Extreme precipitation events and their influence on ice core climate records from Dronning Maud Land, East Antarctica

A Thesis submitted in partial fulfillment for the Degree of

DOCTOR OF PHILOSOPHY

In Marine Sciences

In the School of Earth, Ocean, and Atmospheric Sciences

Goa University

By

SIBIN SIMON

National Centre for Polar and Ocean Research

Headland Sada, Vasco da Gama, Goa, India – 403804

October 2024

DECLARATION

I, Sibin Simon, hereby declare that this thesis represents work that has been carried out by me and that it has not been submitted, either in part or full, to any other University or Institution for the award of any research degree.

Place: Taleigao

Date: 26-09-2024

Sibin Simon

CERTIFICATE

I hereby certify that the above Declaration of the candidate, Sibin Simon, is true, and the work was carried out under my supervision.

26/9/2024

Dr. Thamban Meloth

Research Supervisor

Director

National Centre for Polar and Ocean Research

Vasco-Da-Gama, Goa - 403804

Dr. M. Ravichandran

Research Co-supervisor

Secretary

Ministry of Earth Sciences

Government of India,

New Delhi - 110003

राष्ट्रीय ध्रुवीय एवं समुद्री अनुसंधान केंद्र NATIONAL CENTRE FOR POLAR & OCEAN RESEARCH GOA गोवा

Acknowledgments

I would like to express my heartfelt gratitude to my PhD Guide, **Dr. Thamban Meloth,** Director of the National Centre for Polar and Ocean Research (NCPOR), for his invaluable guidance and consistent support throughout my PhD research. His wisdom and insights have played a crucial role in my development as a researcher, and his constant encouragement has been a source of inspiration, helping me navigate through challenges and grow as a scholar.

I am deeply thankful to **Dr. John Turner**, British Antarctic Survey (retired professor), UK, for being a strong mentor and guiding force in Antarctic meteorology during my PhD journey. Our regular Zoom meetings, along with his constant encouragement despite his busy schedule, have been pivotal in my PhD and in nurturing the researcher in me. His support and mentorship have been incredibly motivating and reassuring.

I also extend my sincere gratitude to my co-guide, **Dr. M. Ravichandran**, Secretary of the Ministry of Earth Sciences and former director of NCPOR, for his guidance during the initial phase of my PhD. I would also like to thank my Doctoral Research Committee members, **Dr. Nuncio Murukesh** from NCPOR and **Dr. Anthony Viegas** from SEOAS, Goa University, for their valuable feedback and support throughout this research.

A special note of thanks to the team at NCPOR, especially the former Director**, Mr. Mirza Javed Beg**, the Group Director, **Dr. Rahul Mohan**, and the project "PACER-Cryosphere and Climate" for their funding and continuous support. I am also grateful to the **HRDG-CSIR** for providing research fellowship funding during the five-year period. I extend my gratitude to the **Vice-Chancellor, Registrar, Dean, and staff of the Earth Science Department at Goa University** for their unwavering support. My thanks also go out to the scientists and staff at NCPOR, as well as the IITM HPC facility 'Pratyush,' for their assistance with atmospheric modeling-related works.

I would like to acknowledge my **lab mates in the F-18 lab** — Subeesh M.P, Vikram Goel, Sunil Oulkar, Ankit Pramanik, Tariq Ejaz, Mohammad Tarique, Gayathri E M, Ahammed Shereef, Teesha Mathew, Ejin George, Pranav S Prem, Aswathi Das — and all the members of the Antarctic Cryospheric Division at NCPOR for their camaraderie and support. My sincere thanks also go to my **colleagues and friends** — Ajith Singh, Milind Mutnale, Sreerag A, Rahul Yadav, Ajay Bhadran, Bijesh CM, Aswini, Anoop T R, Femi Thomas, Harikrishnan G, Susanth Sundaran, Anju, Twinkle, Preethi Paul — for being a source of encouragement, joy, and friendship through travel, cooking, trekking, and all get-togethers. The evening football and volleyball games were invaluable in maintaining a perfect work-life balance and mental health during my PhD.

I am immensely grateful to the international Antarctic meteorology community, particularly the '**AntClimNow**', for funding my attendance at the SCAR-Antarctic extremes workshop in Cambridge, UK, and international conferences such as the IUGG in Berlin, Germany. I would also like to thank **Dr. Pranab Deb** and the members of the Polar Modeling Lab at IIT Kharagpur, as well as all the collaborators during my PhD, for enriching my research and enhancing its quality.

To my family — **my father, Simon K L, my mother, Ruby Simon; my brother, Sangeeth Simon, and his family** — I extend my deepest gratitude for their constant love and encouragement throughout this journey.

Lastly, my heart goes out to my wife, **Sophia**, who has been a constant source of strength since my PhD life and became my life partner during this PhD journey. Her unwavering support and understanding have been my anchor throughout all phases of this PhD, and I am deeply thankful to her for being my strongest pillar.

And finally, I thank **God** for His grace, blessings, and guidance that made this accomplishment possible.

SIBIN SIMON

Dedicated to my family, teachers, and friends…

Table of Contents

Abstract

Ice cores from Antarctica are a unique environmental archive, offering insights into atmospheric composition, climate variability, and change on decadal to millennial timescales, far beyond what direct observations can provide. However, there are significant challenges in interpreting the information contained in the cores because of a limited understanding of the synoptic origins of the snow and ice contained therein, the poor temporal resolution of the signals, which is essentially limited to annual information, and errors in dating the information they contain.

Snowfall is the primary input to ice accumulation, but major gaps exist in our understanding of the seasonality of the precipitation, the role of strong winds in adding or removing snow at an ice core site, and the relationship between accumulation and the various high-latitude weather systems and modes of climate variability. Precipitation in Antarctica is highly episodic, and it is known that its inter-annual variability is primarily controlled by extreme precipitation events (EPEs), especially in the coastal regions. However, we have very limited knowledge of how these extremely important events influence the snow accumulation that is eventually retrieved from the ice cores and the inter-relationship between the precipitation from EPEs and other surface processes, such as blowing snow.

This thesis investigates the impact of extreme meteorological conditions on the climate signals contained within ice core records obtained from the Dronning Maud Land (DML), East Antarctica. This is the first study to examine the influence of intense, short-lived, and episodic extreme meteorological events on annually-resolving ice-core data from Antarctica. The study uses a combination of meteorological reanalysis fields, the output from regional high-resolution atmospheric models, in-situ meteorological observations, surface snow height measurements, satellite images, and annually-resolved ice core data to

address the above questions regarding how EPEs influence the snow and ice accumulation in ice cores.

EPEs occur predominantly in north-easterly to easterly flow associated with deep synoptic-scale depressions over the Southern Ocean and atmospheric rivers (ARs) embedded in strong meridional flow. Approximately 40% of EPEs result from ARs, which are narrow bands of moist air originating at subtropical latitudes, which provide the largest daily precipitation amounts. Precipitation is greatest on the steep, windward slope of orographic features, including ice rises and mountain ranges. The interannual variability in the number of EPEs is controlled by the frequency of quasi-stationary blocking anticyclones over the Southern Ocean northeast of DML. From 1979 to 2018, much of DML experienced a positive trend in the number of EPEs per year as a result of high-pressure systems in the southern South Atlantic and greater cyclonic activity in the Weddell Sea. This led to more frequent poleward winds from the South Atlantic and greater moisture transport into the continent.

A detailed case study was carried out of a major EPE with associated AR that affected DML from 8 – 9 November 2015. The case gave insight into the distribution of precipitation from the event and indicated that it contributed 22% of the total annual precipitation at 71.51°S, 10.15°E, where an ice core was drilled (IND33). The case study was based on the output of a high-resolution atmospheric model optimized for the polar regions (Polar WRF), atmospheric reanalysis fields, in-situ observations, and satellite imagery. The EPE was a result of a blocking high-pressure ridge of record strength that obstructed the eastward track of a storm and resulted in the poleward movement of a deep low-pressure system into the interior of the continent. The anomalously strong AR developed in the subtropics on 7 November 2015 and was characterized by a belt of intense moisture transport from 30-40°S to coastal DML by the following day. The event resulted in heavy snowfall and considerable spatial variability in snow distribution due to interaction with the high, complex coastal orography. These elevated regions are often considered suitable for the drilling of ice cores as they have high accumulation and minimum horizontal ice flow. The large annual snowfall provides high temporal resolution and potentially the chance to resolve sub-annual features. However, with large amounts of snow falling in just a few days each year, these events are a major controlling factor in the annual accumulation and can cause biases in annually dated ice core records.

Analysis of in-situ surface snow height (SSH) changes at the Belgian Princess Elizabeth station (71.57°S, 23.21°E) revealed that both EPEs and strong wind (SW) events could cause large changes in SSH and, therefore, surface snow accumulation, which could, in turn, affect an ice core drilled at the site. Most sudden SSH changes occurred during the days with both extreme precipitation and SW conditions, with such events contributing, on average, 24.3% of the total positive change in SSH during 16 days per year. SW-only events contribute to both positive and negative SSH changes, with mean annual contributions of 22.7% and 24.8%, respectively. Further case studies of high-magnitude SSH change days revealed that strong southerly or easterly winds cause significant changes in SSH on days with little precipitation. These drifting (<1.8 m above the surface) and blowing (>1.8 m above the surface) SW events can transport a considerable amount of snow across the surface, leading to changes in the surface elevation, with the maximum single-day change in SSH observed over 2009-2019 at PE station being 0.128 m.

The variability in the annual accumulation in ice core records is primarily controlled by the number of EPE days. It was found that ice cores drilled from the Derwael (1979-2011) and Hammarryggen (1979-2018) ice rises had a positive correlation ($p < 0.05$) with the yearly ice core accumulation value and the number of EPE days per year. However, in some years of low ice core accumulation, there were many EPEs but also a large number of SW days, suggesting that a considerable amount of the snowfall that fell was blown away. Thus, extreme meteorological conditions, both in terms of EPEs and SW events, are vitally important in influencing the accumulation recorded in the ice cores and, therefore, interpreted climate records.

Both EPEs and the surface wind fields are strongly influenced by orography, and such events may occur on only a few days each year, yet they can skew the information contained in the annual ice core data towards particular meteorological conditions. These may be intrusions of air originating at low latitudes, anomalous atmospheric circulation over the Southern Ocean, or circulation regimes over the Antarctic ice sheet.

There is a complex relationship between the processes that lead to precipitation over the Antarctic and the accumulation of snow that is eventually extracted via an ice core. This study has shown that a thorough assessment of the meteorological conditions should be undertaken before an ice core is drilled at a location. This will aid the interpretation of the extracted data and the production of a climate record. Consequently, investigating the influence of extreme meteorological conditions can aid in the strategic selection of ice core drilling locations, helping to mitigate biases in annually-dated climate signals derived from ice cores in coastal Antarctica.

Keywords: Extreme precipitation events, Moisture transport, Atmospheric rivers, Orographic features, Antarctica, Blocking Anticyclones, Polar WRF, Ice cores, Surface wind events, snow accumulation

List of Abbreviations and Acronyms

EPE	Extreme Precipitation Event
DML	Dronning Maud Land
AR	Atmospheric River
WRF	Weather Research and Forecast
SSH	Surface Snow Height
SW	Strong Wind
EP	Extreme Precipitation
GHG	Green House Gas
AP	Antarctic Peninsula
EAIS	East Antarctic Ice Sheet
WAIS	West Antarctic Ice Sheet
SAM	Southern Annular Mode
ENSO	El Niño-Southern Oscillation
EPICA	European Project for Ice Coring in Antarctica
ECMWF	European Centre for Medium-Range Weather Forecasts
AWS	Automatic Weather Station
GCM	General Circulation Model
AMPS	Antarctic Mesoscale Prediction System
IVT	Integrated water Vapor Transport
IWV	Integrated Water Vapor
SMB	Surface Mass Balance
RCM	Regional Climate Model
IPCC	Intergovernmental Panel on Climate Change
PBL	Planetary Boundary Layer

ERA5	ECMWF Reanalysis (5th Generation)
IFS	Integrated Forecast System
MSLP	Mean Sea Level Pressure
MERRA	Modern-Era Retrospective analysis for Research and Applications
JRA55	Japanese 55-year Reanalysis
CFSv2	Climate Forecast System Version 2
GOES	Geostationary Operational Environmental Satellite
NOAA	National Oceanic and Atmospheric Administration
POES	Polar Orbiting Environmental Satellite
NCAR	National Center for Atmospheric Research
RMSE	Root Mean Square Error
4D-Var	4-Dimensional Variational Data Assimilation
GMTED	Global Multi-resolution Terrain Elevation Data
MODIS	Moderate Resolution Imaging Spectroradiometer
RRTMG	Rapid Radiative Transfer Model for General Circulation Model
WSM5	WRF single-moment-microphysics class 5
MYJ	Mellor-Yamada-Janjic
SCAR	Scientific Committee on Antarctic Research
READER	Reference Antarctic Data for Environmental Research
YSU	Yonsei University Scheme
MYNN	Mellor–Yamada– Nakanishi–Niino
ACM2	Asymmetric Convective Model version 2
WDM6	WRF Double-Moment 6-class
PE	Princess Elisabeth
NW	North Westerly

SW	South Westerly
SE	South Easterly
NE	North Easterly
RACMO2	Regional Atmospheric Climate Model version 2
HIRLAM	High-Resolution Limited Area Model
MAR	Modèle Atmosphérique Régional
SR	Snowfall Rate
GPR	Ground Penetrating Radar
DC	Directional Constancy
vIVT	Meridional Integrated Water Vapor Transport
SOM	Self-Organizing Maps
EOF	Empirical Orthogonal Function
MK	Mann-Kendall
EAP	East Antarctic Plateau
AMSL	Above Mean Sea Level
LW	Longwave
RH	Relative Humidity

List of Figures

List of Tables

Chapter 1

Introduction

Recent decades have seen exceptional climatic changes in many parts of the Earth. The concentrations of greenhouse gases have increased alarmingly, which, through the greenhouse effect, has led to the global mean near-surface temperature rising at an unprecedented rate (Legg, 2021). This has resulted in a greater frequency of heatwaves, extreme precipitation events, and altered weather patterns globally (Perkins-Kirkpatrick & Gibson, 2017). Studies have shown that the polar regions are an integral and critical part of the global climate system and are particularly vulnerable to the global changes taking place. The phenomenon of polar amplification means that temperature increases in these regions are more than twice the global average rate (Bintanja & Oerlemans, 1995; Holland & Bitz, 2003). Regionally, there has been a significant reduction in the extent of sea ice across the Arctic, with the extent reaching several historic lows. These changes in sea ice extent not only affect the habitat of polar species but also have broader implications for the global climate system, as they disrupt oceanic circulation patterns and influence weather systems far beyond the polar regions (Jahn et al., 2024; Q. Wang, 2021).

Antarctica is the highest, coldest, windiest, and driest continent and is an essential element of the global climate. In recent decades, the Antarctic continent has undergone considerable climatic changes. Temperatures have risen alarmingly over in the Antarctic Peninsula region, leading to rapid ice shelf disintegration and glacier retreat (Cook et al., 2005; Vaughan et al., 2003). Some of the largest increases in annual mean temperatures on Earth have been witnessed in the Antarctic Peninsula region over the past 50 years, with a shift to more rainfall and a 'greening' of the region (Turner et al., 2005). The appearance of the ozone hole had a significant impact on Antarctica, with total column ozone depletions exceeding 50% during the 1990s. Additionally, the Antarctic ozone hole reached its largest recorded size in the spring of 2000 (Hofmann et al., 1997; A. E. Jones & Shanklin, 1995). The ozone hole has led to a cooling in the stratosphere, influencing atmospheric circulation patterns and mitigating some of the expected warming from rising greenhouse gas (GHG) concentrations (Marshall, 2003; Thompson & Solomon, 2002).

About 90% of the Earth's ice is contained in Antarctic ice sheets, and it represents the largest freshwater reservoir, making its stability critical for maintaining current sea levels (Pattyn & Morlighem, 2020). The complete melting of the entire Antarctic ice sheet could raise global sea levels by ~60 m, with even partial loss having catastrophic consequences for sea levels, ecosystems, and coastal regions (Fretwell et al., 2013; Vaughan et al., 2013). The elevation of the ice sheet increases rapidly inland from the coast, making Antarctica the Earth's highest continent, with an average altitude of approximately 2,200 m (Turner, 2009). About 2% of the continent's ice is in the form of ice shelves, which are floating extensions of ice sheets in the coastal regions formed due to glacial ice flow from the interior of the continent. Near these ice shelves, highly elevated (~ 500 m), small, grounded features called ice rises and ice rumples are located. These are formed when the ice flows over topographically elevated features beneath the surface. As the ice is forced upward, it creates a dome-shaped bulge on the ice shelf's surface (Matsuoka et al., 2015).

Most of the surface of Antarctica is covered by ice and snow. However, the surface also has many morphological and local topographical features, such as nunataks, which are exposed rock outcrops extending upwards from the mountain ranges below. These exposed mountain peaks make up 2.4% of the area of the continent (King & Turner, 1997) and are important meteorologically because of their low reflectivity. Geographically, Antarctica's ice sheet is segmented into three major regions: the Antarctic Peninsula (AP), which extends north-south, the East Antarctic Ice Sheet (EAIS), and the West Antarctic Ice Sheet (WAIS). These regions are divided by the Trans-Antarctic Mountains, stretched between the Ross and Weddell Sea regions (Figure 1.1).

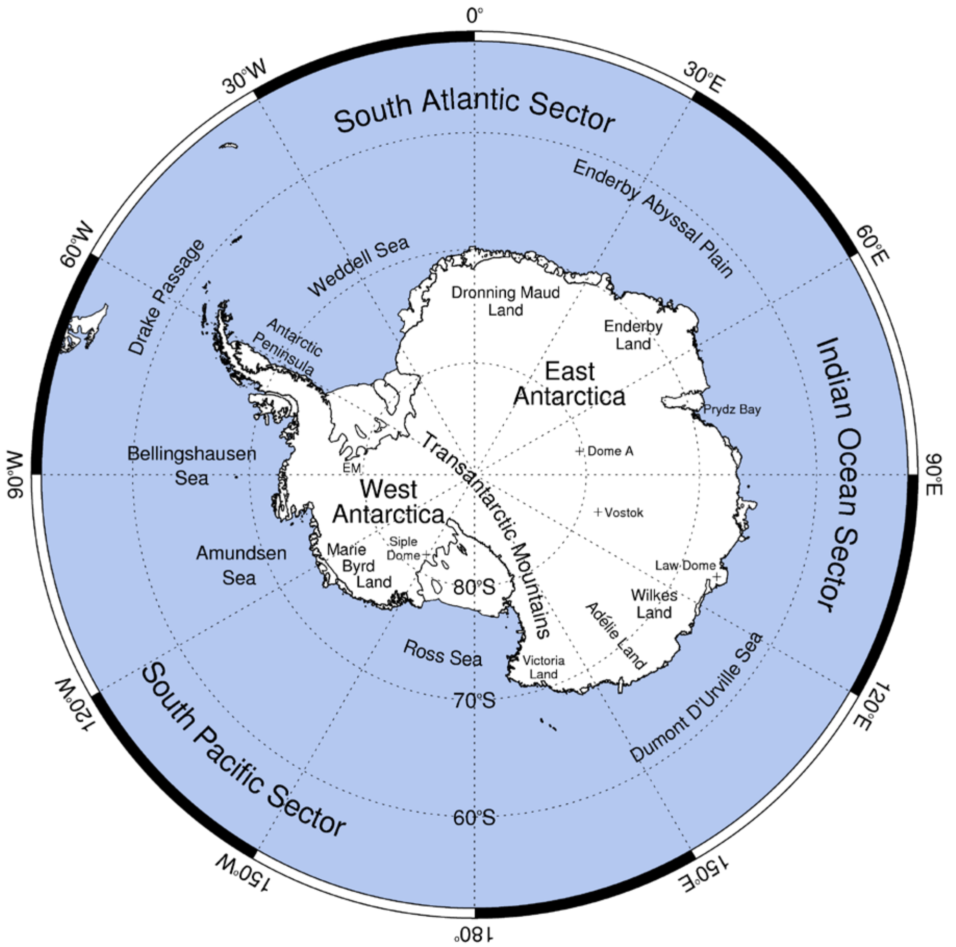

Figure 1.1: Antarctic map highlighting locations and notable topographic features. (Turner, 2009).

The EAIS is high and dome-shaped, reaching a maximum elevation of 4,090 m at Dome A (80º S, 77ºE). The EAIS is considered stable because it rests on mountains above sea level. However, if it were to melt fully, it could contribute up to a 53 m rise in sea level, with a higher potential than the WAIS (Fretwell et al., 2013; Shepherd et al., 2018). In contrast, the WAIS is a grounded ice sheet, much of which rests on the ocean floor, with low-elevation regions and a mean elevation of 850 m (King & Turner, 1997). The intrusion of warm ocean water beneath the WAIS poses a significant threat, as it could lead to melting and contribute about 3.3 meters to sea level rise globally (Bamber et al., 2009; Shepherd et al., 2004).

The stability of ice sheets in the Antarctic depends on the balance between the input of precipitation and ice loss through coastal ice melt and iceberg calving. Thus, precipitation over Antarctica is a crucial factor in mitigating sea-level rise by influencing the growth and dynamics of the ice sheet (Lenaerts et al., 2013; Medley & Thomas, 2019). Increased precipitation could help offset some of the mass loss from the ice sheet, reducing its contributions to global sea level rise (Davis et al., 2005). Solid precipitation is by far the dominant form of precipitation over the continent. However, rainfall also occurs over some coastal parts of the Antarctic, especially the north-western Antarctic Peninsula and East Antarctica (Vignon et al., 2021). The nature of the precipitation differs substantially between the coastal and interior parts of the continent, with small quantities of clear sky precipitation (diamond dust) falling from thin, isolated clouds or a seemingly clear sky in inland locations. In contrast, snowfall on the coast is episodic and often gives large amounts of snow (Bromwich, 1988). Large, episodic snowfall events in the coastal region are associated with cyclonic systems in the circumpolar trough region, which encircles the continent between 60°S and 70°S. This trough is characterized by three climatological low-pressure centers close to 150°W, 20°E, and 90°E, located north of the continent (King & Turner, 1997). The latitudinal position of the circumpolar trough exhibits a semi-annual oscillation, which is influenced by the different annual temperatures at mid and high latitudes. It results in the trough being deeper and further south in spring and autumn, and further north and weaker in summer and winter. This seasonal change in surface pressure around Antarctica significantly affects the net transfer of air and moisture towards the continent (King & Turner, 1997). The temperature difference is most pronounced during the autumnal equinox, leading to a peak in cyclonic activity over the continent (Loon, 1967).

The Southern Annular Mode (SAM) is another climate cycle that significantly impacts meteorological conditions across Antarctica. It represents the primary pattern of climate variability in the region and involves an oscillation of mass between high and mid-latitudes. SAM is marked by a poleward strengthening of mid-latitude westerly winds during its positive phase, extending from the surface to the upper levels. Conversely, in its negative phase, these winds weaken equatorward (Marshall, 2003). It has been shown to control cyclonic activity and precipitation over the continent, especially in West Antarctic regions, with a positive phase of this circulation pattern (Marshall et al., 2017).

Atmospheric and oceanographic conditions in the tropics can also affect the climate of Antarctica through teleconnections, for example, the El Niño-Southern Oscillation (ENSO) cycle in the Pacific Ocean (Turner, 2004). The signals of ENSO have been recognized in the Antarctic's physical climate system through long-range Rossby wave dynamics (X. Li et al., 2021). Also, studies reveal that Antarctic climate extremes are extremely responsive to disturbances in the ocean and atmosphere occurring in the mid-latitudes and subtropics (Blanchard-Wrigglesworth et al., 2023).

Recent findings reveal that the precipitation in Antarctica is highly episodic and dominated by extreme precipitation events (EPE). These EPEs give substantial daily precipitation and account for a significant portion (40-60%) of the annual snowfall. They are identified as the main factor influencing both intra- and inter-annual variability in snowfall across the Antarctic continent (Turner et al., 2019). Long-range moisture transport linked to a dipole pattern of positive and negative anomalies in the geopotential height to the east and west of the region emerges as the primary synoptic pattern during these EPEs (Gorodetskaya et al., 2014; Welker et al., 2014; Yu et al., 2018). The orography of the coastal region is also a key factor in the lifting of the warm, moist airmasses from low-latitude oceanic areas and the distribution of precipitation during these EPEs (Gehring et al., 2022; Thomas et al., 2017).

In addition to their meteorological effects, these EPEs greatly affect the interpretation of chemical signals in ice cores. As precipitation events bias stable water isotope records in ice cores, EPEs can heavily skew the annual climate signals. In some years, these records may reflect data from just one season or a few EPE occurrences, leading to potential misinterpretations of the climatic history (Turner et al., 2019). Antarctic ice cores are the most important natural archives for investigating pre-instrumental climatic variability, particularly utilizing the chemical species in the snow, trapped gases, and isotopic composition of ice, spanning timescales ranging from sub-annual to glacial and interglacial periods. Antarctic ice core investigations have transformed our understanding of climatic variability and have become vital to climate change detection and attribution research (Mayewski et al., 2009). Over Antarctica, the ice core stable isotope data interpretation assumes continuous, seasonally distributed precipitation. However, snowfall does not occur continuously during the year, and the isotope record can be influenced by the intermittent nature and seasonality of precipitation (Münch & Laepple, 2018; Zuhr et al., 2021). The temperature record from ice cores is often obtained using the isotopic composition of the ice, particularly the ratio between heavy to light oxygen isotopes, denoted as $\delta^{18}O$ (Dansgaard, 1964), and this relationship is assumed to be constant and linear in space and time. In Antarctica, the water isotope records represent a variety of complicated processes that are determined by the temperature at which the moisture evaporates from the ocean's surface, the subsequent condensation and evaporation cycles, and the temperature at which the moisture eventually condenses before precipitating, sea surface conditions and changes in moisture source areas (Casado et al., 2018; Schlosser, 1999; Werner et al., 2000). Due to the frequent strong winds over the Antarctic continent, there is often post-depositional redistribution of the freshly precipitated snow, leading to the mixing of the annual climate signals in the ice cores (Karlöf et al., 2005; King et al., 2004). Thus, the annual layers of ice cores can be skewed by the significant contribution of the EPEs to the annual accumulation. Identifying the individual short-lived events in ice cores is impossible due to the low temporal resolution of ice cores, which is typically annual or seasonal. However, the contribution of EPEs to shaping annual ice core accumulation highlights their crucial importance.

The ice core community often focuses on the chemical and geochemical aspects of ice core records in paleo-climate studies, and more work is needed on the links between local and global meteorological environments in generating the climate signals from the ice cores. For improved paleo-climate reconstruction using ice cores, a better understanding of the frequency and seasonality of EPEs, atmospheric processes behind EPEs, moisture transport, and mechanism, and changes in atmospheric parameters at the deposition location, etc. is required (Noone et al., 1999; Turner et al., 2019). Since the Dronning Maud Land (DML) region has often been the focus of ice core drilling programs, and EPEs are more pronounced over these regions (Welker et al., 2014), this study seeks to examine the impact of EPEs on proxy-based ice core climate records. Many orographic characteristics, such as ice shelves, ice rises, and ice rumples, dominate the coastal DML region, controlling precipitation and surface accumulation (Goel et al., 2020; Pratap et al., 2022; Rotschky et al., 2007). Only a few studies have examined in detail the high precipitation events that occur in this part of Antarctica, and most of the studies were conducted only for short periods (Birnbaum et al., 2006; Noone et al., 1999; Schlosser, Manning, et al., 2010; Welker et al., 2014). Hence, this PhD work presents the first detailed study of EPEs and the role of these extreme atmospheric conditions in shaping the annual precipitation accumulations in ice cores. This doctoral study focuses on climatological analysis (1979-2018) and case studies to better explain the distribution, nature, and origins of EPEs and how they influence the snow and ice contained in ice cores. This work uses a combination of atmospheric reanalysis data, aided by simulations from a high-resolution regional atmospheric model, in-situ observations, and ice core proxy data from coastal DML, East Antarctica. The following are the specific objectives of this doctoral study,

Objectives of the study

a) Identify the atmospheric processes that lead to EPEs over coastal DML.

b) Determine the characteristics, distribution, and variability of meso- and synoptic-scale cyclones and the role of these systems in generating EPEs over DML.

c) Quantify the influence of anomalous atmospheric parameters during EPEs and their impact on annually resolving ice core climate records from coastal DML.

1.1 Outline of the thesis

This thesis consists of six chapters, each addressing different aspects of the study. These are as follows:

Chapter 1 outlines the significance of this research based on existing literature and identified knowledge gaps. It introduces the Antarctic climate and the impact of EPEs in the study region. It also discusses the potential implications of these extreme events on paleo-climate signals from ice cores and underscores the importance of this study. Additionally, it highlights previous regional modeling efforts over Antarctica and the use of these models to understand extreme events better.

Chapter 2 provides a comprehensive overview of the study region, DML in East Antarctica, and details the data and methods employed in this research. It describes the optimization of the regional model through sensitivity studies and validation using in-situ data and identifies the best combination of parameterization schemes for simulating synoptic scale events in the study area. The chapter also explains the various datasets used, including reanalysis model outputs, satellite images, in-situ observation data, and ice core annual accumulations, along with the different methods applied in the study.

Chapter 3 focuses on the climatological analysis of the spatio-temporal variabilities of EPEs in the region and the controlling factors for this variability. It presents detailed results of the precipitation contribution from EPEs, the number of EPE days at ice core locations, significant trends of EPEs in the region, and the quantified contribution of atmospheric rivers in causing EPEs.

Chapter 4 uses regional model simulations to investigate a single EPE occurrence in detail, examining the extreme upper and lower atmospheric processes responsible for the EPE. This case study provides an in-depth analysis of moisture uptake, transport, and precipitation features and discusses the role of the complex coastal orography in the distribution of precipitation.

Chapter 5 estimates the impact of extreme meteorological conditions on significant changes in surface snow height and snow accumulation in the study region. It uses in-situ observations from coastal areas to quantify the influence of extreme events on surface accumulation. The chapter further explores how these extreme conditions contribute to changes in annual accumulation values at selected ice core locations, linking the role of extremes to the shaping of annual ice core accumulations and their implications for ice core records.

Chapter 6 presents the key conclusions of this doctoral research and explores potential directions for future studies.

1.2 Literature review

1.2.1 Precipitation over Antarctica

The net snow accumulation of the Antarctic continent is the balance between input through precipitation and loss via evaporation, drifting snow, and melt-water run-off (Bromwich, 1988). It has been estimated that about 2,300 km^3 of snow falls on the continent each year (Fortuin & Oerlemans, 1990), but measuring precipitation in the Antarctic is extremely difficult because significant snowfall typically occurs at the same time with strong surface winds (Bromwich, 1988). Other approaches, such as snow stakes, stratigraphy, and examination of snow and ice retrieved from pits and ice cores, are used across the Antarctic because standard snow gauges provide inadequate data due to the influence of the wind, which can blow snow out of the gauge (King & Turner, 1997). There is a large difference in precipitation magnitude between the coastal areas and the interior of the continent. Giovinetto & Bull, (1987) estimated that generally high values of annual total precipitation of ~800 mm or more are found in the coastal regions. This contrasts with the significantly smaller amounts of < 50 mm $year^{-1}$ in the desert-like interior regions where the altitude is higher than 3,000 m. Thus, the precipitation decreases rapidly from the coast to the interior by about 90% within a distance of 1,000 km, as the air becomes drier and colder as it moves away from the coast and rises in elevation. In the inland regions, small precipitation occurs in the form of ice crystals falling from thin, isolated clouds, whereas coastal regions often experience intermittent and high-magnitude precipitation from frontal cyclones or long-range moisture transport mechanisms (King & Turner, 1997; Noone et al., 1999). This pattern over coastal Antarctica shows the impact of large-scale weather systems and the influence of synoptic-scale features such as cyclones and fronts. The synoptic activity around the Southern Ocean is crucial for bringing precipitation to the Antarctic continent (Simmonds et al., 2003). Local maxima in precipitation are found on the windward side of orographic features due to moist, low-level air rising rapidly and cooling, leading to cloud formation and precipitation (Doswell et al., 1996, 1998)). EPEs can be defined in different ways, but are often taken as days with precipitation above a particular threshold value calculated from the long-term time series of precipitation (Schlosser, Manning, et al., 2010; Yu et al., 2018). Due to the episodic nature of EPEs, the daily precipitation frequency distribution at these coastal locations has an extended tail of extremely dry days and a short tail of high precipitation days (Noone et al., 1999; Yu et al., 2018). EPEs are linked to the amplification of planetary waves, which advect warm, moist airmasses from low latitudes far north of the Antarctic continent. They occur with a frequency of 10-20 events days per year, particularly at coastal locations (Schlosser, Manning, et al., 2010; Turner et al., 2019). The synoptic patterns and features of EPEs have been investigated across various regions of Antarctica, including the coastal region of the Antarctic Peninsula (González-Herrero et al., 2023; Turner et al., 1995, 1997), the Amundsen Sea Embayment (Swetha Chittella et al., 2022), the Ross Sea (Markle et al., 2012; K. E. Sinclair et al., 2010), and the Prydz Bay region (Yu et al., 2018).

1.2.2 Characteristics of precipitation over Dronning Maud Land (DML)

DML is the region between 20°W and 45°E, mostly south of the Atlantic Ocean, characterized by rapidly increasing orographic height, particularly close to the coast (Rotschky et al., 2007). Snow distribution is impacted by orographic factors and wind-driven sublimation and redistribution on the grounded ice sheet (Reijmer et al., 2004; Thiery et al., 2012). The two most typical climatological divisions of DML are the low-altitude coastal areas with high to moderate snowfall amounts (600-800 mm year^{-1}) and the high-altitude interior plateau with dry conditions (20-50 mm year^{-1}), which are divided by the nunatak and mountain ranges (Bromwich, 1988; Rotschky et al., 2007; Welker et al., 2014). The coastal area of DML is also affected by strong, cold katabatic winds that originate in the high-altitude, dry interior plateau flow towards the continent's edge, and are diverted to the left by the Coriolis Force (Parish & Bromwich, 1987). The surface mass balance of the coastal region is affected by the spatial variability of snow erosion/deposition by these katabatic winds (Broeke et al., 1999). Furthermore, the convergence zone of warm, moist air from the ocean and cold katabatic winds from the continent's interior is ideal for the formation of powerful coastal mesocyclones, which are responsible for short-duration (less than a day) high precipitation events (Carrasco et al., 2003; Pezza et al., 2016). Synoptically induced precipitation strongly influences DML due to amplified upper-level planetary waves (Schlosser et al., 2010). These large, meandering, upper-level waves advect warm, moist airmasses to coastal DML (Welker et al., 2014). The low-altitude coastal region experiences occasional EPEs due to the orographic lifting of warm, moist airmasses. The precipitation is enhanced with support from strong vertical motion, decreased static stability of the atmosphere, and enhanced levels of moisture, which are common in synoptic weather systems (Bromwich, 1988; Welker et al., 2014).

Since DML is the key location for many ice core drilling programs (e.g., EPICA-European Project for Ice Coring in Antarctica), the precipitation pattern and distribution over this area have been investigated in a number of studies (Noone et al., 1999; Schlosser, Manning, et al., 2010; Welker et al., 2014) using in-situ measurements and reanalysis data. Coastal DML is prone to intermittent and intense EPEs, contributing to more than half of the annual total precipitation over the region within 10-20 days per year (Turner et al., 2019). Extratropical cyclones and associated fronts in the circumpolar trough, lead to many high precipitation occurrences over DML (Bromwich, 1988; Pfahl & Wernli, 2012). The north-northeasterly winds on the eastern flank of these cyclones drive moist airmass poleward, where the orographic barriers lift it, cool it, and result in precipitation (Schlosser et al., 2008). Over several days, persistent weather systems linked with enhanced upper-level planetary waves and blocking anticyclones promote the strong advection of moisture and heat to the interior of DML from low latitudes (Noone et al., 1999; Schlosser, Manning, et al., 2010; Welker et al., 2014). Most studies cover only a few years, and the occurrence of high-precipitation episodes had no discernible seasonality. According to a climatological study of high precipitation days over DML (Welker et al., 2014), ~30% of EPE days occur in the autumn (MAM) for Kohnen and Halvfarryggen stations in the DML region. This seasonality can differ depending on the poleward transport of warm, moist airmasses and the position of synoptic features over coastal DML. Changes in the position of a climatological low-pressure system over the southern Atlantic Ocean, located between 15˚E and 25˚E, induce an easterly airflow along the DML coast, delivering moisture and precipitation to the eastward-facing steep slopes of north-south aligned mountain ranges (Lenaerts et al., 2013). Nearly 50% of annual precipitation variability across East Antarctica is related to changes in synoptic-scale characteristics linked to the major patterns of variability, such as the SAM and ENSO (Yu et al., 2018). Stronger circumpolar westerly winds, associated with recent changes towards the SAM's positive phase, influence the formation of cyclones over the Southern Ocean, leading to higher precipitation in the circumpolar trough (Noone & Simmonds, 2002; M. R. Sinclair, 1997). The negative SAM phase corresponds to Rossby wave amplification and greater meridional atmospheric flow (Marshall, 2003; Schlosser et al., 2011). Increased poleward flow on the western side of blocking high-pressure systems causes substantial changes in precipitation and temperature near the coast (Hirasawa et al., 2000).

1.2.3 High precipitation events over DML

EPEs over DML have been studied using atmospheric models, reanalysis data, and in-situ observations to understand the upper and surface synoptic patterns during these events. A few studies (Gorodetskaya et al., 2014; Lenaerts et al., 2013; Schlosser et al., 2016) investigated the characteristics of anomalous high precipitation years, while others (Noone et al., 1999; Schlosser, Powers, et al., 2010) studied the details of these events using case studies with available high-resolution model and reanalysis data. In terms of the availability of in-situ observations, the majority of the research covers just a few years (Birnbaum et al., 2006; Reijmer & Broeke, 2003; Schlosser, Manning, et al., 2010), and only a few studies (Welker et al., 2014) use a climatological approach to investigate them. Noone et al., (1999) conducted a comprehensive study of precipitation over DML using operational and reanalysis data from the European Centre for Medium-range Forecasts (ECMWF). According to the study, synoptically-generated high precipitation occurrences connected with amplified upper-level planetary waves transporting moist air from low latitudes into the continent's interior have resulted in unusually high precipitation, contributing about 25-30% of total annual precipitation. These EPEs are the predominant factor controlling the precipitation variability over the year. Their occurrence has been linked to the variability of cyclonic systems across the hemisphere, especially storms centered in and to the Weddell Sea's north region (Noone et al., 1999). These storms are crucial in the heat and moisture balance over the Antarctic coastal regions (M. R. Sinclair, 1981). Reijmer & Broeke, (2003) used automatic weather station (AWS) observations from DML to validate the presence of these episodic occurrences, which contribute about 50% of yearly precipitation in a few (about 7%) large precipitation events. They further demonstrate that as elevation and distance from the coast increase, the number of events and accumulation from each event decreases. Using a general circulation model (GCM), Noone & Simmonds (1998) demonstrated the presence of a dipole structure of MSLP anomaly in the zonal direction during EPEs, and they also estimated the anomalous changes in atmospheric temperature and wind speed during these events. The surface temperature measurements during EPE days were found to be ~10°C warmer than the climatological mean values (Noone and Simmonds, 1998). Enomoto et al., (1998) investigated the warming caused by blocking high-pressure systems that lasted several days and were connected to the advection of warm, moist airmasses. The longwave radiation changes due to cloud cover and increased wind speed during these events lead to the breakdown of the surface temperature inversion layer, resulting in a significant increase in temperature from -73°C to -36°C in two days over interior DML (Hirasawa et al., 2000). Using satellite and reanalysis data, Massom et al. (2004) demonstrated the role of occasional, long-lived atmospheric blocking-high activity in the South Tasman Sea in delivering ~27% of annual total snowfall much further south over the central East Antarctic Ice Sheet plateau. During these snowfall events, the moisture source was from 35°S to 40°S in the Southern Ocean.

Birnbaum et al., (2006) found that during the summer months of 2001 to 2005, three main kinds of synoptic weather patterns resulted in excessive snowfall at Kohnen station (75°S, 0°E, 2892 m) in DML. Combined in-situ observations, reanalysis fields, and satellite images were used for the classifications of major synoptic patterns, such as 1) eastward-moving low-pressure systems and associated fronts, 2) westward-moving frontal clouds or secondary lows originating close to the Greenwich meridian, and 3) an upper air low west of Kohnen station enhanced by large scale lifting processes. Compared to cyclones that move eastward, the study indicated the contribution of frontal clouds with retrograde movement (westward) or secondary lows, which also bring substantial precipitation to the region. Schlosser et al., (2010) used data from the Antarctic Mesoscale Prediction System (AMPS) to calculate precipitation from 2001 to 2006 and categorize EPEs at Kohnen station. They examined five frequent synoptic scenarios during the high precipitation episodes, which were: 1) strong and deep cyclones to the north of the station, blocking high-pressure to the east of the station with 2) north westerly flow, 3) north easterly flow,

4) a weak ridge over the station, and 5) an upper air low south of the station. They also discovered that only 20% of the events were closely linked to strong cyclones and frontal systems, but blocking anticyclones was involved in more than half of the cases. A 30-year climatological analysis of high precipitation events over DML (Welker et al., 2014) provided new insight into the upper and surface-level interactions of atmospheric patterns during EPEs. They demonstrated that vertically integrated water vapor transport (IVT) might be utilized as a predictor for heavy snowfall occurrences, with the moisture transported to the DML interior by a trough-ridge-trough pattern in the upper level, and at the surface, a cyclone and blocking high pressure to the west and east of DML, respectively. When this large amount of moisture interacts with local orography during a strong northerly-north westerly flow, the airmass rises, leading to adiabatic cooling, followed by condensation of water vapor in the air and, eventually, cloud formation and heavy precipitation. A Rossby wave intensifying in the meridional direction, forming a trough-ridge-trough pattern north of DML, and high-amplitude moisture transport a few days before the event are both critical factors in the triggering of EPEs over DML (Schlosser et al., 2008; Welker et al., 2014). Detailed case studies by Schlosser, Powers, et al., (2010) using high-resolution AMPS data also confirmed that a blocking high over eastern DML is important, directing a large amount of moisture toward the continent. Increased temperature and wind speed during these events were also noted.

1.2.4 Atmospheric rivers (ARs) leading to EPEs over DML

Recent research has discovered that 'atmospheric rivers (ARs),' which are narrow and transitory long bands of intense horizontal water vapor transport extending from subtropical latitudes to the Antarctic coast, are capable of transporting a considerable amount of moisture to DML (Gorodetskaya et al., 2014; Wille et al., 2021). Gorodetskaya et al. (2014) explain the role of ARs over DML in leading to EPEs as strong moisture fluxes and associated high vertically integrated water vapor (IWV) values. These values are concentrated along the eastern side of a deep cyclone that is centered north of DML. The cyclone is blocked on the eastern side by an anticyclone, directing air toward and making landfall on the DML coast (Gorodetskaya et al., 2014). These ARs frequently begin in the tropics or subtropics and then extend southward, carrying water vapor to high latitudes (Ralph et al., 2004; Zhu & Newell, 1998). As a result of the large intrusions of warm, moist airmasses, ARs making landfall in Antarctica's coastal areas contributed to heavy snowfall, accounting for about 70% to 80% of the surface mass balance (SMB) and also affecting melt processes on the ice sheet (Bozkurt et al., 2018; Gorodetskaya et al., 2014; Wille et al., 2021). One of the primary factors establishing AR and poleward moisture transport during these occurrences is a strong blocking over the Southern Ocean to the east of DML (Pohl et al., 2021). Wille et al., (2021), in their Antarctic-wide climatological analysis of ARs covering 1980 to 2018, found a significant increasing trend of these ARs across DML, and this region is more vulnerable to short-term EPEs than precipitation generated by cyclonic activity (Turner et al., 2019; Wille et al., 2021). The significant moisture flux and extreme state of lower tropospheric profiles of temperature, wind speed, humidity, and moisture transport induced by strong low-level jets are seen in the vertical profiles of ARs over the DML coastline region (Gorodetskaya et al., 2020). In a case study of an AR over the DML coast, Terpstra et al., (2021) illustrated the establishment of a secondary mesoscale cyclone in the latter stages of ARs, promoting further poleward moisture transport. Baiman et al., (2023) found the presence of coastal barrier jets, which are the areas of anomalous easterlies along the coastal DML south of the low-pressure system. These low-level blocking winds can enhance precipitation during AR occurrences by supporting the upward vertical motion of poleward moisture intrusions along the complex orography over DML (Baiman et al., 2023; Bromwich, 1988).

1.2.5 Regional climate model-based studies over Antarctica

Regional climate models (RCMs) are used to dynamically downscale global model simulations for specific regions. They demonstrate better skill than GCMs in areas with rapidly varying orography and small-scale phenomena (Douville et al., 2021). This study utilized the atmosphere-only regional model 'Polar WRF' optimized for polar conditions (details in Chapter 2). Polar WRF has been widely used for short- and long-duration regional modeling studies over Antarctica (Bromwich et al., 2013; Guo et al., 2003). The model's performance varies with different lateral and initial boundary conditions, with ERA-Interim reanalysis data providing better performance than other forcing data (Bromwich et al., 2013). Model discrepancies, particularly in simulating 2-m temperatures and surface winds, can be mitigated by optimizing parameterization schemes for downscaling climate variables over Antarctica (Deb et al., 2016; Somos-Valenzuela & Manquehual-Cheuque, 2020). Increasing model resolution enhances the representation of surface winds, although the model struggles to capture transient cyclones during winter in coastal Antarctica (Deb et al., 2016). Tastula & Vihma, (2011) conducted sensitivity studies to identify the optimal combination of parameterization schemes in the planetary boundary layer (PBL), surface layer, and radiation processes, validating their findings against coastal and inland station observations. These studies revealed significant improvements in model performance by integrating selected parameterization schemes. Further sensitivity studies indicated substantial improvements in simulating severe wind events over coastal Antarctica (Powers, 2007). Enhancing data assimilation and grid resolution also improved the representation of surface parameters (Powers, 2007). Investigations of coastal Antarctic cyclones using AMPS data, which employed the WRF model for regional simulations, demonstrated the model's efficacy in capturing complex interactions between katabatic winds and coastal orography during cyclone landfall, as well as representing various atmospheric parameters associated with synoptic-scale events (Nigro et al., 2012).

1.2.6 Implications of EPEs on ice core climate records

Snowfall is the main input to ice cores, which are a primary tool for reconstructing the long-term climatic history of Antarctica. Over coastal DML, the snowfall is highly episodic and contributes a large proportion to the annual total precipitation in a few days (Turner et al., 2019). The local snowfall conditions, frequency, magnitude, origin of the airmass, and moisture content greatly impact the climate information preserved in ice cores. The conditions during snowfall do not have to be representative of the average conditions at that location (Noone et al., 1999; Noone and Simmonds, 1998).

Also, days with EPEs recorded in ice cores had much higher temperatures than usual (Schlosser et al., 2010). The advection of warm, moist airmasses associated with blocking high-pressure systems and the occurrence of warm winter storms causing precipitation over the Antarctic coastal regions can lead to a significant warm bias in the ice-core records (Jackson et al., 2022; Servettaz et al., 2020), and the reconstruction of the ice core isotope data will be overestimated if this warm bias is not taken into account (Noone and Simmonds, 1998; Servettaz et al., 2020). High wind speeds during these precipitation events can affect post-depositional processes, including erosion, drift, vertical mixing, and blowing snow, all of which can affect the spatial variability of ice core proxies (Fisher et al., 1985; Karlöf et al., 2005; Münch et al., 2017). The majority of moisture sources for snowfall in DML are found between 40°S and 60°S in the southern Atlantic Ocean (Reijmer & Broeke, 2001), and moisture transport during AR episodes also reveals the moisture source further north from low latitudes (Gorodetskaya et al., 2014; Terpstra et al., 2021). However, a northern moisture source does not always imply more isotopic fractionation since the temperature difference between the source and deposition region is smaller, resulting in less heavy-isotope depletion (Schlosser et al., 2008). Changes in moisture supply, dynamic effects during evaporation from the ocean surface and atmospheric transport, and systematic changes in general atmospheric circulation can all alter stable isotope records (Masson-Delmotte et al., 2008; Reijmer et al., 2002). The interpretation of ice core records, on the other hand, is not straightforward because of the limited proxy-data calibration possibilities, inconsistencies in dating, seasonality of precipitation, fluctuations in airmass transport pathways, changes in source evaporation conditions, and other uncertainties; there are complications in ice core proxy data, that must be considered (Delaygue et al., 2000; Masson-Delmotte et al., 2008; Vimeux et al., 1999). It is also probable that the seasonality of precipitation events has varied during the past owing to changes in the circumpolar trough's position, the frequency of synoptic systems and changes in atmospheric circulation, the systematic shift in mean cyclone trajectories, sea ice coverage, and other factors (Godfred-Spenning & Simmonds, 1996; Schlosser & Oerter, 2002).

Chapter 2

Data and Methods

This chapter describes the types of data used, the study region considered in the thesis, and the various orographic and topographic features that it contains. Further, this chapter explains the details of the regional modeling using the Polar WRF model, including model validation, sensitivity studies, and selected combination of parameterization schemes for extreme precipitation events (EPEs) related studies. The usage of different reanalysis, satellite data, and in-situ observations are also explained briefly, along with the introduction of methods used in annual dating for ice core data. This chapter further explains different methods used throughout this work and related details.

2.1 Study area

Dronning Maud Land (DML) is located mainly in the Indian and Atlantic Ocean sectors of the Antarctic continent, spanning 20°W to 45°E in East Antarctica. This region is characterized by complex orography from the coastal sector to the inland regions (Rotschky et al., 2007). The geomorphology of DML sets it apart from other regions of East Antarctica, notably between 15°W and 30°E, where high mountains obstruct the ice flow towards the coast, resulting in a sharp transition from the polar plateau (>2,000 m above sea level (asl) to the coastal zone (<1,500 m asl) and ice shelf zone (< 100 m asl) (Broeke et al., 1999).

Coastal DML is distinguished by numerous topographic features, such as ice rises and ice rumples, which exert significant control over the regional precipitation distribution and surface mass balance (SMB) (Goel et al., 2020). The area is characterized by steep orography, particularly near the coast, with snow distribution strongly influenced by orographic features as well as wind-driven redistribution and sublimation across the grounded ice sheet (Reijmer et al., 2004; Thiery et al., 2012). Further inland, the Antarctic ice sheet's elevation rises to around 3,700–4,000 m asl and has a dome-shaped form. The gravity-driven katabatic winds resulting from the pressure gradient force between inland and coastal regions are a particular feature of the continent. The wind speed is maximum on the slope and is highest in the region with a steep slope toward the Antarctic plateau. Coastal DML is also fringed by several ice shelves extending northward from the coast. Twelve research stations are situated in the DML region and are operated by India, Japan, Russia, Germany, Norway, and Belgium. Figure 2.1 shows various features of DML, with selected coastal stations and ice core locations referred to in this study also indicated.

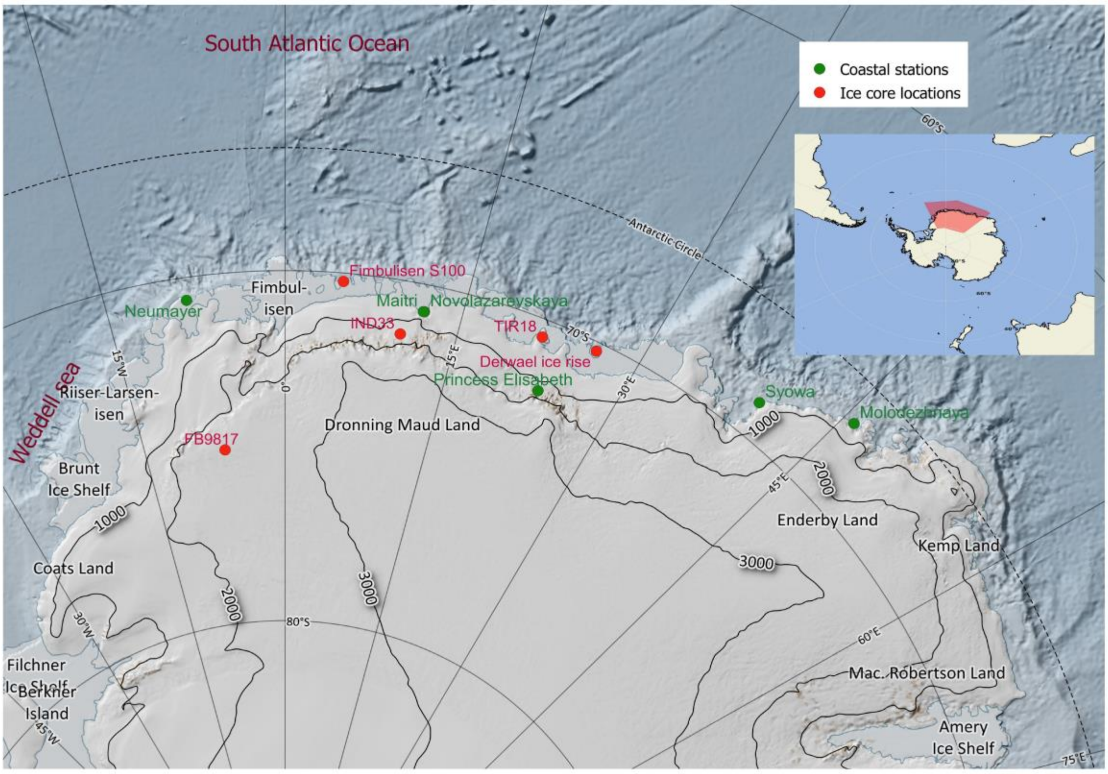

Figure 2.1: The location of Dronning Maud Land (DML) with selected ice core sites (red dots) and coastal stations (green markers) from where in-situ data are used is indicated. Elevation contours and a number of ice shelves are also shown. The inset figure shows the location of Antarctica within the Southern Hemisphere with DML shaded.

2.2 Reanalysis and satellite data

2.2.1 Reanalysis data

Reanalysis datasets are created by merging model forecast data with in-situ observations using a data assimilation technique and producing the most accurate estimates of the atmospheric state, considering the limited amount of data available at high latitudes. The data assimilation schemes are global and generate fields at high horizontal (~31 km resolution) resolution. This study used several reanalysis datasets available over the Antarctic at various spatial and temporal resolutions.

ERA5: The fifth and latest version of ECMWF's reanalysis (ERA5) has global coverage and a horizontal resolution of 0.25° × 0.25°, and fields are available every hour on a number of pressure levels (Hersbach et al., 2020). ERA5 employs the Integrated Forecast System (IFS), which is produced utilizing a 4D-var data assimilation scheme. ERA5 has been shown to give the best performance in terms of precipitation and other near-surface parameters over Antarctica compared to other reanalyses (Gossart et al., 2019; Tetzner et al., 2019). While differences exist in precipitation values across various reanalysis datasets, ERA5 agrees well with observed spatial variability and seasonal patterns in precipitation, corroborated by satellite measurements (Liu et al., 2019; Roussel et al., 2020) and is still the best available high-resolution data for the study of extremes in Antarctica. Surface and upper-level data from ERA5 were employed here, including precipitation, 10-m wind, 2-m temperature, integrated water vapor transport, MSLP, specific humidity, and 500 hPa geopotential height.

The precipitation in the various reanalysis and atmospheric models show differences in magnitude (Bromwich et al., 2011; Tang et al., 2018). Notably, a recent investigation conducted by González-Herrero et al. (2023) underscores a significant two-fold difference in the magnitude of extreme precipitation between a regional model (RACMO2) (van

Wessem et al., 2018) and ERA5. Regardless of the difference in the amount of precipitation, these datasets show similar results in the dates of extreme events, long-term analysis, and spatial distributions (González-Herrero et al., 2023). While the magnitude uncertainty is a crucial consideration in studies concerning precipitation, it does not affect the overall validity of the results, such as long-term trends, the count of EPEs, and spatial variabilities (in Chapter 3).

Other reanalysis data used: We extracted precipitation from three additional reanalysis products with different spatial and temporal resolutions to compare their representation of precipitation distribution for the case study of an EPE (Chapter 4). The reanalysis used for EPE day, 8 November 2015, were MERRA2 (0.5° × 0.625°, hourly), JRA55 (1.25° × 1.25°, 6-hourly), CFSv2 (0.5° × 0.5°, hourly).

2.2.2 Satellite data

Satellite images were used in the EPE case study (Chapter 4) to analyze the cloud band structure during the event. The Antarctic satellite composite imagery is a mosaic of geostationary and polar orbiting satellite imagery (Kohrs et al., 2014; Lazzara et al., 2003). Data from the geostationary satellites (GOES-Geostationary Operational Environmental Satellite, Himawari, and Meteosat) are combined with polar-orbiting satellite imagery. This is from the NOAA (National Oceanic and Atmospheric Administration) satellites, also known as POES (Polar-orbiting Environmental Satellite), Terra/Aqua, and Metop satellites. The composite is made hourly and is created at several spectral channels. This study used infrared (IR - 10.7 microns) and water vapor composites (6.7 microns) to track the development of cloud and water vapor features.

2.3 The regional modeling approach

Atmospheric reanalyses provide valuable insights into synoptic-scale features across the Antarctic continent, albeit at moderate spatial and temporal resolutions (J. M. Jones et al., 2016). However, due to the intricate orography of the coastal area and the coarse grid resolutions of global reanalysis fields, these products often fail to capture small-scale atmospheric features, such as narrow frontal bands (Deb et al., 2018). Furthermore, the paucity of long-term, in-situ data coupled with the extreme, remote conditions prevailing over the Antarctic continent contribute to inconsistencies in the performance of reanalysis systems over the ice sheet. Considering these limitations, this study employs the output of a high-resolution regional model to provide a more detailed analysis of extreme events and to explore the influence of coastal orography on the spatial distribution of precipitation during such events.

Two modeling experiments were conducted in this study. The first one optimized and validated the regional model's ability to capture atmospheric processes during the evolution of a synoptic cyclone. Additionally, sensitivity experiments were carried out to refine the parameterization schemes. The outcome of this work aided the selection of the most suitable model configuration for subsequent analyses. Then, using the optimized model configuration, integrations were carried out dedicated to model an EPE event with the highest snowfall over DML during the 40-year period (Chapter 4). Using the selected model setup, this simulation aimed to provide insights into the dynamics of the event.

In the subsequent sections, the study provides a comprehensive overview of the regional model employed in this study. The detailed descriptions of the simulations conducted, their methodologies, and the results obtained are included in annexure 1.

The Polar Weather Research and Forecast Model (Polar WRF): The polar meteorology group at Ohio State University created version 4.1.1 of Polar WRF, which is utilized as a limited-area meteorological modeling system for polar regions (Bromwich et al., 2004). It uses fully compressible Euler non-hydrostatic equations on a horizontal Arakawa C-grid. The model uses a hybrid vertical coordinate system, aligning levels with the terrain near the surface and transitioning to pressure levels at higher altitudes. A third-order Runge-Kutta scheme is employed for time-split integration. For a better depiction of physical processes in polar regions, the standard WRF model version 4.1.1 has been optimized for polar conditions such as sea ice fraction and thickness, snow depth, snow albedo, cloud radiative process, and improved heat transfer of ice and snow. For this study, the basic configuration for the Polar WRF model was taken from the Antarctic Mesoscale Forecast System (AMPS), a numerical weather prediction tool for the Antarctic that is run by the US National Center for Atmospheric Research (NCAR).

2.3.1 Evaluation and validation of the Polar WRF model over DML

The performance of the Polar WRF model in simulating a synoptic cyclone that occurred over the coast of DML from 12 to 17 April 1992 was investigated. The model simulated variables were compared to in-situ meteorological observations from coastal DML stations, including Neumayer (Germany), Syowa (Japan), Novolazarevskaya (Russia), and Molodezhnaya (Russia). Also, the model sensitivity to parameterizations, including the PBL, cloud microphysics, and longwave radiation, was analyzed. The model performance was assessed through an analysis using statistical significance tests, correlation, Root Mean Square Error (RMSE), and bias values.

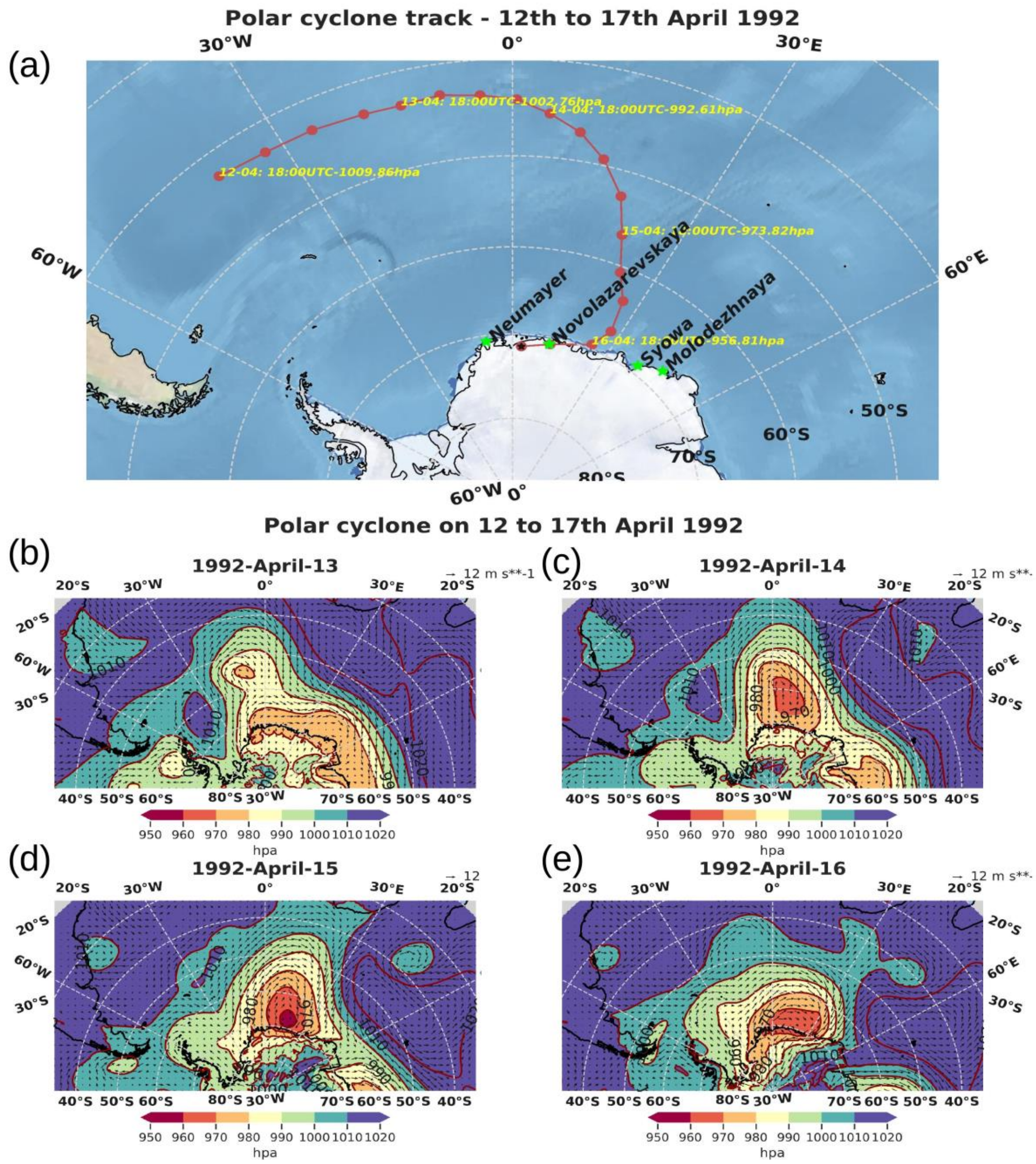

Figure 2.2: a) Track of a cyclone making landfall in coastal DML from the Melbourne University cyclone tracking scheme. The figures are also marked with locations of coastal stations, where in-situ data are available. b) MSLP and wind vectors on 13 April 1992, c) 14 April 1992, d) 15 April 1992, e) 16 April 1992.

The genesis of a cyclone that took place over the Southern Atlantic (45ºS, 40ºW) on 12 April 1992 and made landfall on the coast of DML on 17 April 1992 was selected for simulation as it made landfall on the DML coast and affected coastal stations. Figure 2.2 shows the cyclone's track and atmospheric conditions throughout its lifespan. The cyclone followed an eastward track during the initial days after formation. It moved to the coastal region on 14 April 1992 with the formation of a high-pressure area on the eastern side of the Atlantic Ocean that acted as a block to the low's eastward movement. Upon reaching the coast, the low moved towards the west on 16 April 1992 under the influence of an inland extended high-pressure ridge over the east side of DML. The landfall of the cyclone and associated changes in the lower atmosphere were identified in the observed surface meteorological observations from coastal stations.

Further details about the Polar WRF model simulation of the polar cyclone, including model domains, methodology, results of model validation experiments, and sensitivity studies for the selection of parameterization schemes, are explained in Annexure 1.

2.3.2 Simulation of an EPE using Polar WRF

The role of the DML complex orography in the precipitation distribution during an EPE event is investigated in detail using Polar WRF. The parameterization schemes are selected based on the sensitivity analysis that identifies the best-performing schemes in the PBL, longwave radiation, and cloud microphysics. Table 2.1 presents the physics options utilized in the EPE case study.

Model configuration	**Physics scheme/ details**
Longwave radiation scheme	Rapid Radiative Transfer Model for general circulation model (RRTMG)
Shortwave radiation scheme	Goddard shortwave scheme
Cloud microphysics	Morrison 2-moment scheme
Land surface physics	Unified Noah Land Surface model

Planetary Boundary layer physics	MYNN level-2 scheme
Surface layer physics	Revised MM5 Scheme
Cumulus parameterization scheme	Kain-Fritsch scheme

Table 2.1: Parameterization schemes used for the EPE case study

The EPE on 8 November 2015 was selected for this case study as there was the highest daily precipitation (33 mm) at the ice core site IND33(71.51°S,10.15°E) for the 40-year period 1979 – 2018. More details are provided in Chapter 4. For this simulation, the model was run with a 9 km parent domain, with an inner domain of 3 km covering the area primarily influenced by the event. The nested models were on a polar-stereographic projection (Figure 2.3). To supply the required surface, lateral boundary conditions, and initial conditions such as sea surface temperature and sea ice concentration, the study used ERA5 reanalysis data. This data was available at a high resolution of 0.25° × 0.25° spatially and hourly temporally. The 10-day model simulation was started at 00 UTC on 3 November and ran to 18 UTC on 12 November 2015, with a temporal resolution of 1 hour. Surface meteorological variables observed at Neumayer and Princess Elisabeth (PE at 71°57′S, 23°21′E), were utilized to validate the model output (Figure 2.4).

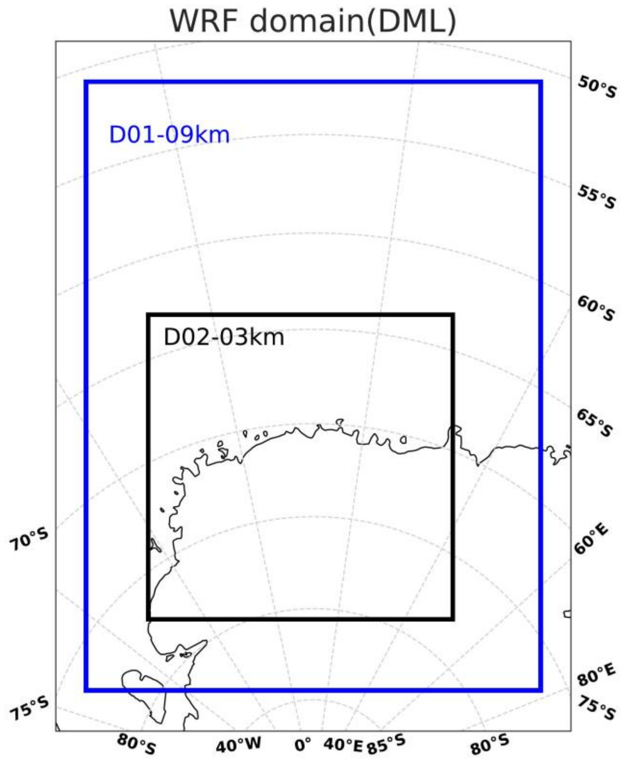

Figure 2.3: Polar WRF domains used for the EPE case study simulation. Within the parent domain (9 km) is nested the inner domain (3 km) over the coastal region.

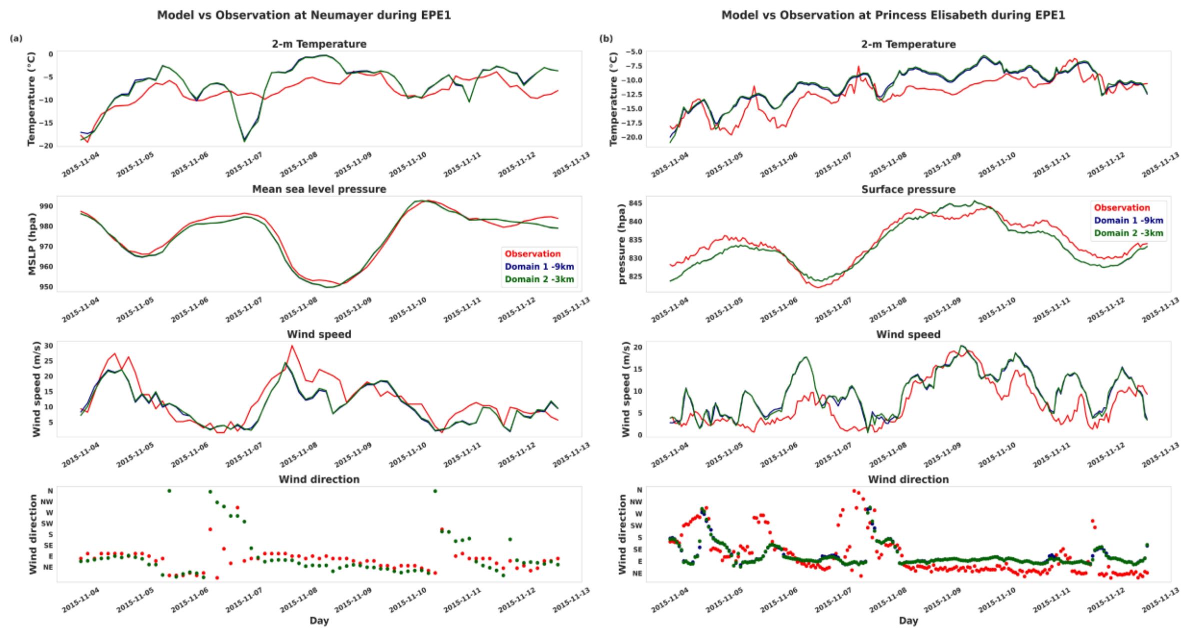

Figure 2.4: (a) The validation of the Polar WRF model outputs from both model domains. Time-series comparison of model output from the nearest grid point of observed values at Neumayer for the ten days from November 4 to November 12, 2015. (b) same as (a) for the PE station

We compared these observed variables with the model's nearest grid point values, demonstrating the accurate representation of surface variables by Polar WRF during the precipitation event. The performance was assessed using statistical measures, including correlation, RMSE, and bias (see Table 2.2). At the PE station, there was a significant ($p < 0.05$) strong correlation between the model and in-situ surface variables of 2-m temperature (r value = 0.85), wind speed (r value = 0.76), and surface pressure (r value = 0.94). Although there was a slight overestimation of temperature of 1.4°C and wind speed (2.6 m s^{-1}), the model effectively captured the abrupt changes and temporal variability during the event. However, the model failed to capture the sudden changes in wind direction from easterly to north-westerly and overestimated the wind speed on 6 and 7 November 2015. The model also underestimated the 2-m temperature (~ 5°C) at Neumayer on 7 and 11 November, before and after cyclone landfall, as indicated by changes in MSLP values. The model incorrectly had the wind direction as NW-N instead of SW-S on 7 November, resulting in a sudden temperature drop. Similarly, on 11 November, the model misrepresented the wind direction as SW-S instead of SE, contributing to the cold bias. Despite these discrepancies, the model performed well overall, with precipitation at PE and Neumayer, as indicated by the model-to-observation comparison statistics (Table 2.2).

(a) Neumayer station	2-m temperature (°C)		Wind speed (m s^{-1})		MSLP (hPa)	
	Domain 1	Domain 2	Domain 1	Domain 2	Domain 1	Domain 2
Correlation ($p < 0.05$)	0.71	0.72	0.82	0.82	0.98	0.98
RMSE	3.43	3.42	8.45	8.33	2.14	2.11

Bias	1.65	1.56	-1.86	-1.76	-0.97	-0.91

(b) PE station	Surface temperature (°C)		Wind speed (m/s)		Surface pressure (hPa)	
	Domain 1	Domain 2	Domain 1	Domain 2	Domain 1	Domain 2
Correlation ($p < 0.05$)	0.85	0.84	0.77	0.75	0.94	0.94
RMSE	2.23	2.39	4.34	4.43	2.25	2.27
Bias	1.57	1.73	2.78	2.78	-1.10	-1.10

Table 2.2: Comparison of observed surface meteorological values from coastal stations Neumayer and PE and the model outputs of Polar WRF. The model output was obtained from the nearest grid points in Domain 1 (9 km) and Domain 2 (3 km). The comparison used statistical metrics, including correlation, RMSE, and bias. (a) for Neumayer and (b) for PE.

2.3.3 Other regional model output used

RACMO2.3p2: The Regional Atmospheric Climate Model (RACMO2) is designed for glacier regions such as Greenland and Antarctica (Reijmer et al., 2004). It integrates the dynamical core of the High-Resolution Limited Area Model (HIRLAM) with the physics from ECMWF's Integrated Forecast System (IFS). RACMO2 employs a hybrid vertical coordinate system, combining terrain-following sigma levels near the surface with pressure levels higher in the atmosphere. For the simulations, the model used resolutions of 27 km, 5.5 km, and 40 vertical layers. ERA-Interim reanalysis data drove lateral boundaries and ocean conditions, while the domain interior was allowed to evolve independently. The model is coupled with a multi-layer snow model to handle melt, refreezing, percolation, and meltwater runoff. It assumes hydrostatic equilibrium and incorporates various parameterizations, including snow albedo, calculated using a predictive scheme for snow grain size. The drifting snow scheme models the interaction between drifted snow and the surface and lower atmosphere. The current version includes improvements such as upper-air relaxation, updated orography, refined cloud scheme parameterizations, and adjusted snow properties to enhance performance over the Antarctic ice sheet. For this study, the dataset on surface mass balance (SMB), precipitation, and surface wind components over DML at 5.5 km spatial resolution (van Wessem et al., 2018) was utilized to ensure accurate comparison with in-situ surface snow height measurements.

MAR v3.11: The "Modèle Atmosphérique Régional" (MAR) model was created to study climate in high-latitude regions (Gallée & Schayes, 1994). MAR is a regional hydrostatic atmospheric model based on primitive equations (Agosta et al., 2019; Kittel et al., 2018), with a horizontal resolution of 35 km specifically for Antarctica. It incorporates parameterization schemes for cloud microphysics, snow properties (Gallée & Schayes, 1994), snow particle sublimation, and radiative transfer across the snow surface (Morcrette, 2002). Additionally, the model employs a one-dimensional multi-layered energy balance scheme to simulate snow properties, surface albedo, and the refreezing of meltwater (Fettweis et al., 2017). MAR v3.11 utilizes ERA5 reanalysis data for its input, running on a polar stereographic projection and incorporating Bedmap2 data for Antarctic topography. The model includes a drifting snow scheme to simulate surface mass balance components (Amory et al., 2021).

2.4 In-situ data from coastal DML stations

The in-situ meteorological measurements from several coastal stations over DML were used in this study. The details of the surface observations used for model validations have been discussed in Annexure 1. Along with that, this work also used meteorological variables, such as hourly snowfall rate and surface snow height measurements from the PE station located at 71°57′S, 23°21′E, 1392 masl, and 173 km from the coast. The Belgian PE station is located to the north of the Sør Rondane Mountain Range, which stretches approximately 220 km from east to west. The area surrounding the observatory experiences significant fluctuations in accumulation and strong katabatic winds coming from inland. Despite this, the observation site is positioned closer to the Sør Rondane Mountain Range and is partially shielded from the intense katabatic winds (Gorodetskaya et al., 2013).

Snow surface height values: The automatic Weather Station (AWS) at PE (see Figure 2.5) is on a flat snow surface and has been operational since February 2009. Its primary advantage is its ability to record snow depth and meteorological conditions. The AWS collects hourly average data on various surface variables, including near-surface air temperature, relative humidity, surface pressure, wind speed and direction, radiative fluxes, and snow height measurements (Gorodetskaya et al., 2013). Snow height data from 2009 to 2019 are available, though there are gaps in 2014 and 2015 and some additional short intervals. The sensor measures snow height hourly with an accuracy of 1 cm, providing data at an hourly resolution. The hourly data are resampled into daily SSH changes to reduce short-term variabilities. The change in daily SSH values is calculated by taking the difference between the daily mean snow height between consecutive days. Observed meteorological variables are used to analyze different atmospheric conditions associated with these SSH changes.

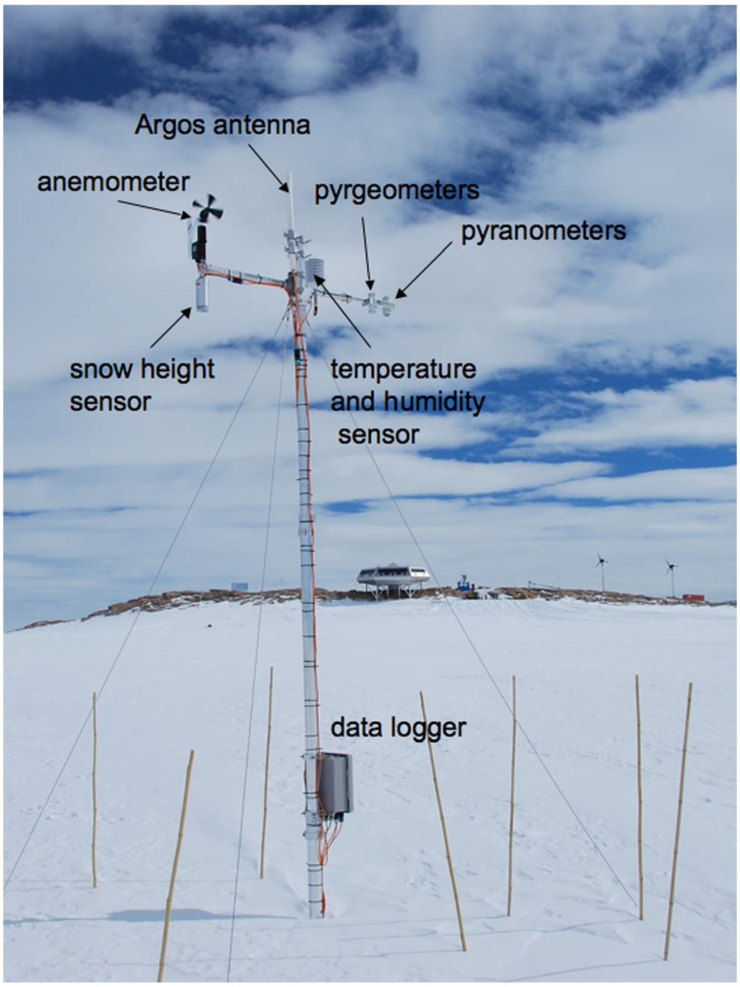

Figure 2.5: Image of the AWS at PE station with different sensors, including snow height, temperature, humidity sensors, anemometer, and pyranometer. (Gorodetskaya et al., 2013).

Micro rain Radar data for hourly snowfall rate: The cloud/precipitation/meteorological observatory at the PE station, provided the precipitation readings for selected case studies of EPEs. Hourly snowfall values have been recorded via a Micro Rain Radar (MRR) at this observatory since 2010, and the radar variables such as mean Doppler velocity or effective reflectivity factor (Ze) have been used to calculate precipitation rates. The derivation of the snowfall rate (SR) - Ze relationship needs information on snow particle microphysics or particle size distributions, which are measured using an optical disdrometer. Thus, the calculation of Ze, SR, and the parameters of the Ze-SR relationship is used to process the precipitation rate (mm/hr) at PE (Souverijns et al., 2017). This study used the hourly snowfall rate at PE available for the year 2015, which is published and accessible (Souverijns et al., 2017).

2.5 Ice cores

Due to its extreme remoteness and harsh environment, Antarctica has limited in-situ meteorological observations. Proxy climate data, such as ice core records, can be used to determine changes in atmospheric conditions and climatic parameters over periods from the annual to the millennial timescales, assuming we understand how climate information is expressed in the climate proxy. Annually-resolved high-resolution ice core-based proxy records from high-accumulation regions in Antarctica offer a reliable method of studying Antarctic climate change and understanding multidecadal and shorter climate variability over the last millennia, and seasonal variations can also be assessed using snow isotopic compositions at high-accumulation sites in coastal Antarctica (Ejaz et al., 2021; Jouzel & Merlivat, 1984; Morgan, 1985; Stenni et al., 2016).

Ice core drilling sites are carefully selected based on ground-penetrating radar (GPR) and satellite data, which provide information on accumulation rates, bed characteristics, ice flow velocity, and direction. Establishing a precise age model for an ice core is crucial in achieving accurate high-resolution climate studies. This process begins with a preliminary timeline created by manually counting annual layers in the $\delta^{18}O$ record, focusing on seasonal signals - summer maxima and winter minima (Dey et al., 2023). Sections of an ice core are further analyzed for various measurements, including stable isotopes of water (oxygen and hydrogen), trace elements, atmospheric dust, and major ions. Counting annual layers is the most exact technique for establishing the ice age (Dey et al., 2023). To refine the chronology, the non-sea-salt sulfate record is plotted against the first-order chronology, pinpointing recognized volcanic events by analyzing distinct peaks in the sulfate record. The volcanic ash layers are often considered good chronological markers, where volcanic eruptions produce distinct layers of ash that settle over large areas and are subsequently buried by snowfall, becoming preserved within the ice. Because the timing of many volcanic eruptions is well-documented through historical records and other geological evidence, these ash layers can be precisely dated (Hammer et al., 1978). Furthermore, age modeling refines the chronology by deriving ages for sub-sampling depths through linear interpolation between two annual layers. However, it's important to recognize that age-depth relationships often exhibit non-linear characteristics, and using linear interpolation along with tuning the chronology with tie points may introduce uncertainties into the ice-core age model. Thus, an uncertainty of ±1 to 2 years is often considered in annual dating in ice cores. Also, isotope diffusion, wind-driven redistribution, sublimation, and condensation can complicate the δ18O record from ice cores (Mahalinganathan et al., 2022; Münch et al., 2017).

Several ice cores were drilled in DML, both at coastal sites and in inland regions (Thomas et al., 2017). This study used the annual accumulation values from several of these cores (discussed in Chapter 5), which cover the reanalysis data period (from 1979), for relevant analysis on the role of meteorological extremes in shaping annual ice core accumulation.

2.6 Methods

2.6.1 Identification of EPEs

Over Antarctica, several studies on high-precipitation events have been carried out using available short and long-term datasets and used different methods to identify these events (Schlosser, Manning, et al., 2010; K. E. Sinclair et al., 2010; Swetha Chittella et al., 2022). The climatological occurrence of EPEs over Antarctica was determined using threshold criteria applied to precipitation time series. In most studies, the threshold value was taken as either a high percentile value (Turner et al., 2019; Welker et al., 2014; Yu et al., 2018) or twice the standard deviation plus the average value (Schlosser et al., 2010) of the entire time series. Here, an EPE day is defined as a precipitation day (precipitation >0.02 mm) with daily total precipitation greater than the 95th percentile at a location, based on a 40-year climatology (1979 - 2018). Spatial variability in the 95th percentile values was also analyzed to understand the influence of the complex orography on precipitation distribution.

By applying the 95th percentile threshold criteria to the time series of precipitation at each grid point for the 40-year study period, variables such as precipitation, 10-m winds, 2-m temperature during EPE days, and the spatial pattern of the total number of EPE days, were found for each latitude-longitude grid point over the region. Daily anomalies were calculated using the mean value for each day for the climatological period 1979–2018 for temperature, MSLP, and 500 hPa geopotential height. The climatological analysis (Chapter 3) also identified the seasonality of EPE occurrences by calculating seasonal variabilities in contribution to annual precipitation, total number of EPE days, temperature anomalies, and changes in seasonal 95th percentile values.

For the case study of an EPE event (Chapter 4), the extreme values of various meteorological parameters in the upper and lower atmosphere were considered as those exceeding the 99th and 95th percentiles and less than the 5th and 1st percentiles compared with daily data for 1979-2018 for each latitude-longitude grid. The variables 500 hPa geopotential height, MSLP, wind component, IVT, precipitation, and 2m temperature were analyzed to determine the extreme conditions during this event

2.6.2 Directional wind constancy

Directional constancy (DC) is a measure to identify the persistency in wind direction for a given area. To determine DC during EPE days, we compared DC during these events with mean values for the region. DC is calculated by taking the ratio between the vector wind speed and the mean wind speed at 10 m (Bromwich, 1989; Ettema et al., 2010). If DC equals 1, the wind direction is constant, whereas a DC value of zero signifies that the near-surface wind direction is arbitrary over time.

$$dc = \frac{(\overline{u}^2 + \overline{v}^2)^{1/2}}{\overline{(u^2 + v^2)^{1/2}}}$$

Where v and u are the meridional and zonal components of the 10 m wind.

2.6.3 AR detection criteria

This study employed the AR detection algorithm outlined by Wille et al. (2021). This algorithm identifies periods of unusually high meridional integrated water vapor transport (vIVT) that exceed the 98th percentile every three hours, within the latitude range of 37°S to 85°S. An Atmospheric River (AR) is characterized as a persistent, narrow moisture band with elevated IVT values and a meridional span of at least 20 degrees. While the original algorithm utilizes both integrated water vapor (IWV) and vIVT for detecting ARs, this study focused solely on vIVT values. This choice was made because the meridional wind speed component, as captured by vIVT, better represents the dynamic processes leading to snowfall (Wille et al., 2021). To assess the contribution of ARs to extreme precipitation events (EPEs), we analyzed the AR landfall dates provided by the algorithm.

2.6.4 Self-Organizing Maps (SOMs)

SOMs are a widely used neural network method that uses unsupervised learning to analyze high-dimensional data by grouping similar patterns into a two-dimensional matrix of easily interpretable patterns (Cassano et al., 2015; Hewitson & Crane, 2002; Kohonen, 2012). This work uses the SOM algorithm to detect large-scale atmospheric circulation and identify diverse synoptic patterns responsible for EPEs. Selecting the right number of nodes to classify the input dataset is essential in SOM analysis. A larger number of nodes will reveal more in-depth circulation patterns, while fewer nodes will show the overall patterns of the investigated region (Cassano et al., 2015). The quantization error is an essential indicator for estimating how closely the SOM nodes align with the data. In determining the various moisture transport pathways responsible for EPEs in coastal DML, we employed the SOM technique to demonstrate several moisture transport patterns during EPEs over a selected ice core location (IND33). We used IVT patterns during these EPEs for the period 1979-2018 and the region of 90°W to 90°E and 20°S to 90°S. A 5 × 3 matrix with 15 nodes was chosen to perform the SOM analysis by comparing the quantization error values from various node combinations.

This study also employed several other techniques, including composite anomaly analysis of MSLP and empirical orthogonal function (EOF) applied to 500 hPa geopotential height anomalies during EPE days (Grotjahn et al., 2016; Yu et al., 2018) to analyze the synoptic patterns during EPEs. EOF analysis of atmospheric variables during EPEs produced a set of modes that could explain the synoptic pattern on EPE days. Further, this study utilized the non-parametric Mann- Kendall (MK) statistical test (Kendall, 1975; Mann, 1945) on the 40-year time series for each grid point to assess the significant trend over the region.

Chapter 3

The Spatial and Temporal Variability of Extreme Precipitation Events over Dronning Maud Land

Introduction

Understanding the distribution and variability of extreme precipitation events (EPEs) is crucial for comprehending the overall precipitation dynamics in Antarctica and their implications on ice-core climate records from Antarctic ice sheets. This chapter explains the climatological aspects of EPEs, using the high-resolution reanalysis data from the European Centre for Medium-range Weather Forecasts (ECMWF) by examining the spatial and temporal variability of EPEs over the Dronning Maud Land (DML) region, East Antarctica for 40 years (1979–2018). This chapter examines the spatial changes in 2-m temperature and 10-m wind components during EPEs and compares them with climatological values. To further understand the variability of EPEs in the coastal and inland regions, the study focuses on six ice-core locations that represent both low-elevation coastal locations (altitude < 2,000 m) and the high-altitude interior, East Antarctic Plateau (EAP) region (altitude > 2,000 m). Using the temporal occurrence pattern of EPEs at these ice-core locations, this chapter analyzed the interannual and seasonal variability of EPEs occurrence, the factors controlling this variability, and the synoptic environment in which they occur. This chapter also considers the spatial trend of EPE days and the contribution from ARs to EPEs over the selected locations to identify their regional differences.

3.1 Spatial and temporal distribution

3.1.1 Spatial distribution of EPEs and their characteristics

3.1.1.1 Precipitation pattern and the complex orography of DML

The characteristics and distribution of precipitation during EPE days compared to the annual mean values are shown in Figure 3.1. It also shows the elevation contours across DML, with the regions with closer contours highlighting the locations of steep orographic gradients. The annual mean precipitation is high near the coast but decreases inland (Figure 3.1a). The precipitation distribution has alternate maximum and minimum values near these coastal orographic features, with maximum precipitation on steep east-facing slopes. The ice shelves, especially the ice rise areas near 35°E and 5°W, have the largest values (~800 mm year^{-1}). Further inland, the Antarctic ice sheet's elevation rises to around 3,700 to 4,000 m above mean sea level (AMSL) and has a dome-shaped form. The lack of moisture and very low temperatures lead to much lower precipitation amounts over these inland regions. Figure 3.1b shows the annual mean precipitation on EPE days, and when compared to climatological yearly mean precipitation, it shows a similar distribution pattern with a considerable difference in magnitude. This implies that these top 5% precipitation events (EPEs) significantly affect the spatial distribution of total annual precipitation. The precipitation over the continent's interior comes mainly from clear sky precipitation, and the contribution from EPEs is less over these regions due to infrequent warm air intrusions from ocean regions.

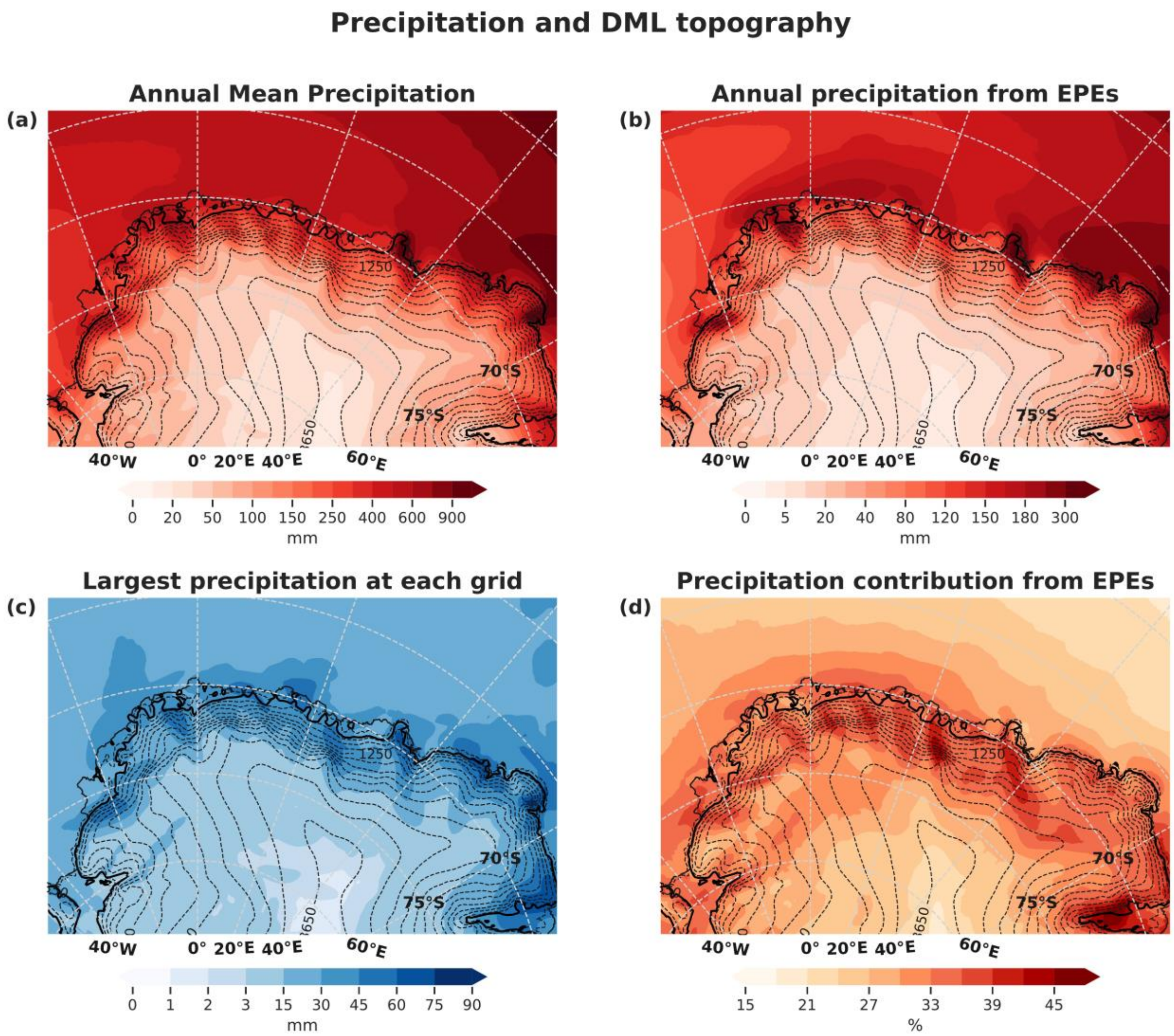

Figure 3.1. (a) Annual mean precipitation, (b) annual mean precipitation from EPEs, (c) largest precipitation values at each grid, (d) percentage contribution to annual total precipitation from EPEs. All the figures are overlayed by the orography from ERA5 data. The contour interval is 200 m.

The largest 1-day precipitation at each grid point (Figure 3.1c) demonstrates the landfall of these single-day precipitating events on the windward (eastern) side of these orographic features. EPEs with 70–80 mm day^{-1} of precipitation occur close to these orographic features due to steep slopes leading to the uplift of warm, moist airmasses from low latitudes (Welker et al., 2014). The contribution from EPEs (Figure 3.1d) to the total annual precipitation shows that the maximum values are found a little farther south (around 72°S). The contribution is more significant near orographic features with steep gradients along the coast than in the vicinity of ice shelves and ice rises. The leading cause of this spatial difference between near steep-gradient and more coastal orographic features is the landfall of severe precipitation episodes. Overall, the EPEs contribute roughly 35%–40% of the total annual precipitation, and the maximum impact of EPEs can be seen in regions with steep orographic gradients. The contribution of EPEs to yearly total precipitation declines further inland from the coast following the region's orography.

3.1.1.2 Spatial distribution and variability in the total number of EPE days

The total number of EPE days at each grid point has been analyzed (Figure 3.2a), which aimed to identify regional differences in the number of high-precipitation days. The spatial distribution of the total number of EPE days (Figure 3.2a) overlaid with elevation contours and wind vectors during EPEs illustrates the interaction of wind flow with the region's complex orography. The spatial variability in the number of EPE days has a pattern with high values over the ocean, coastal, and steep gradient high elevation locations over the interior, and low values on the leeward side of these coastal and inland high orographic regions (leeward side with respect to wind vectors during EPEs). The frequent interaction of easterly to north-easterly winds with these high orographic regions, which often transport large amounts of moisture from the ocean during EPEs, can be linked to regional differences in EPE days across these orographic features. Owing to the substantial intrusion and interaction of moisture with these steep gradient regions and the resulting large amount of precipitation from EPEs, inland regions (around 71°S to 72°S) with a steep elevation gradient have more EPE days. Due to the limited number of these intense EPEs, the leeward side of these inland high orographic regions has a minimum number of EPE days.

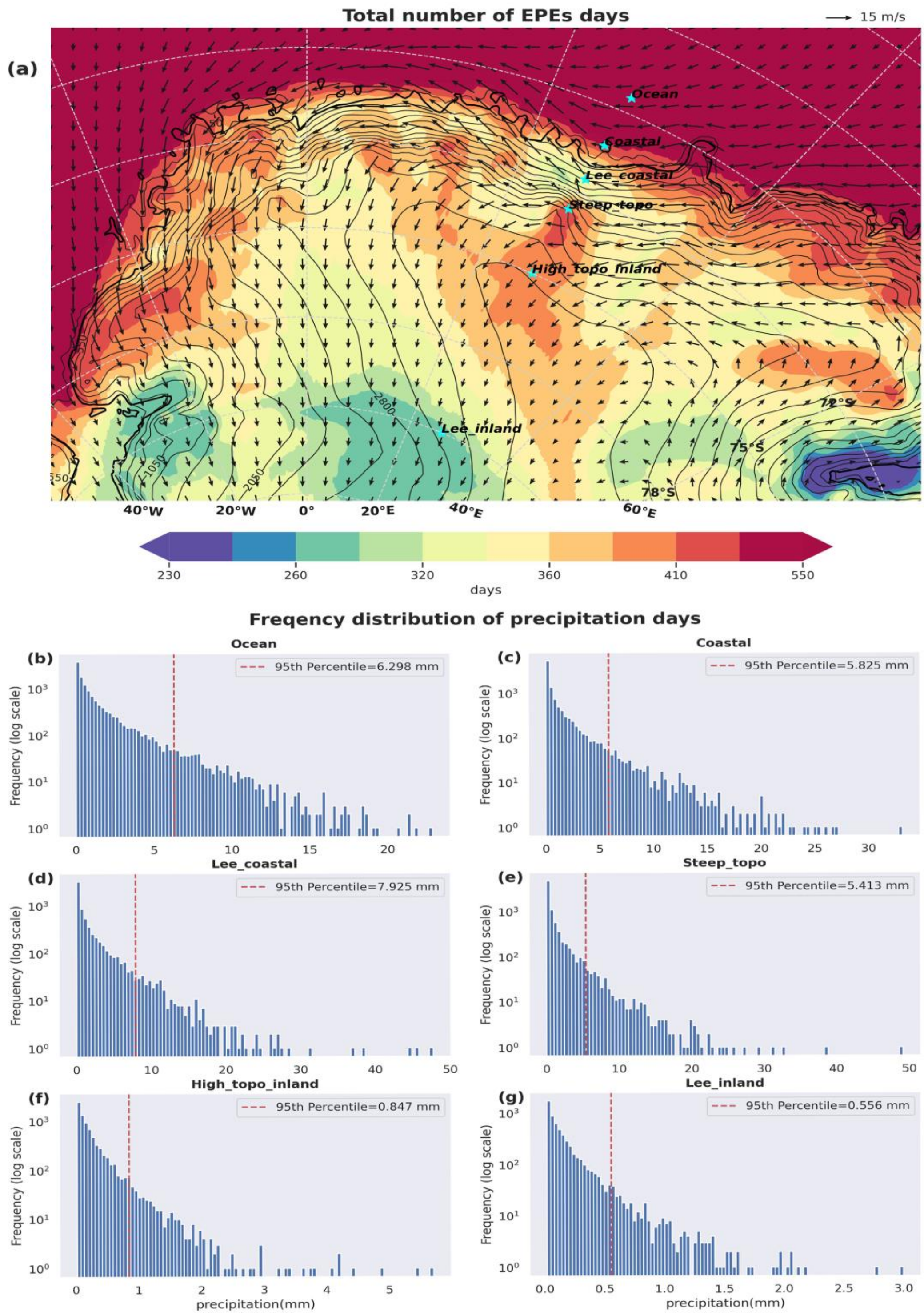

Figure 3.2: (a) Total number of EPE days for the period 1979–2018 overlayed with the orographic height and vectors of mean wind during EPEs. The lower six figures show the frequency distribution of precipitation days (precipitation value >0.02 mm) in 100 equal bins of precipitation values on the x-axis and the frequency of days in the log scale on the y-axis. Locations shown are (b) ocean, (c) coastal, (d) lee side of coastal orographic features, (e) steep topographic region, (f) high topographic region inland, and (g) lee side of the high orographic region. The red dotted vertical line shows the value of the EPE threshold (95th percentile).

Dry northerly to northeasterly downslope winds across 0 – 20˚E predominated during the EPEs. The mean number of EPE days per year (Figure 3.3) shows a pattern similar to the total EPE days. Areas near the ocean and coastal regions demonstrate a greater frequency of EPE days. High-altitude areas with steep gradients exhibit 10–12 EPE days annually, aligning with the region's orography. Conversely, leeward areas have fewer EPE days per year, with inland leeward areas and the Amery Ice Shelf (~ 72°S, 73°E) area to the east of DML recorded the lowest number of annual EPE days (4–7 days). Recent case studies (Gehring et al., 2022; Terpstra et al., 2021) demonstrate the impact of heavy precipitation episodes on the complex terrain of coastal Antarctica and highlight the importance of the orientation and local processes associated with coastal orography in determining the spatial and temporal distribution of precipitation and snowfall microphysics. Thus, the selection of ice core sites over these regions with complex orographic must consider this high spatial variability in the distribution of EPEs.

The frequency distributions of daily precipitation values are illustrated for six different sites, ranging from over the ocean to the interior, each with varying numbers of EPE days (Figures 3.2b to 3.2g). This analysis provides insight into the range of precipitation values across these locations. The distribution has a long tail toward the right, with large extreme values found at the tail of the distribution. Locations with a longer tail or greater separation between the threshold (95^{th} percentile) value and the maximum precipitation exhibit a more extreme distribution. The ocean and coastal regions (Figures 3.2b and 3.2c) share a similar 95^{th} percentile precipitation value. These areas receive frequent precipitation occurrences and have a substantial number of days with heavy precipitation. The largest EPE threshold (95^{th} percentile) value among the selected points was found on the leeward side of coastal orographic regions (Figure 3.2d), indicating that these areas are prone to frequent events with high precipitation. However, near steep orographic regions (Figure 3.2e), the positively skewed long-tailed precipitation distribution has an extreme nature with a lower threshold value than lee-side coastal regions. Although the highest precipitation values in both regions (coastal lee side and near steep orographic regions) are comparable, the 95th percentile values varied based on extreme values (outliers), the shape of the distribution, and the spread of values in the two distributions. A smaller 95th percentile value and more EPE days imply that the precipitation events with large (small) magnitude are more frequent (less frequent) near these steep-orographic regions. High orographic regions inland (Figure 3.2f) also have more EPE days. Maximum precipitation of 5–6 mm day^{-1} is seen over these high interior regions, suggesting that moist airmasses occasionally reach far inland and cause many EPEs.

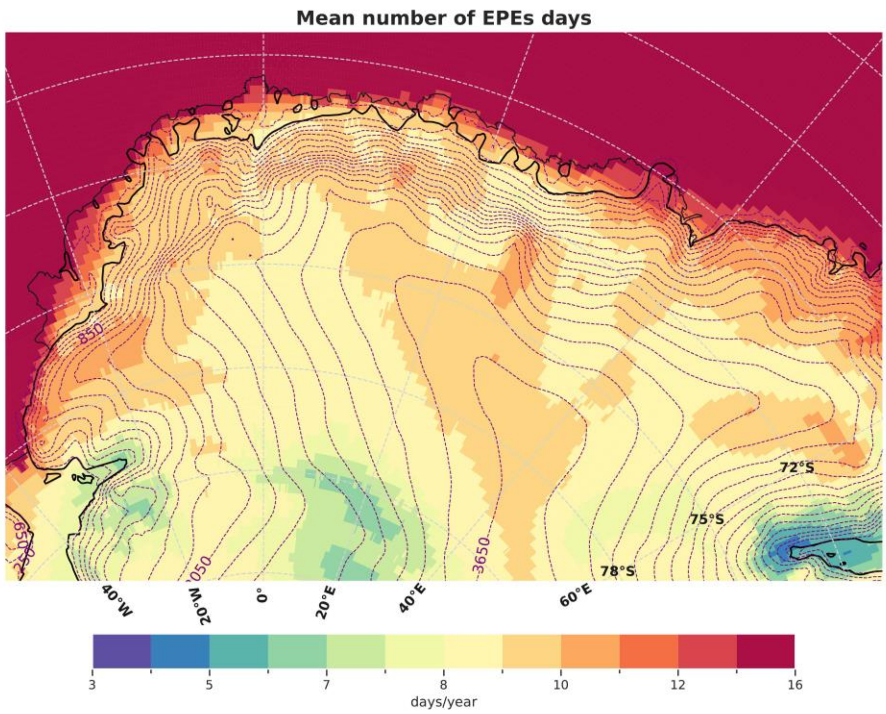

Figure 3.3: Mean number of EPE days per year for the period 1979-2018 overlayed by the orography.

The lee-sides of these inland high orography regions (Figure 3.2g) represent the inland precipitation pattern with a small precipitation magnitude and a less extreme distribution. Although clear sky precipitation or "diamond dust" dominates in these regions, some precipitation events with a daily precipitation total of 3 mm day^{-1} occur. This analysis provides details about the distribution of precipitation over different coastal and inland regions and the control of orographic features in the distribution of EPEs.

3.1.1.3 Seasonality of EPEs

This section explains the spatial variability of these EPEs during each season by categorizing months into the standard meteorological seasons, which are June, July, August (winter season), September, October, November (spring), December, January, February (summer) and March, April, and May (autumn) in the Southern Hemisphere. The contribution of EPEs during each season to the annual precipitation total is graphically represented in Figure 3.4, showing high spatial variability.

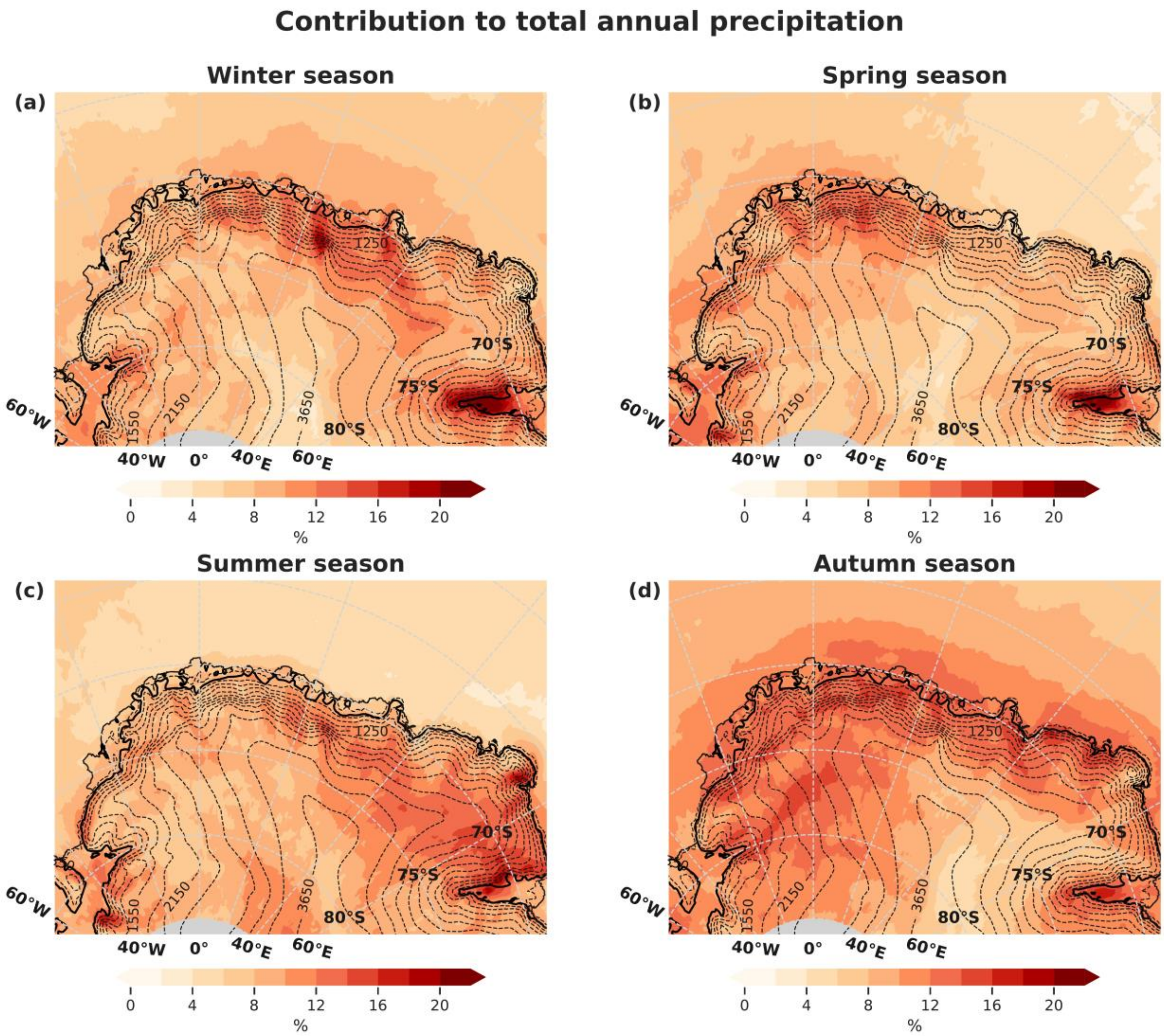

Figure 3.4: Spatial variability of contribution to total annual precipitation from EPEs (percent) during each season. (a) winter season, (b) spring season, (c) summer season, (d) autumn season. All the figures are overlayed by the orography from ERA5 data. The contour interval is 200 m.

Regional differences attributed to local orography are particularly notable near locations with a steep elevation gradient. Each season shows specific regions with dominant EPE contributions. Autumn boasts a wide range of precipitation contributions, significantly impacting coastal areas, especially the western part of DML and inland regions along the Greenwich meridian (0°E). EPEs in the winter season primarily influence central regions, demonstrating pronounced orographic effects on precipitation distribution. Both winter and spring seasons exhibit higher contributions over the Amery ice shelf area (~ 72°S, 73°E) compared to other seasons, with spring having a dominant influence on coastal areas ranging from 0°E to 30°E. Meanwhile, the summer season contributes significantly to the eastern part of DML, especially east of 30°E and north of 75°S. These regional variations are influenced by local factors, such as the formation of low-pressure systems in the circumpolar trough, resulting in maritime moisture intrusions, as well as the positioning of high-pressure and low-pressure dipole patterns in the oceanic areas north of DML (detailed analysis on Section 3.1.2.2). Additionally, tropical-polar teleconnections, such as ENSO, the Southern Annular Mode, and strong katabatic winds during the winter all shape the seasonal variations in EPEs over Antarctica (Turner et al., 2019). The mean number of EPE days during each season (Figure 3.5) exhibits a similar pattern to precipitation contributions. The autumn season has a high number of mean EPE days in the western and interior regions of DML, associated with the southward movement of the circumpolar trough. The winter season has a high frequency in the coastal and central areas. The summer season has an elevated number in the eastern region, extending into the continent's interior. These regional variations in EPE occurrence during each season are significant when interpreting stable isotope records from ice cores, as highlighted in previous studies (Laepple et al., 2018; Noone & Simmonds, 1998).

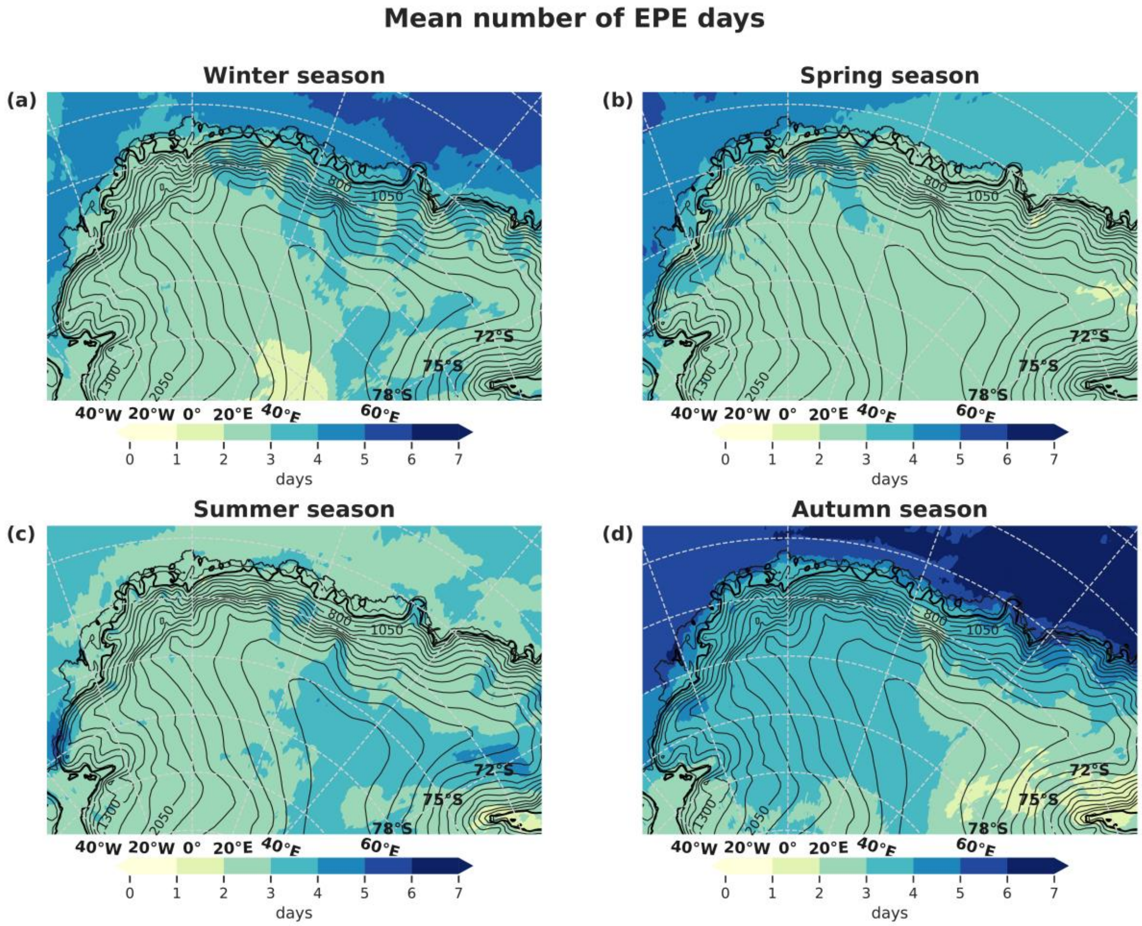

Figure 3.5: Spatial variation in the mean number of EPE days during each season. (a) Winter, (b) Spring, (c) Summer, (d) Autumn season. Orography details over the DML region are overlayed (black lines).

3.1.1.4 The meteorological environment during EPEs

Along with high precipitation values, the EPEs are often accompanied by anomalous changes in surface meteorological parameters, including strong winds and high atmospheric temperatures. The following section analyzes 10-m surface wind speeds and 2-m temperature values at each grid point during EPEs and compares them with climatological values. These sudden changes in surface meteorological parameters during EPEs can significantly impact the stable isotope records and initiate the redistribution of freshly precipitated snow, which can impact the ice core records.

3.1.1.4.1 Surface winds

The wind speed and directional constancy (DC) and a comparison of these quantities with the annual mean reveal that the direction and speed of the wind during EPEs and the annual mean wind differ noticeably (Figure 3.6). The yearly mean wind (Figure 3.6a) is characterized by strong downslope katabatic flow from the high elevation interior, with southerly to south-easterly winds along the coast and particularly over the region 15°E to 45°E with wind speeds of up to 12–15 m s^{-1}.

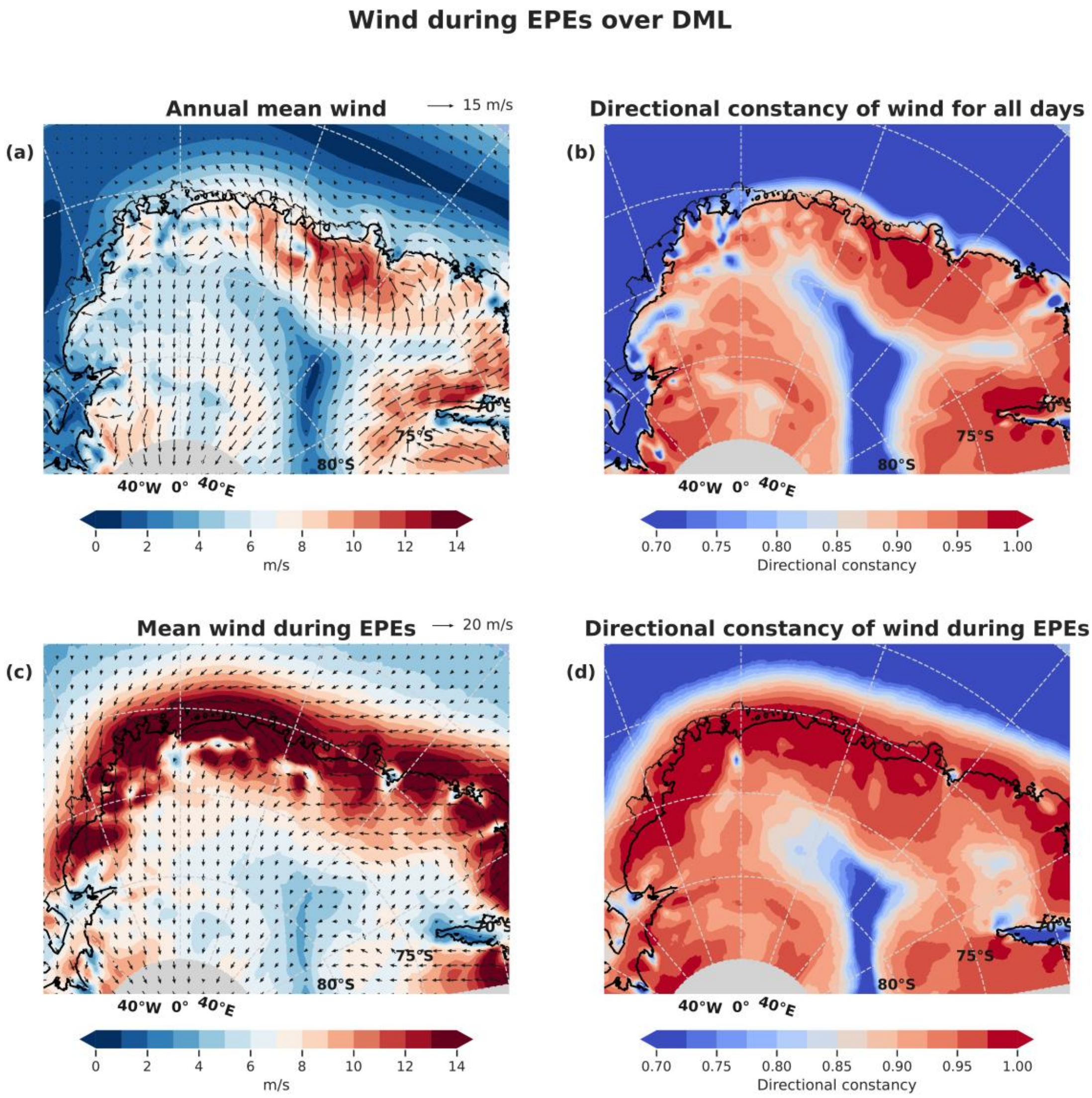

Figure 3.6: (a) Annual mean wind, (b) directional constancy for all days, (c) mean wind during EPEs, and (d) directional constancy during EPE days.

Compared to the interior high-elevation region, where wind direction is less consistent, the coastal area has a DC close to 0.95 (Figure 3.6b). However, during EPEs (Figures 3.6c and

3.6d), strong coastal easterlies interact with the complex orography, occurring under remarkably consistent patterns over most of the coastal regions (DC > 0.95). Strong coastal easterlies and north-easterlies replace katabatic winds during EPEs, causing warm, moist airmasses to be advected from the ocean. These winds have an average wind speed greater than 10 m s^{-1}, which is considered the threshold value for the snow starting to be lifted as blowing snow on the Antarctic ice sheet (King & Turner, 1997), especially over the coastal regions. This suggests that blowing snow can be expected during EPEs over the coastal region and that the orography influences wind speed distribution. High wind speeds during these precipitation events can affect post-depositional processes, including erosion, drift, vertical mixing, and blowing snow, all of which can affect the ice core proxy records (Fisher et al., 1985; Karlöf et al., 2005; Münch et al., 2017).

3.1.1.4.2 Temperature

The annual mean temperature of DML (Figure 3.7a) is relatively high along the coast and decreases inland. The temperature during EPEs has a similar distribution to the climatological values but with higher values (Figure 3.7b). The average temperature anomaly during EPEs (Figure 3.7c) illustrates that the interior ice sheet areas have positive anomalies of 10–12°, particularly across 75°S–78°S close to the Greenwich meridian (0–20°E). This region is on the lee side of the high orographic areas, characterized by dry downslope winds during EPEs. The maximum temperature anomaly values (Figure 3.7d) are similar to the mean anomaly distribution, with the continental interior having the largest anomalies (+23–25°C). Although EPE episodes are less frequent in the interior, they significantly impact the area's temperatures, with a mean anomaly of +10°C.

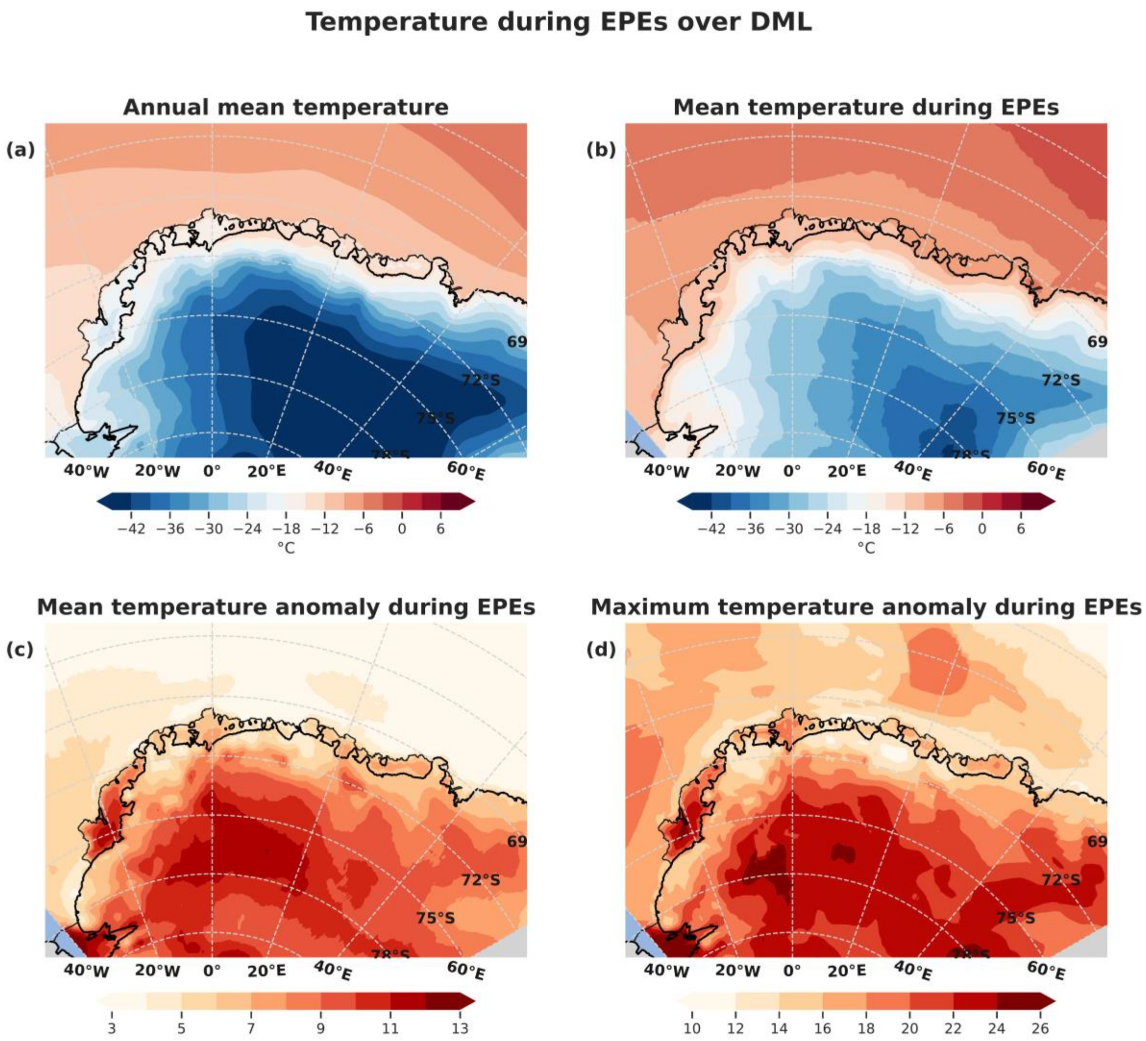

Figure 3.7: (a) Annual mean temperature, (b) mean temperature during EPEs, (c) mean temperature anomaly during EPEs, and (d) maximum temperature anomaly during EPEs over DML.

Extreme blocking events, warm air advection, cloud cover causing changes in longwave radiation, and strong dry winds contribute to temperature anomalies during EPEs (Hirasawa et al., 2000; Schlosser, Powers, et al., 2010; Servettaz et al., 2020; Turner et al., 2022), particularly in inland areas. When compared to interior sites, the coastal regions experience smaller temperature anomalies during EPEs due to frequent synoptic cyclone landfall and advection of warm airmasses.

When examining the seasonal distribution of temperature anomalies (Figure 3.8), it becomes evident that the largest positive anomaly values occur during specific seasons, most notably during the transition from winter to summer and throughout the summer months. These EPEs, occurring from September to February, exert a more substantial influence on the ice sheet, resulting in elevated temperature values surpassing the long-term average. EPEs give rise to positive temperature anomalies in the range of approximately 15–20°C in each season, with even more pronounced deviations observed in the inland regions of the ice sheet. The high-temperature anomalies during EPEs can cause a significant warm bias in the ice-core records (Jackson et al., 2022; Servettaz et al., 2020), and reconstruction of ice-core isotope data will overestimate reconstructed temperature if this warm bias is not considered (Noone & Simmonds, 1998; Servettaz et al., 2020).

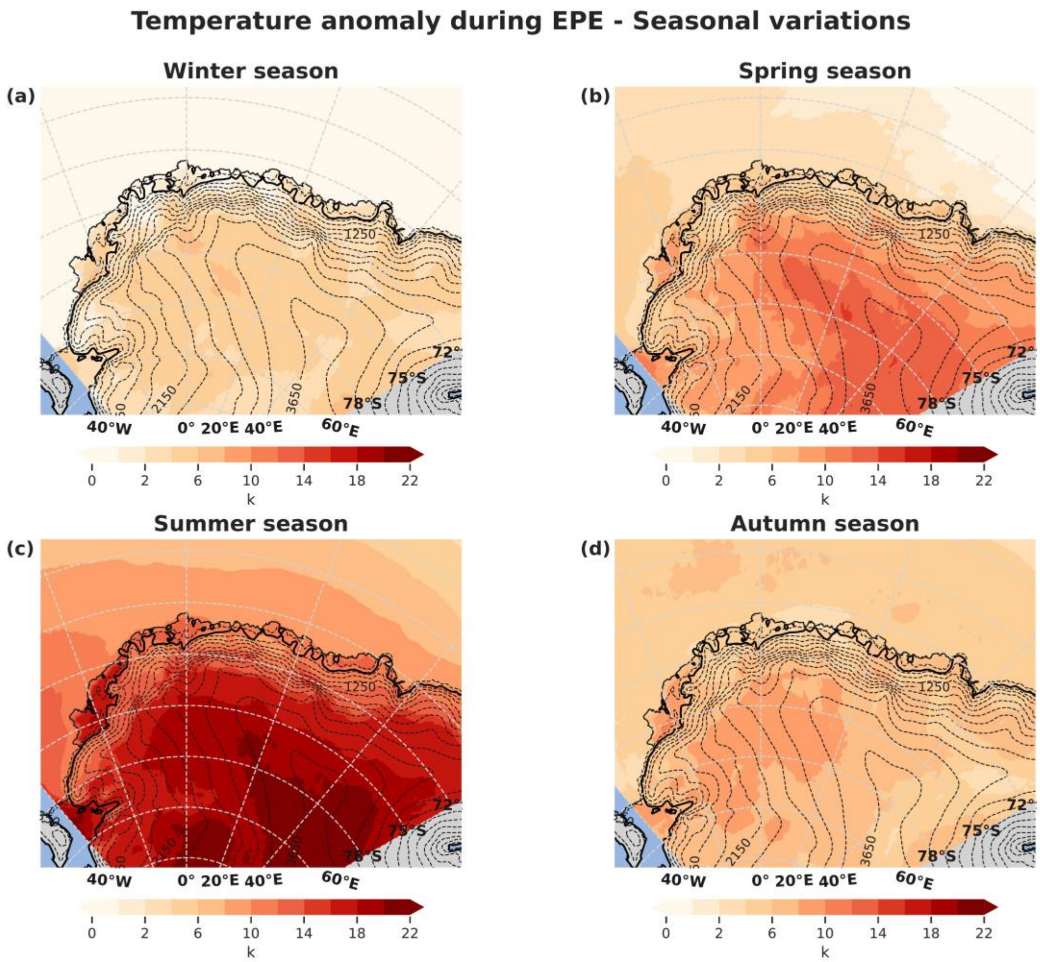

Figure 3.8: Spatial variation of temperature anomalies during each season. (a) Winter, (b) Spring, (c) Summer, (d) Autumn season. Elevation contours are overlayed (black dotted lines).

3.1.2 Temporal variability of EPEs and associated atmospheric conditions

3.1.2.1 Inter-annual variability of EPE occurrence over ice core sites

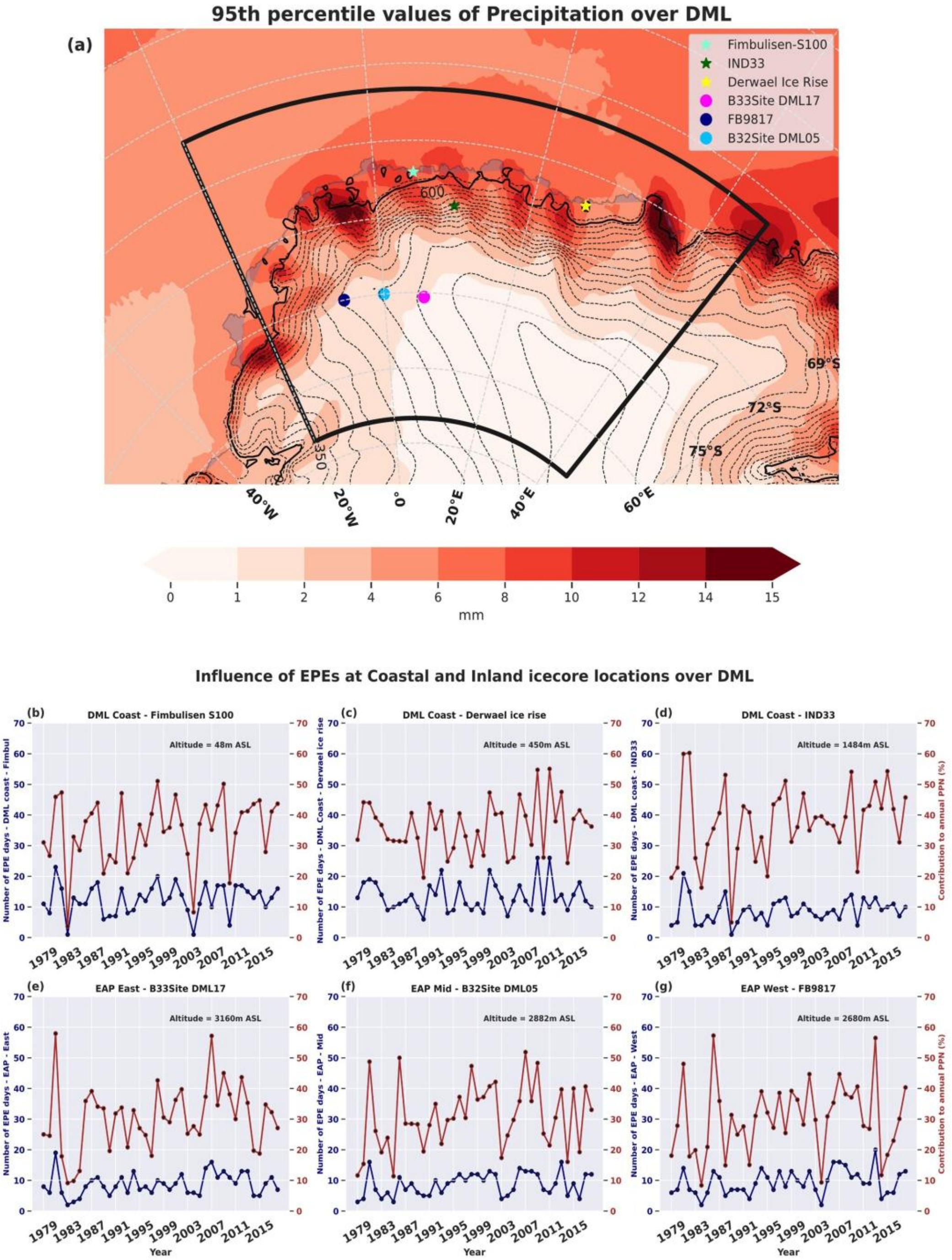

Figure 3.9: (a) Spatial variability of 95th percentile values with contours of elevation (dotted contours). The selected six locations for the temporal analysis of EPEs are also marked (a). Three locations from coastal (altitude < 2,000 m) ((b) Fimbulisen S100, (c) Derwael ice rise, (d) IND33) and three from inland (altitude > 2,000 m) ((e) B33Site DML17, (f) B32Site DML05, (g) FB9817).

The bold black line over the map shows the DML sector, temporal variability of the number of EPE days (blue line), and contribution to total annual precipitation (red line) for the period 1979–2018 from these locations.

The spatial variability of the EPE threshold value (95th percentile) is illustrated in Figure 3.9a. The coastal region shows large spatial variability in line with the complex orography of the region. The largest values are found along the ice shelves near 35°E and 5°W, and higher values are on the eastward-facing slopes. Precipitation events on the windward and leeward sides of small glacial valleys cause alternate higher and lower 95th percentile values in the coastal area. Inland, the 95th percentile value decreases and follows the orography in spatial distribution. The locations with frequent precipitation occurrences have a higher value in the 95th threshold on the eastward side of coastal orographic features. A comprehensive temporal analysis was conducted focusing on six ice core locations (Table 3.1). These sites were chosen based on their altitude, with three located in the coastal region (altitude < 2,000 m) and three in inland areas (altitude > 2,000 m), as indicated in Figure 3.9a.

The selected inland locations lie on the same latitude circle with a significant longitudinal separation. Due to frequent precipitation events in the coastal region, the EPE threshold values and the total number of EPE days decrease from the coast to inland. For all the locations during the study period, the autumn season experienced more EPEs than the winter or spring months. However, there is a high interannual variability in EPE occurrence between years. Figure 3.9 also shows the contribution of precipitation from EPEs to the annual total precipitation and the interannual variability of EPE days for the selected six ice-core locations. In regions close to the ocean (Figures 3.9b to 3.9d), the number of EPE days is relatively high (12–15 days year^{-1}), while the number of EPE days is smaller (8–10 days year^{-1}) in areas farther inland (Figures 3.9e to 3.9g). Coastal and inland locations have different numbers of EPE days, but on average, the EPEs account for 30%–40% of the total annual precipitation at each location. All areas have a substantial interannual variability in the number of EPE events, significantly influencing the annual total precipitation. The year 1981 had many EPEs at all selected sites, whereas 1983 and 2003 had fewer EPE days. In the following section, we examine the interannual and monthly variability of EPEs and the contributing factors.

Ice core location		Latitude, Longitude	Altitude (m)	95th threshold (mm)	Number of EPE days for the 1979-2018 period						AR contribution (%)
					Total	Mean (per year)	Autumn (MAM)-Total	Winter (JJA)-Total	Spring (SON) - Total	Summer (DJF)-Total	
Coastal	Fimbulisen S100	70.24S,4.8E	48	7.62	503	13	169	136	121	77	46.5%
	Derwael ice rise	−70.25S, 26.34E	450	5.825	539	14	215	148	107	69	41%
	IND33	71.51S,10.15E	1470	4.534	353	9	113	106	80	54	56%
Inland	B33Site DML17	75.17S,6.5E	3160	0.9958	350	9	122	78	75	75	42%
	B32Site DML05	75S,0.01W	2882	1.643	350	9	117	82	79	72	49.8%
	FB9817	75.0S, 6.5W	2680	1.363	376	10	136	84	89	67	44%

Table 3.1. *The six ice-core locations were selected for temporal analysis and altitude details as given by Thomas et al. (2017). The 95th percentile value, total number of annual EPE days, seasonal*

EPE days, and mean number of EPE days per year are given in each column. The percentage of EPEs associated with an atmospheric river (AR) is given in the rightmost column. This was calculated by comparing the EPE dates with AR landfall dates using the vIVT detection algorithm (Wille et al., 2021).

3.1.2.2 Meteorological factors controlling EPE occurrence

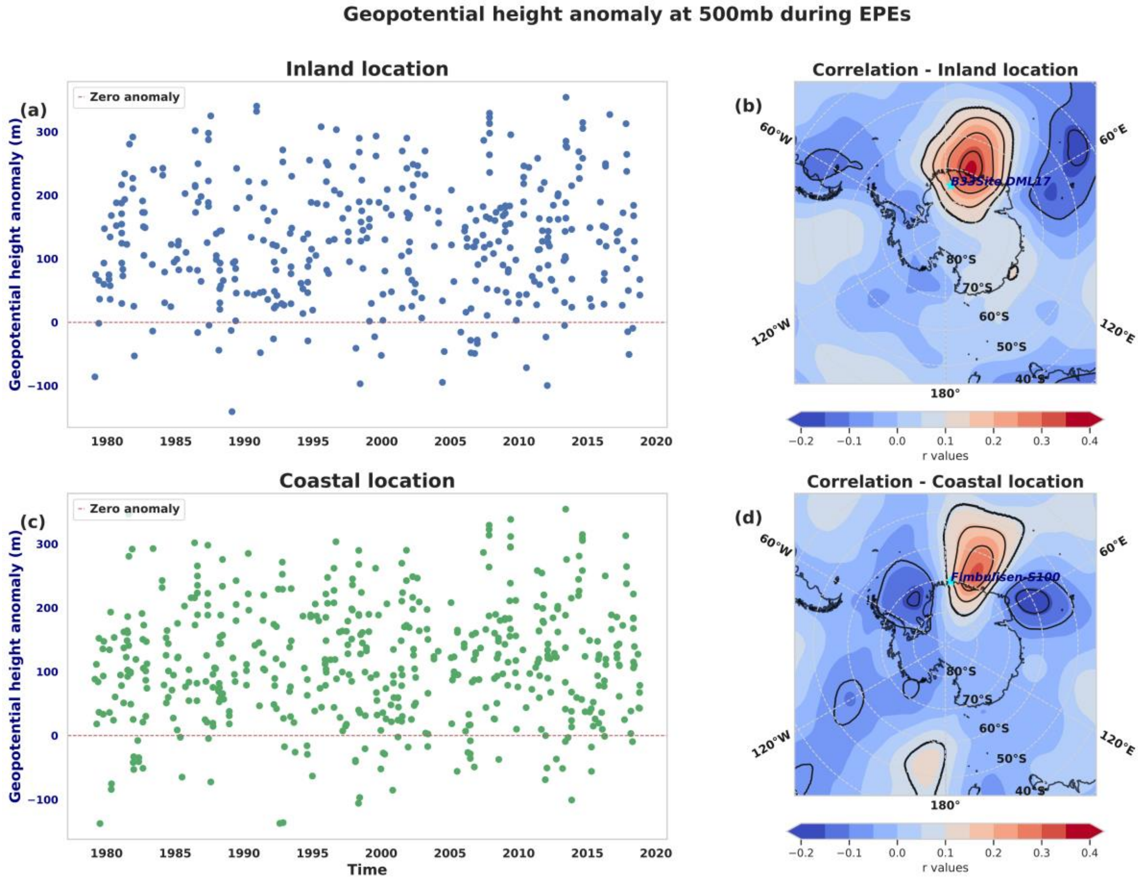

Figure 3.10: 500 hPa geopotential height anomaly during EPE days for the period 1979–2018 (a) for the inland location, (c) for the coastal location. The zero-geopotential height anomaly value is plotted as a separate line. (b) the correlation between EPE days precipitation and geopotential height anomalies during EPEs for the inland location, (d) same as (b) for the coastal location. Areas with significant correlation values are marked with bold lines.

The factors controlling the inter-annual variability of EPE days across the coastal and inland regions have been investigated using 500 hPa geopotential height anomalies over a rectangle box (0°E to 35°E and 60°S to 75°S) to the north-east of DML. Figure 3.10 shows the distribution of this during EPE dates for the selected inland (B33Site DML17 - Figure

3.10a) and coastal (Fimbulisen S100 - Figure 3.10c) locations for 1979–2018. Most EPE dates are linked to positive geopotential height anomalies to the northeast of the region, with a substantial proportion (91% inland and 89% coastal) of EPEs occurring during these atmospheric blocking episodes. The connection between EPEs and positive geopotential height anomaly underlines the importance of strong atmospheric blocking and EPE generation over the region

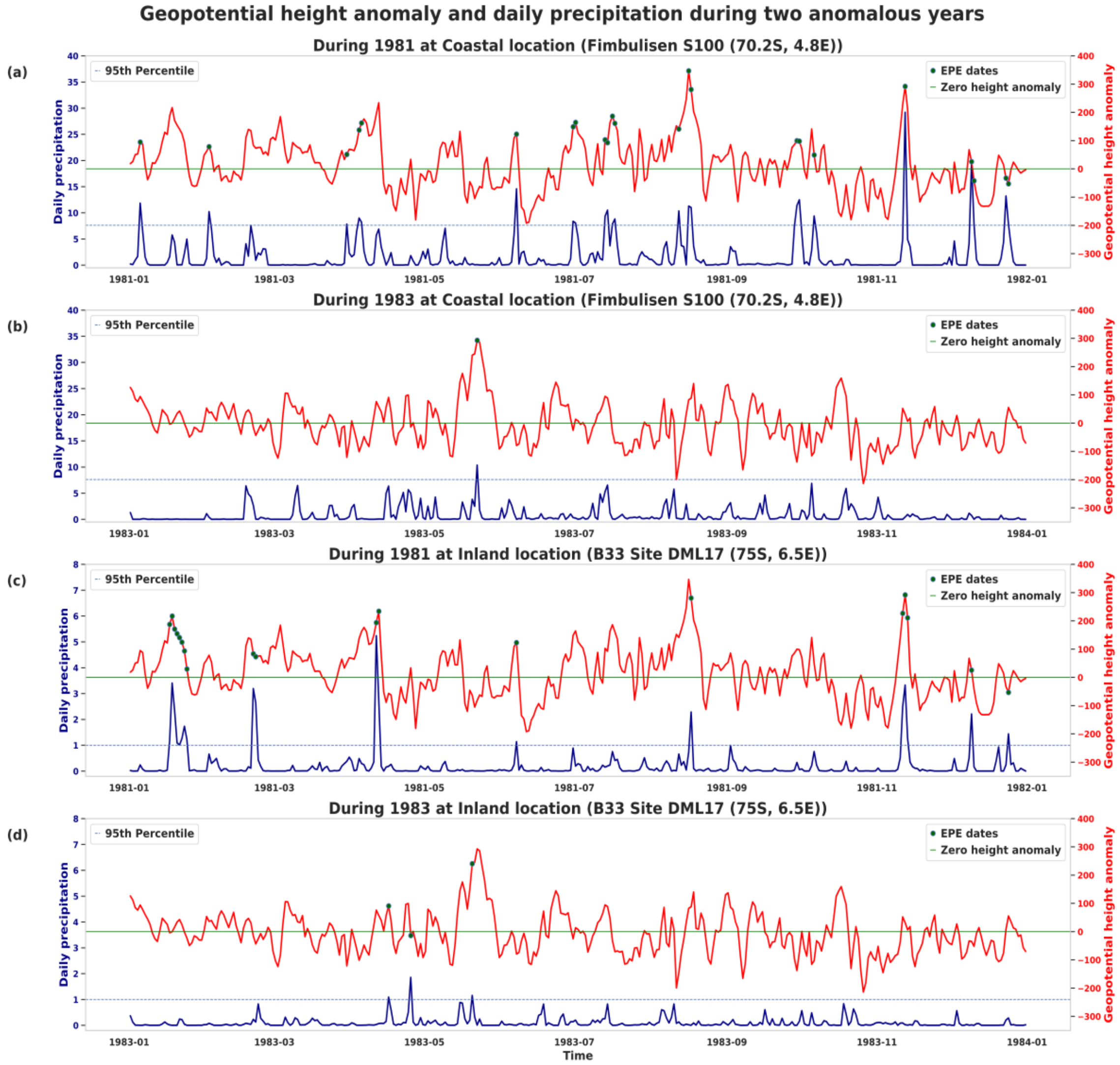

Figure 3.11: Variability of 500 hPa geopotential height anomaly over a rectangular box north DML (0°E to 35°E and 60°S to 75°S) (red line) and daily precipitation values (blue line) with green dots denoting the EPE days with daily precipitation greater than the 95th percentile value for a coastal location (Fimbulisen S100) and (a) for the year 1981 - a year with a greater number of EPEs, (b) 1983 – a year with few EPEs. (c,d) similar to (a,b) but for an inland location (B33Site DML17).

The blue dotted line indicates the EPE threshold value, and the green shows the zero-geopotential height anomaly line.

The spatial correlation of EPE-related precipitation and 500 hPa geopotential height anomalies also validate this relation (Figures 3.10b and 3.10d). The correlation analysis revealed a significant positive correlation (with an *r*-value of ~0.4) to the northeast of the region for both inland and coastal locations and a notably strong, significant correlation in inland areas (Figure 3.10b). This positive correlation between high precipitation amounts and higher geopotential height anomalies to the northeast emphasizes the pivotal role of atmospheric blocking in redirecting low-pressure systems to DML, leading to high precipitation.

To obtain detailed information about the interannual variability of EPE occurrences at the coastal (Fimbulisen S100) and inland (B33Site DML17) stations, we examined years with the largest (1981) and smallest (1983) number of EPE days within the 40-year period. Figure 3.11 shows the geopotential height anomalies and daily precipitation values for the coastal (Figures 3.11a and 3.11b) and inland (Figures 3.11c and 3.11d) stations. There were more EPE days at the coastal locations than inland, and these days of greatest precipitation were associated with intense blocking episodes. However, over the coastal locations, there were some EPE occurrences (9, 10, and 23, 24 December 1981) along with negative geopotential height anomalies, which indicates the presence of low-pressure systems and the landfall of cyclones. Inland areas, where long-lived strong blocking is necessary for moisture intrusion at high latitudes, show a substantially stronger relationship between atmospheric blocking and EPE days. For example, a significant blocking event in mid-January 1981 generated a week-long EPE event (17–24 January 1981) across the inland location. The year 1981 was marked by a high frequency of atmospheric blocking episodes, which resulted in a greater number of EPE days over both the coastal station (23 EPE days) and the inland (19 EPE days). However, due to fewer blocking occurrences, 1983 experienced a smaller number of EPE days and precipitation occurrences, with small precipitation amounts dominating that year. Since all blocking events north of DML did not produce significant precipitation, adequate moisture availability is crucial for EPE generation. Both the long-term (40-year period (Figure 3.10)) and short-term (1-year period (Figure 3.11)) analyses confirm the importance of high-pressure anomalies in the eastern part of the South Atlantic and associated moisture availability from marine sources in generating EPEs over DML. As discussed earlier, atmospheric blocking northeast of the area is crucial in controlling the interannual variability of EPEs, particularly in the inland zones.

Figure 3.12 shows the monthly variation of the total number of EPE days for each selected location over the 40-year study period. The number of EPE days varied significantly across months for the various sites. All sites show more EPE days from late autumn to early winter and at the end of the spring season. To investigate this further, the climatological (1979–2018) monthly MSLP values for each location were analyzed. The results show a weak relationship between the semi-annual oscillation of MSLP values and the frequency of EPE days. The surface pressure within the circumpolar trough is lower, and the trough is closer to the continent during equinoctial months. This seasonal change of MSLP around Antarctica has a crucial effect on the net transfer of air and moisture towards the continent (King & Turner, 1997). The position of the circumpolar trough, modulated by the temperature contrast between mid and high latitudes, leads to the semi-annual oscillation in pressure and wind values. The strength of this temperature difference is largest during the autumnal equinox, causing cyclonic activity to peak over the continent (van Loon, 1967). The frequency of EPE days during these months is increased by enhanced poleward transport of moist air to higher latitudes during this time. In late winter and summer, there is an equatorward shift of the circumpolar trough (King & Turner, 1997), which results in a decrease in the number of EPE days during those months over the Antarctic.

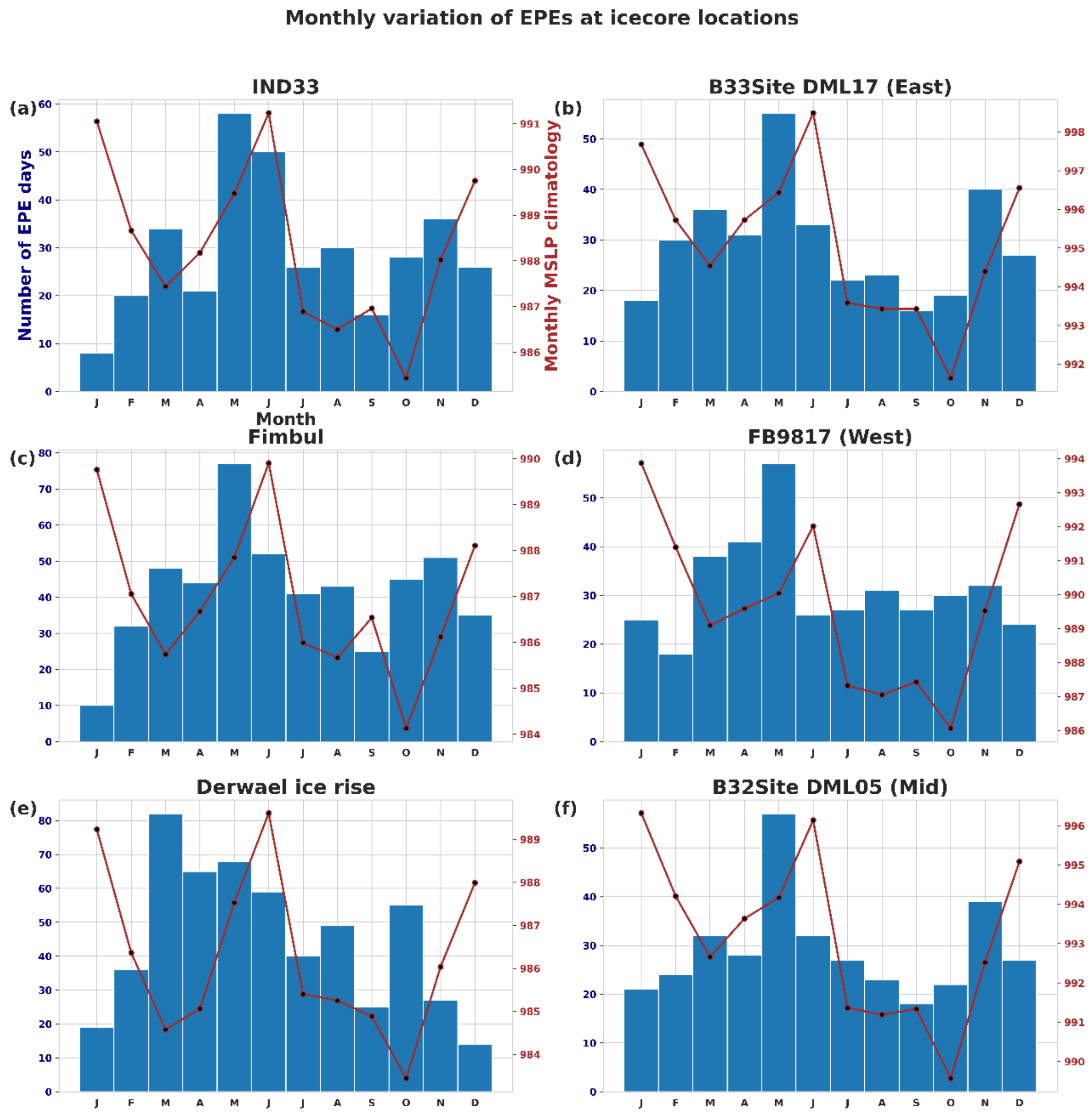

Figure 3.12: Histograms of the number of EPE days at six locations and monthly mean MSLP (red line) at these locations.

An examination of the duration of EPEs and their seasonal variations was conducted at one of the selected sites (IND33) and is illustrated in Figure 3.13. Out of 353 days marked by extreme precipitation, 240 distinct events have been identified. As with the findings of Turner et al., 2019, this location is predominantly characterized by short-duration EPEs (lasting 1–2 days), accounting for 63% of single-day events and 29% of 2-day events.

Longer-lasting events, spanning 3 and 4 days, are relatively rare, constituting just 7% and 0.1%, respectively. Regarding seasonality, the autumn season stands out with the largest number of EPE events at 32.78%, with single-day events being particularly dominant (making up 68% of EPEs during this month). Approximately 30.7% of EPEs occurred in the winter, with a significant proportion from 2-day events. The spring and summer seasons contribute 20.3% and 16.18% to the total EPE count, respectively, with a higher number of 3-day events during spring. Overall, it is observed that the autumn and winter months (March-August) have a higher frequency of EPEs at IND33. Although the number of EPEs has substantial interannual and seasonal variabilities, no significant relationship was found between indices of the major modes of climate variability, including the SAM and ENSO, and the number of EPE days over the region. This suggests that changes in ENSO and the SAM have a relatively small impact on the inter-annual variability of EPEs, with their occurrence primarily determined by regional atmospheric variability, such as the frequency of blocking episodes.

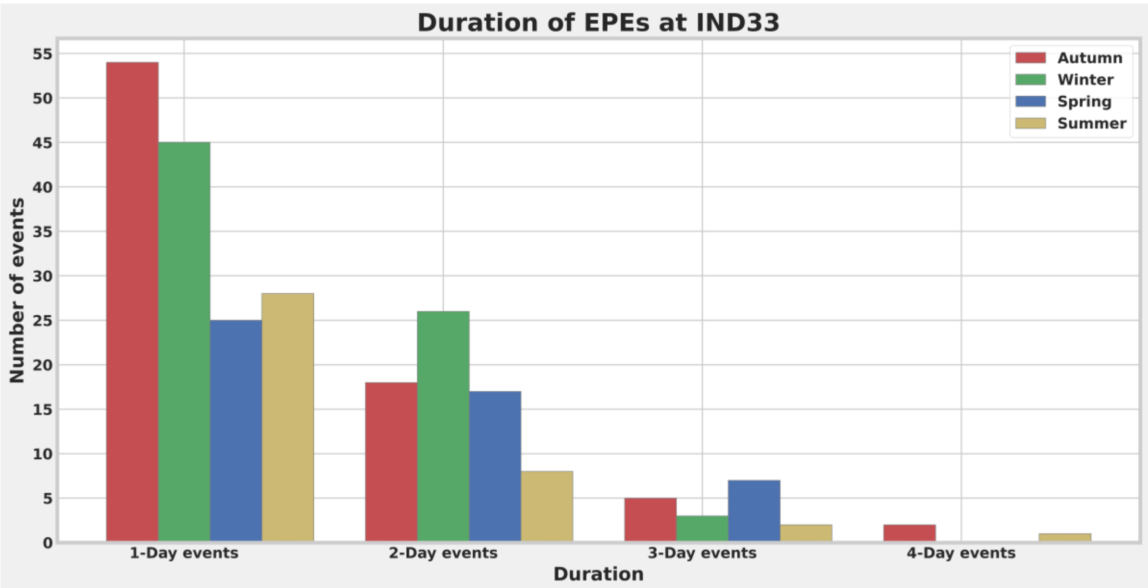

Figure 3.13: Duration of EPE days at IND33 and seasonal distributions.

3.1.3 Synoptic atmospheric conditions during EPEs

To identify the synoptic patterns that occur during EPEs, we used composite anomaly analysis and EOFs of atmospheric variables during EPE days. Figure 3.14 depicts composites of the MSLP anomaly during EPE episodes at three coastal locations (Figures 3.14 a, c, and e) and three interior sites (Figures 3.14 b, d, and f).

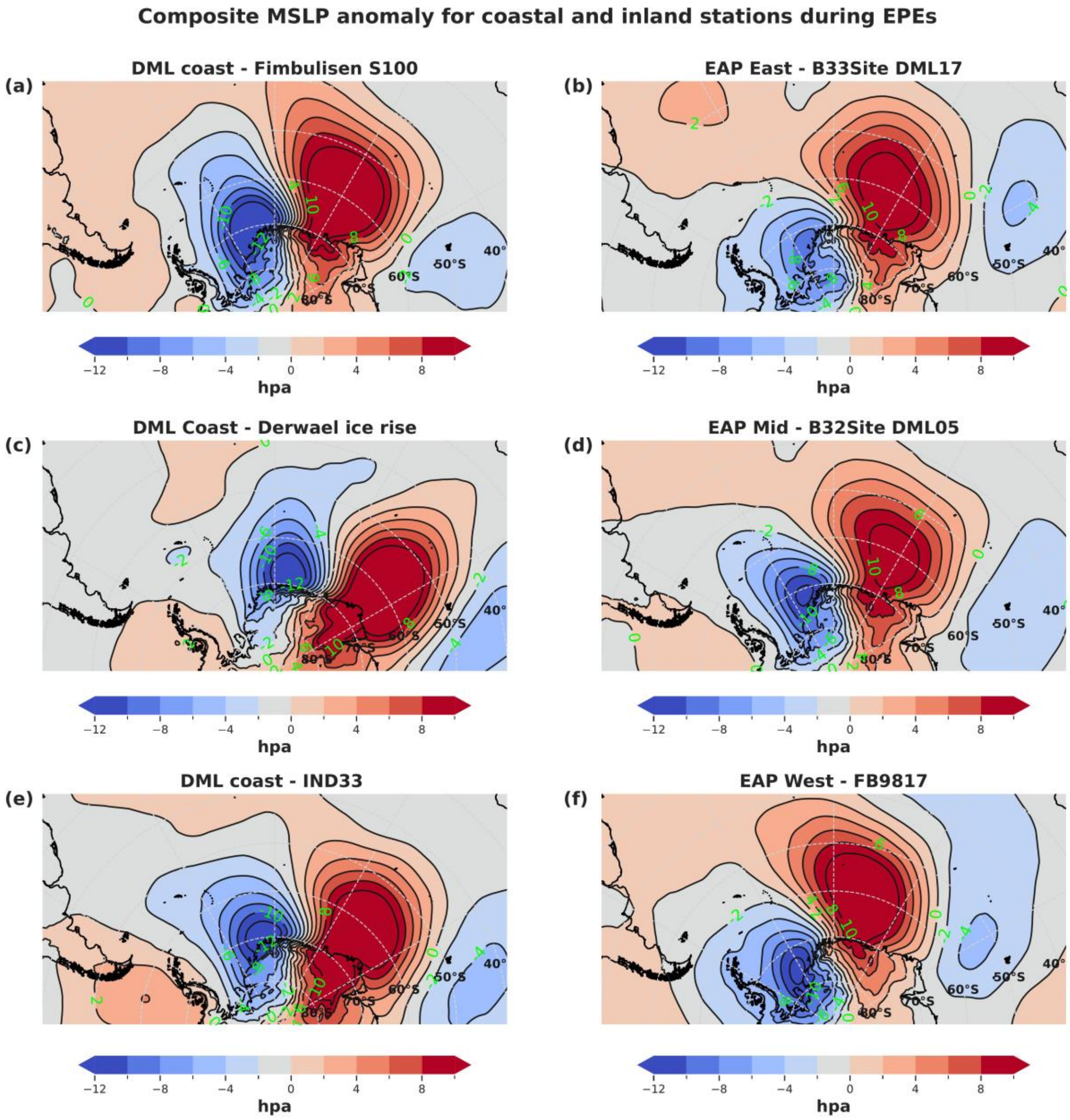

Figure 3.14: Composite MSLP anomalies during EPE days for six locations. The (a), (c), and (e) are for coastal locations, and the (b), (d), and (f) are for inland sites.

A dipole structure of negative (positive) anomalies to the west (east) is present for all locations, with a slight variation in orientation and strength between sites. This shows low pressure to the west and high pressure to the east, with significant atmospheric blocking over the region east of the location. This is the typical synoptic pattern during EPEs. The dipole structure is much more evident in coastal locations, where deep low-pressure systems are present to the west of the sites. However, atmospheric blocking to the east is a significant factor for inland locations rather than a few cyclonic intrusions to high latitudes. This dipole structure leads to anomalous northerly and north-easterly winds that carry moisture from mid-latitudes to DML.

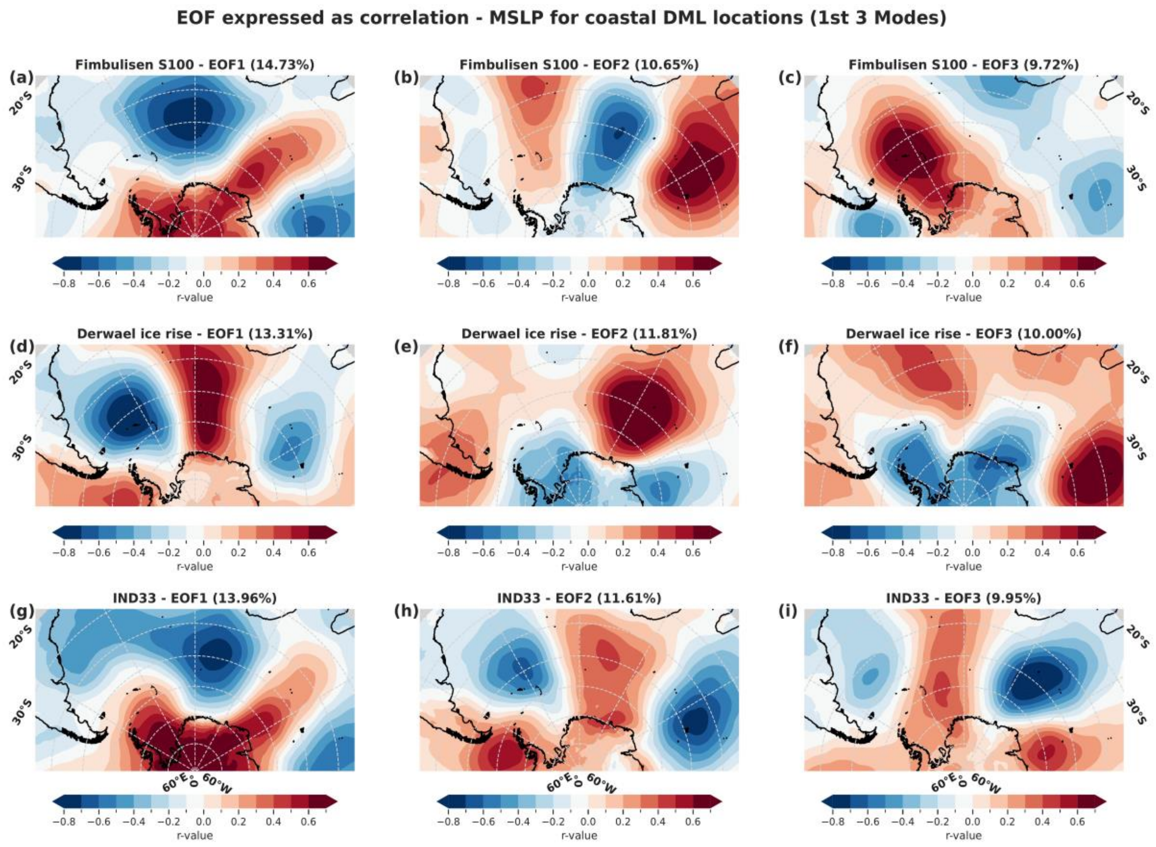

Figure 3.15: EOF modes of 500 hPa geopotential height during EPEs for coastal locations in each row. The top three EOF modes, which explain 40% of the variance, are given and expressed as the correlation between the principal component time series (PCs) and each data set in the input datasets. (a, b, c) – for Fimbulisen S100, (d, e, f) – Derwael ice rise, (g, h, i) – IND33

This chapter also used EOF analysis applied to 500 hPa geopotential height (20°S–90°S, 90°W–90°E) for the 100 largest EPEs over the region, which closely resembles the spatial patterns of the highest precipitation events. With each row showing data for a specific location, the spatial patterns of the first three modes explain more than 40% of the variance exhibited for the coastal area (Figure 3.15) and inland (Figure 3.16). The trough-ridge-trough pattern over the northern part of DML and the eastward shift in this pattern in mode 2 are both apparent in the first two modes, which account for 30% of the variance for the coastal regions. Mode 3 explains about 10% of the variance, describing the eastward-moving low-pressure systems over the South Atlantic. EPEs over the inland areas have a similar trough-ridge-trough pattern that is strongly correlated with the positive height anomalies north of DML. This highlights the significance of atmospheric blocking for EPE occurrences over the interior locations.

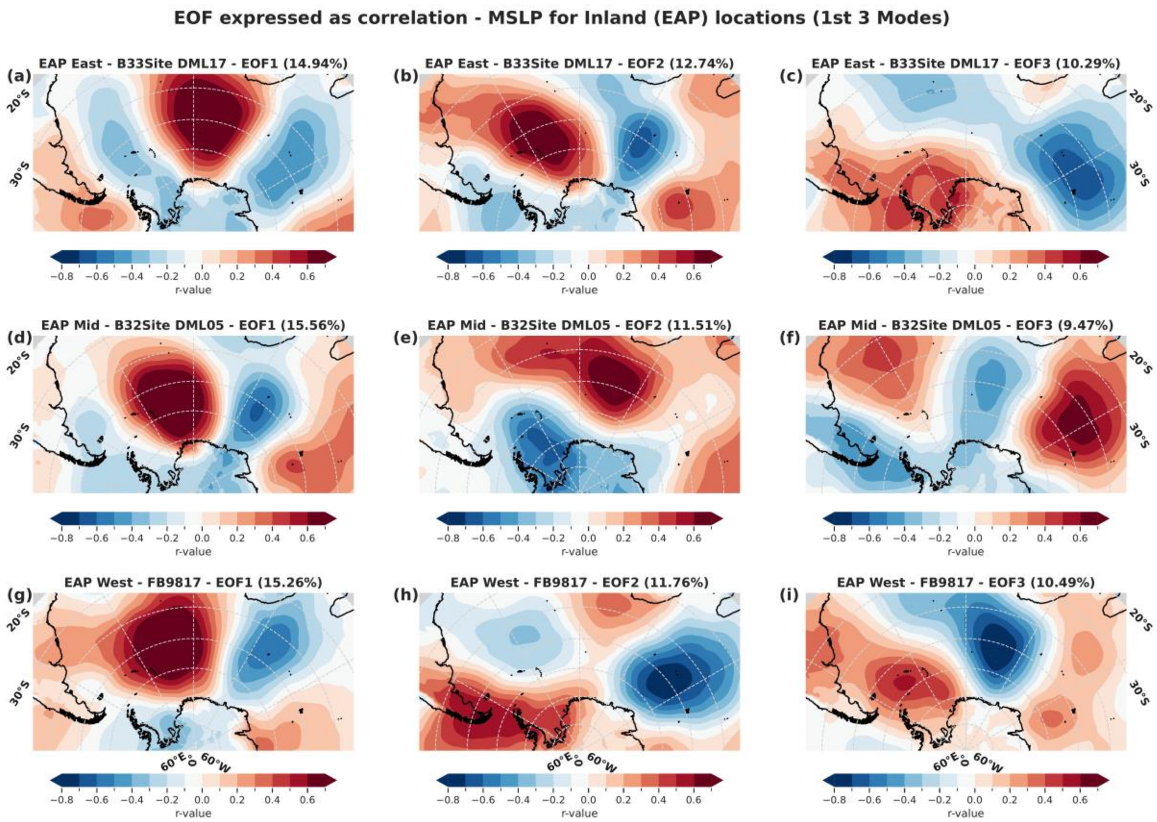

Figure 3.16: Same as Figure 3.15, but for inland locations. (a, b, c) – for B33 Site DML17, (d, e, f) – B32Site DML05, (g, h, i) – FB9817

3.1.4 Trends in the number of EPEs

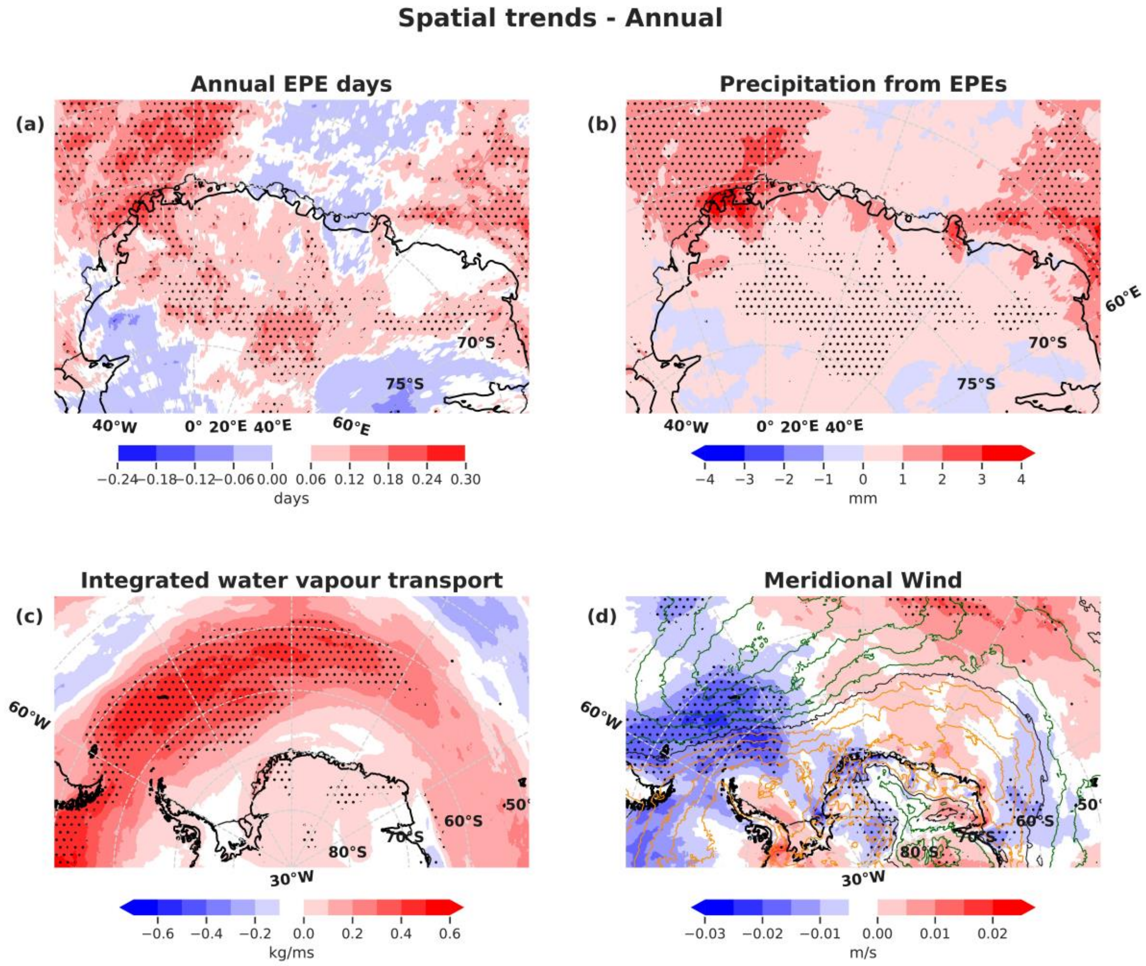

Figure 3.17: Annual trends for the period 1979–2018 in (a) the number of EPE days, (b) the amount of precipitation from EPEs, (c) integrated water vapor transport, and (d) the meridional wind component. The trend in MSLP values is shown by the contour lines in (d), where the green line shows a positive trend, and the orange lines show a negative trend. The black line indicates no trend. Dots denote locations with statistically significant trends (p < 0.05).

The spatial trends in the annual total of EPE days and related variables are displayed in Figure 3.17. With a magnitude of +0.25 EPE days year^{-1}, there is a statistically significant increasing trend ($p < 0.05$) in the number of EPE days to the west of the Greenwich meridian (10°W–3°E), which extends toward the interior around 75–80°S (Figure 3.17a). In these regions, there is also a significant positive trend in precipitation from EPEs, with a slope of 1–2 mm year^{-1} (Figure 3.17b). The trends in IVT, meridional wind, and MSLP over the Atlantic sector of the Southern Ocean were analyzed to explain the trends in EPEs (Figures 3.17c and 3.17d). The results demonstrate a significant ($p < 0.05$) positive trend in IVT values (0.6 kg m^{-1} s^{-1} per year) over the South Atlantic (over 60°W–20°E), the central moisture transport zone for EPEs towards DML. The meridional wind had a significant negative trend (-0.03 m s^{-1} $year^{-1}$), indicating that its more northerly winds towards DML, particularly over the area of 50°W–5°W. This meridional wind zone is closely linked to a north-south-oriented dipole-like trend in MSLP values (depicted by the overlaid contours in Figure 3.17d) within the South Atlantic, north of DML. This dipole pattern, characterized by a high-pressure and low-pressure pattern, contributes towards the inflow of favorable north-westerly winds, which are essential for maritime moisture intrusions and EPEs in the northwestern sector of DML. Altogether, the significant trends in water vapor transport and meridional winds led to an increased moisture convergence and an increase in high precipitating days. This study also found that the increasing trends in the thermodynamic (IVT) and dynamic (meridional winds) contributions were essential in the positive trend of EPEs. The time series analysis at the IND33 location shows a significant positive trend ($p < 0.05$) in annual precipitation from EPEs but no significant increase in the number of EPE days (Figure 3.18). This suggests that there has been an increase in the magnitude of extreme precipitation events in recent decades.

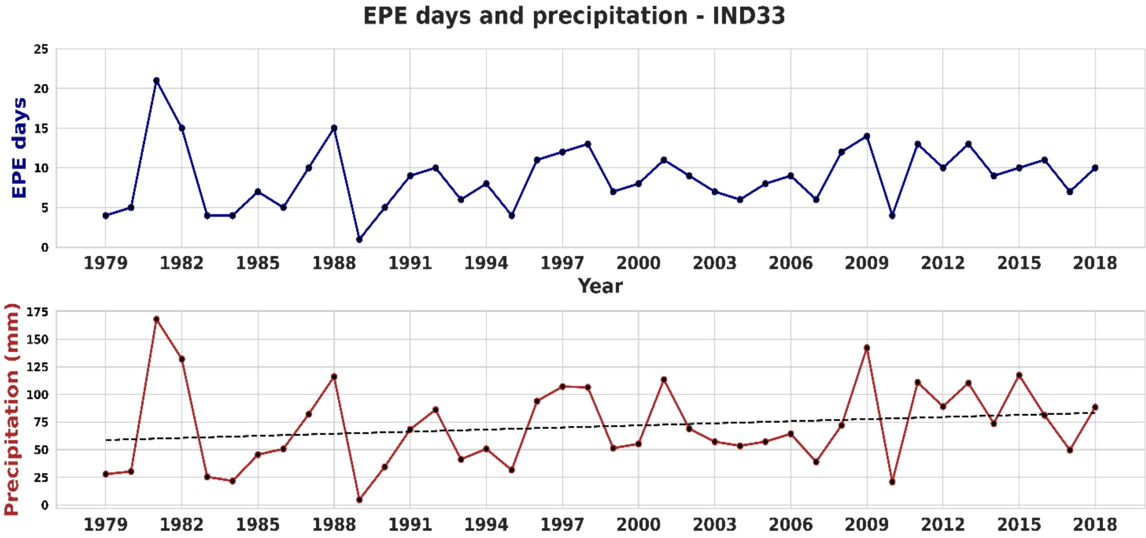

Figure 3.18: Variability in the annual total of EPE days (blue) and precipitation from these events (red) at IND33. The time series with a statistically significant trend is shown with a dotted trend line

3.1.5 The drivers of EPEs and contribution from atmospheric rivers

The synoptic drivers and moisture transport pathways are identified to gain a better understanding of the mechanisms behind EPEs. Welker et al. (2014) demonstrated that moisture transport (IVT) can be used as a proxy for high precipitation events over coastal and interior DML. With the presence of a synoptic dipole pattern of cyclones in the Weddell Sea and mid-tropospheric ridge to the east of the location (Section 3.1.3), the long-narrow, strong moisture transport through the eastern flank of these low-pressure systems is identified as the major synoptic patterns during EPEs. The occurrence of blocking high-pressure systems during EPE days will strengthen the vertically integrated moisture transport (IVT) to DML (Welker et al., 2014). As per the vIVT detection technique (Wille et al., 2021), most moisture transport pathways during these individual EPEs are identified as atmospheric rivers (AR). Using the AR landfall dates at the six different ice core locations for both coastal and inland areas, we quantified the percentage of ARs causing EPEs (rightmost column, Table 3.1). Around 40%–50% of EPEs are linked to the landfall of ARs, with the largest contribution occurring at IND33 (56%) among coastal sites and

B32Site DML05 (50%) among inland areas. The horizontal orientation of this dipole structure creates spatial variability in the AR landfall and generates EPE episodes. An average of 45% of EPE days were associated with AR occurrences in the interior locations with the strong support of a high-pressure ridge to the north of the locations. In addition, the moisture flow patterns of non-AR events also originate from low latitudes as long bands of moisture flow far north of the location. But, these EPE occurrences do not qualify as ARs because the moisture flows that occurred did not meet the length-width and moisture content threshold criteria in the AR detection techniques. Also, some AR landfall dates with high moisture content do not lead to EPEs in DML. Gehring et al. (2022) illustrated that even with strong AR moisture transport, limited precipitation might occur if the flow direction is unfavorable in relation to local orography. Low-level blocking winds can enhance precipitation during AR occurrences by supporting the upward vertical motion of poleward moisture intrusions along the complex orography over the DML region (Baiman et al., 2023; Bromwich, 1988). This study also used the technique of self-organizing maps (SOM) (Chapter 2) that uses IVT during EPE events from a coastal location (IND33) to demonstrate the diversity in moisture transport pathways during EPE occurrences. Figure 3.19 displays the SOMs of the IVT in a 15-node array with the frequency of occurrence for each node. The node with a high frequency (node - N9, N10, N11, N14, N15) highlights the AR pattern, whereas the other nodes display moisture transport from a range of directions to the area. Most moisture flux patterns that originate in the Atlantic Ocean come from a region with peak moisture flux values between 30°S and 50°S (Figure 3.19). With the synoptic support of low pressure to the west and high pressure to the east of DML, the moisture flows to the region from various directions from the South Atlantic and leads to high-magnitude precipitation.

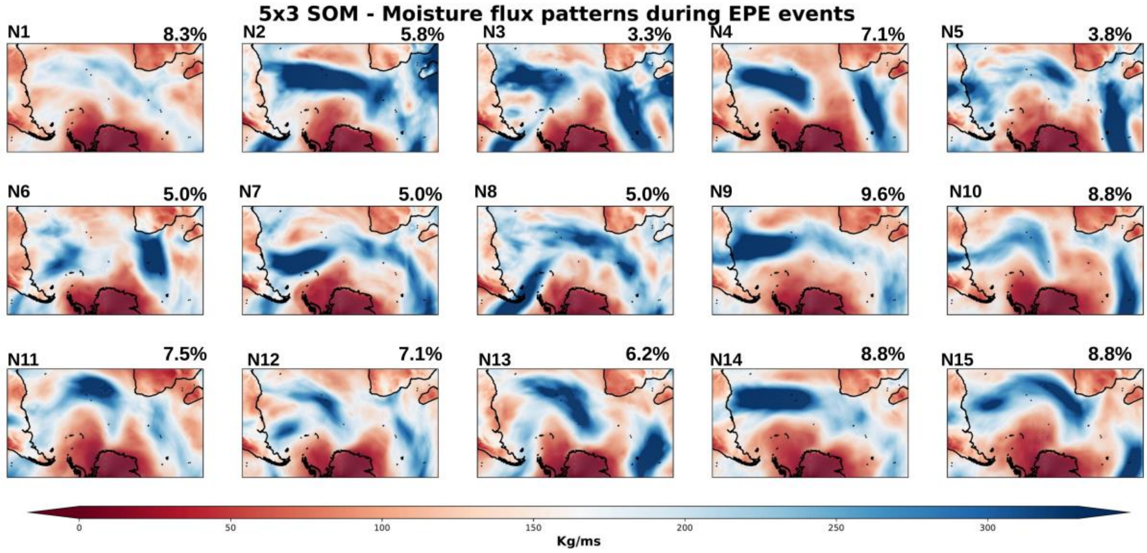

Figure 3.19: 15-node Self-Organizing Maps (SOMs) of moisture flux during EPEs at the coastal site IND33. The frequency of occurrence and node number are given in the top right and left corners, respectively.

3.2 Conclusions

This chapter dealt with the spatial and temporal variability of EPEs over DML using ERA5 reanalysis data for the period 1979–2018. The EPEs, constituting the top 5% of daily precipitation amounts, provided a significant proportion (35%–40%) of the annual total precipitation. The influence of EPEs is dominant along the steep gradient and complex orographic areas, which contribute 40%–45% of the annual total precipitation in just 10–15 days per year. Seasonally, autumn has spatially and temporally the largest number of EPE days. Along with the impact on annual precipitation total, EPEs influence surface meteorological variables such as surface wind and temperature. During EPEs, there are persistent and constant strong easterly to northerly winds, and the interaction between these winds and the region's orography has a crucial effect on the spatial distribution of EPE days. When EPEs make landfall, temperatures are anomalously high, significantly impacting inland regions. The synoptic patterns show that during most EPEs, there are low-pressure anomalies to the west and high-pressure anomalies to the east, with atmospheric blocking to the east of the location being especially important for inland regions. Eastward-moving cyclones and the trough-ridge-trough pattern are crucial in producing EPEs over the region.

The temporal variability in the number of EPE days is controlled by atmospheric flow regimes such as atmospheric blocking and changes in the circumpolar trough over the Southern Ocean. A detailed analysis of a few extreme years shows a strong relationship between atmospheric blocking and EPE occurrence, especially for inland regions. Over the region, notably central DML, there has been an increasing trend in EPE days and EPE-related precipitation. This resulted from kinetic and thermodynamic changes in the South Atlantic. The positive trend in IVT and northerly winds has been responsible for the increase in these high-magnitude precipitation events in recent decades, with a significant role in the landfall of strong ARs. By comparing the dates of AR landfall and EPE occurrences from six selected ice core sites spanning the coastal and interior parts of DML, it was determined that 40%–50% of EPEs are related to ARs. EPEs have various moisture transport pathways associated with a dipole structure of low-pressure systems to the west and high pressure to the east. Increasing trends in EPEs and ARs over DML, which are associated with the changes in atmospheric moisture content and winds, have a potential impact on the stability of ice shelves over this region in the future.

Chapter 4

A high-resolution case study of an extreme precipitation event over Dronning Maud Land

Introduction

Extreme precipitation events (EPEs) contribute a large portion (>40%) of annual snowfall in just a few days across much of the Antarctic continent (Chapter 3; Noone et al., 1999; Turner et al., 2019). These EPEs are one of the major controlling factors of sudden changes in surface mass balance and surface height over most of the West (Adusumilli et al., 2021) and East (Boening et al., 2012; Gorodetskaya et al., 2014; Lenaerts et al., 2013) Antarctic coastal regions. Detailed case studies are essential for better understanding the extreme events and the underlying processes driving them. This chapter analyses a heavy precipitation event in the Austral Autumn on November 8 and 9, 2015. The event was one of the most significant precipitation events for the 1979-2021 period at the ice core site IND33 (71.51°S, 10.15°E) (Ejaz et al., 2021) in coastal Dronning Maud Land (DML - 20°W to 45°E). Significantly, this event was associated with an intense atmospheric river (AR) event, which was within the top 1% of ARs identified through the atmospheric river tracking technique developed by Wille et al. (2021). The primary goals of this chapter are to determine the extreme conditions during this event, follow the evolution of the synoptic-scale environment, and elucidate the pathways of intense moisture transport. This investigation employed a combination of surface in-situ data and remote sensing observations, reanalysis fields, and satellite imagery. Additionally, using a high-resolution regional atmospheric model (Polar WRF) validated for coastal DML (Chapter 2), the role of the coastal orography on the distribution of precipitation during this event was explored.

4.1 Details of the case study

4.1.1 Spatial and temporal precipitation characteristics

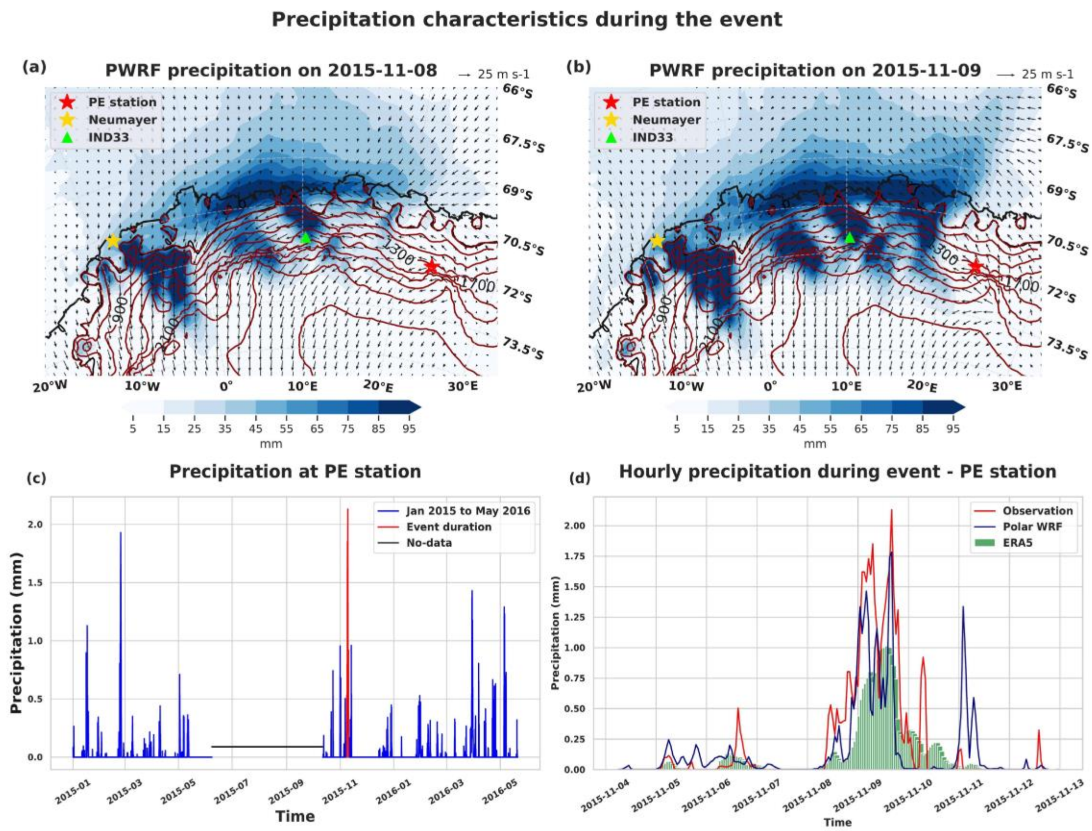

Figure 4.1: (a) Spatial distribution of daily precipitation (shading (mm)) from the Polar WRF model domain with 9 km resolution for 8 November 2015. The orography (red lines (m)) of DML and wind vectors are overlaid. Also, the ice core location (IND33) and locations of Neumayer and Princess Elisabeth (PE) stations are marked. (b) same as (a) but for 9 November 2015. (c) Hourly precipitation reported at the PE station derived from MRR measurements from January 2015 to May 2016 (blue lines, (mm/hr)). A red line marks the precipitation for the event duration, and the data gap area is marked with a black horizontal line. (d) Hourly precipitation (green bar, (mm)) derived from ERA5 for the event days and hourly precipitation observed at PE station (red line, (mm/hr)) and simulated using the Polar WRF model (blue line, (mm))., MRR: Metek's Micro Rain Radar.

The spatial and temporal characteristics of the EPE over DML on 8 and 9 November 2015 are depicted in Figure 4.1. The figure shows the spatial distribution of daily accumulated precipitation simulated by the Polar WRF model on 8 (Figure 4.1a) and 9 November (Figure 4.1b) within the model's 9 km resolution domain. The elevation contours (red lines) highlight the complex orographic structure of the coastal region, with closed contour lines indicating areas of significant orographic gradients over short distances. This region has a complex topography, such as ice rises, steep mountain slopes, and nunataks (Rotschky et al., 2007, Chapter 2). The spatial precipitation pattern and elevation contours illustrate that precipitation fell predominantly in the coastal and escarpment regions near steep gradient areas. The highest precipitation values were concentrated on the eastern slopes of the orographic features in the near-coastal region. Polar WRF simulated the effects of coastal orography in controlling the spatial distribution of precipitation. The event had a broad spatial coverage spanning 5°W to 20°E and was characterized by significant spatial variability with several regional precipitation maxima and minima along the coastal zone. Spatially, there were three (on 8 November) to four (on 9 November) peaks of high precipitation over the region associated with the undulations in the orography of the area. On 9 November (Figure 4.1b), there was an eastward shift in the spatial pattern due to the eastward propagation of the cyclonic system and moisture transport conducive to a heavy precipitation event. According to ERA5, 8 November 2015, was the day with the highest precipitation at IND33 (71.51°S, 10.15°E, Figure 1) for 1979-2022, with a daily total of nearly 32 mm (Figure 4.2a). This event contributed approximately 22% of the 2015 total precipitation, based on the 2-day (8 and 9 November) accumulated value. This precipitation event at IND33 started at 18 UTC on November 7 and ended at 12 UTC on 9 November, 2015, and the temporal distribution shows that there were two peaks of high precipitation (Figure 4.2b).

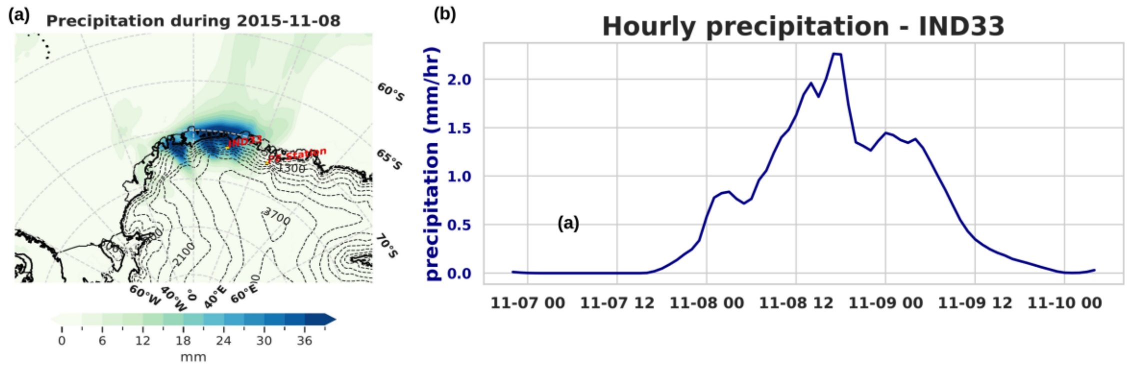

Figure 4.2: (a) Spatial representation of precipitation on ERA5 model on 8 November 2015. The dotted line indicates the elevation of the region based on the ERA5 fields. The locations of IND33 and PE station are also marked. (b) The precipitation time series for the event at IND33 from ERA5 data (mm/hr).

For the detailed temporal analysis of the event, we utilized observed variables from Princess Elisabeth (PE) station situated slightly inland in DML (Figure 4.1a). The hourly precipitation rate from the Micro Rain Radar (MRR) at the station exhibited episodic and highly variable precipitation values between January 2015 and May 2016. The highest precipitation rate occurred on 9 November 2015, marking the peak within this period (Figure 4.1c). The temporal precipitation pattern during the event was analyzed using hourly precipitation rates and compared with the Polar WRF outputs and ERA5 values from the nearest grid point to the observation point (Figure 4.1d). The PE station is located east of IND33, where the snowfall commenced at 9 UTC on 8 November and finished at 8 UTC on 10 November 2015. Two peaks in the temporal distribution of precipitation were observed at 6 UTC on 9 November and 15 UTC on 10 November 2015, with precipitation rates reaching up to 2 mm hr^{-1} (Figure 4.1d). These peaks were concurrent with the frontal bands approaching these locations, and the Polar WRF model successfully simulated this temporal variability with a good representation of the peaks. There was a slight overestimation of precipitation values in the model on 11 November. However, ERA5 underestimated precipitation values at the location of the PE station, and the temporal peaks during the event were not well represented (Figure 4.1d).

To understand the representation of this event in different reanalysis products (JRA55, MERRA2, CFSv2, ERA5), we analyzed their outputs on 8 November 2015 (Figure 4.3). All the reanalyses captured the broad-scale intense precipitation amounts and spatial distribution on 8 November 2015, particularly the dominant three-band structure. However, there are differences in the precipitation magnitude across these models, likely due to variations in model resolution and the representation of orography in the complex coastal terrain (Gehring et al., 2022; Mottram et al., 2021).

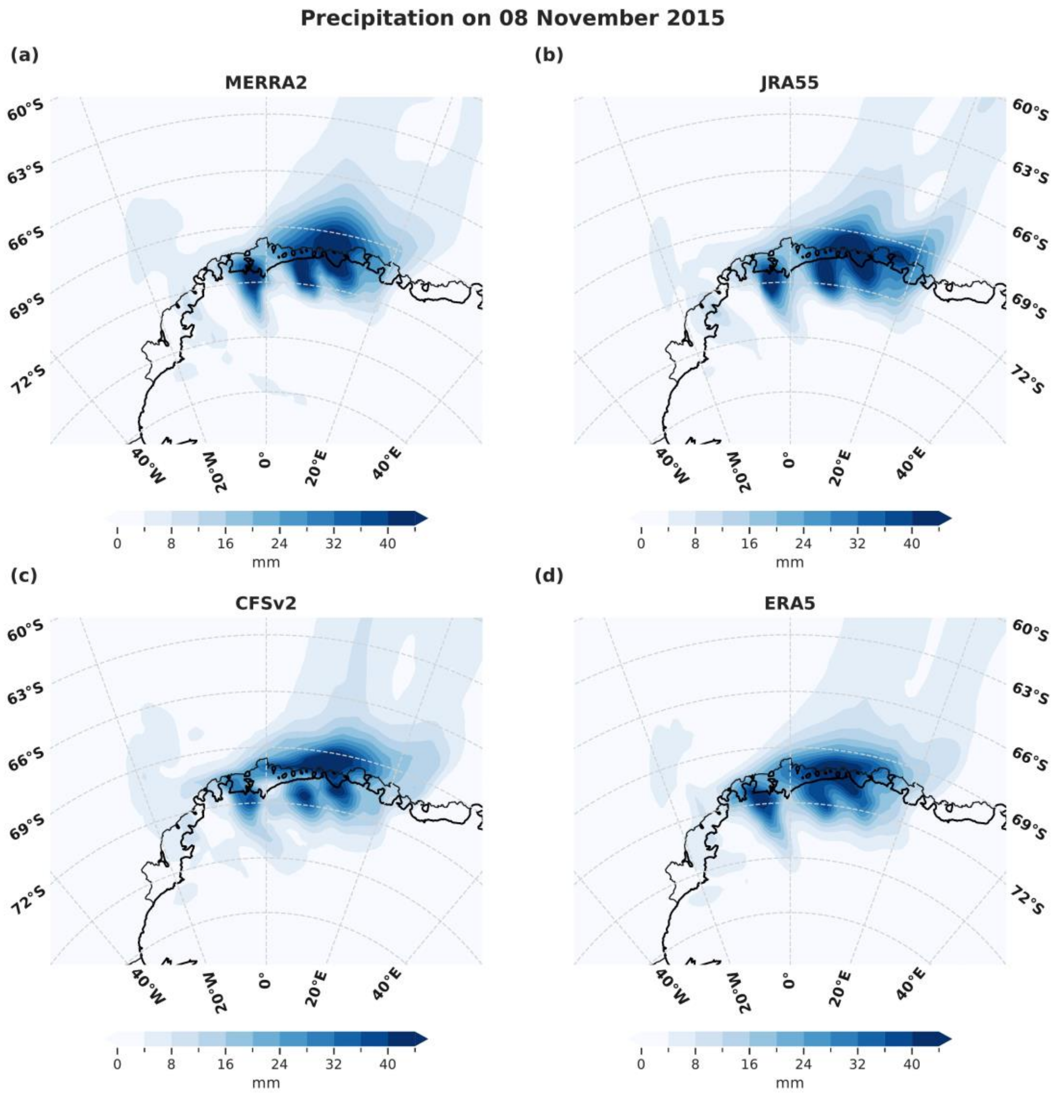

Figure 4.3: The spatial distribution of precipitation on 8 November 2015, from different reanalysis models. (a) MERRA2 (0.5° × 0.625°), (b) JRA55 (1.25° × 1.25°), (c) CFSv2 (0.5° × 0.5°), (d) ERA5 (0.25° × 0.25°).

The dynamically downscaled high-resolution regional model, Polar WRF, demonstrated a clear improvement in both spatial and temporal precipitation distribution over the coastal region compared to the reanalyses (Figure 4.1d), highlighting the importance of accurately representing orographic features in these models. The high-resolution simulation using the Polar WRF model showed higher precipitation values than the reanalyses, attributed to its better ability to capture the interactions between steep orographic structures and advected air masses during the event. While reanalysis models are adequate for capturing large-scale interactions, they lack the resolution necessary to resolve highly localized processes in complex terrains like DML. High-resolution regional models, such as Polar WRF, are better suited for simulating snowfall events in these areas, as they can more accurately represent small-scale processes and interactions. The highly variable precipitation distribution, with banded structures, is also evident in climatological precipitation maps over this region (Figure 3.1, Chapter 3). Thus, the complex orography of the region plays a pivotal role in snowfall accumulation and wind-induced redistribution during these EPEs, and the frequency and precipitation distribution of these events can introduce biases in ice-core climate records, especially depending on the core-drilling locations.

4.1.2 Extreme conditions during the event

To understand the event's unique extreme character and its associated atmospheric dynamics, we employed an extreme value analysis on different atmospheric variables during the event. These variables were mean sea level pressure (MSLP), 500 hPa geopotential height, 10 m wind speed, and integrated water vapor transport (IVT). Extreme value points are shown in Figure 4.4 to highlight the unique nature of the event. In Figure

4.4a, 500 hPa geopotential height values on 8 November exceeded the 95th and 99th percentiles, particularly to the east of DML. This signifies an inland, high-pressure ridge of record strength during the event, which acted as a block for the deep cyclone's eastward progression.

Extreme MSLP values below the 5th and 1st percentiles (Figure 4.4b) indicate an intense low-pressure system west of the region, progressing south-eastward from the South Atlantic and making landfall on 8 November 2015. ERA5 had a very low daily mean MSLP of ~950 hPa at the center of this low-pressure system. These extreme, free atmosphere and lower troposphere conditions initiated strong northerly winds and intense moisture transport towards Antarctica (Figure 4.4c, 4.4d). The combination of a low-pressure system to the west and a blocking high-pressure ridge to the east was identified in Chapter 3 as the major synoptic pattern during the EPEs over coastal Antarctica.

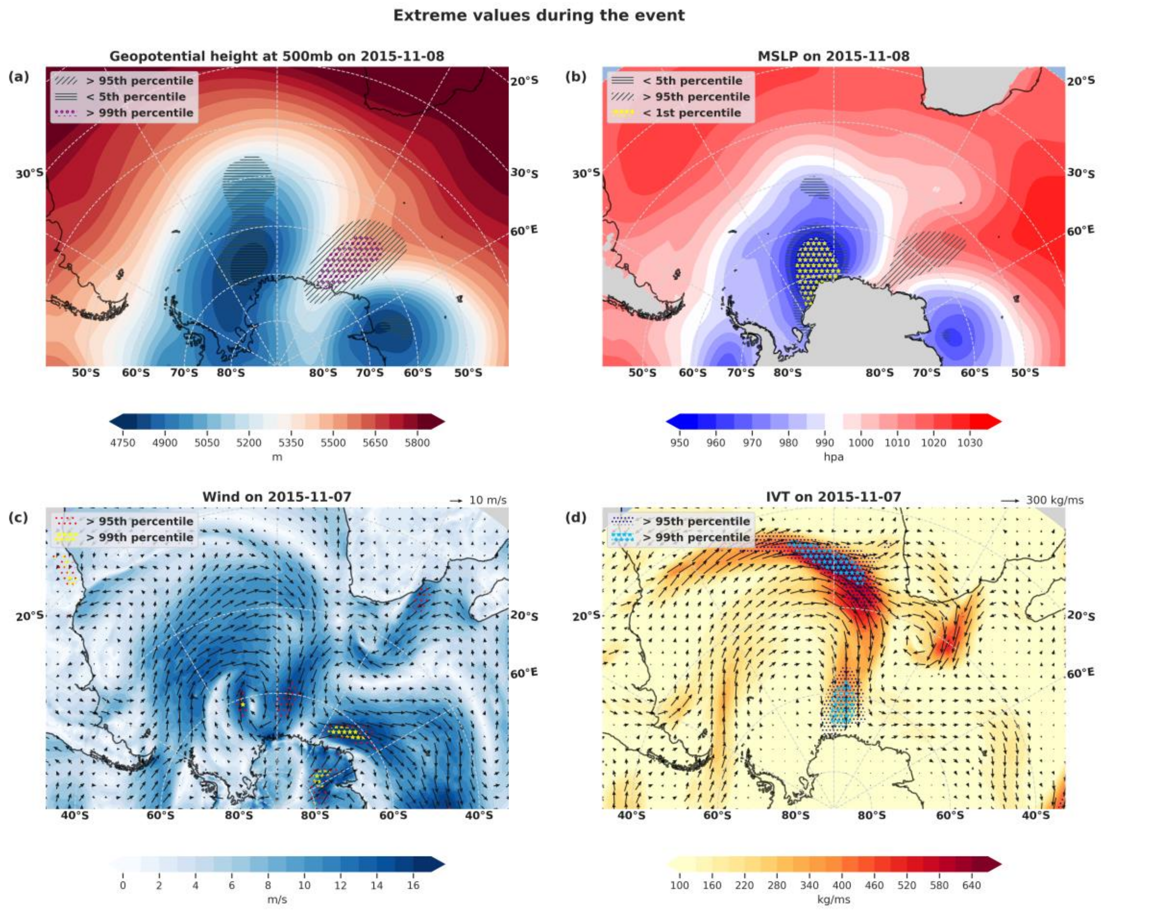

Figure 4.4: Synoptic conditions during the precipitation event in ERA5 and the regions with extreme values found using percentile criteria are denoted in the figure. (a) 500 hPa geopotential height, (b) mean sea level pressure (MSLP), (c) wind speed at 10 m, (d) integrated water vapor transport (IVT). The percentiles are calculated using daily data from ERA5 for 1979-2018. The MSLP values over the high-altitude regions are masked.

A convergent wind pattern was exhibited over the coastal region (15°E to 30°E), with the presence of katabatic winds from inland (Figure 4.4c), which led to the interaction of the warm, moist airmass, cold katabatic winds, and complex orography of the coastal region. These winds reached speeds of up to 15 m s^{-1}, which triggered blowing snow in the precipitation region. The influence of these strong winds and post-depositional effects can significantly mix and disperse the newly fallen snow, potentially affecting the annual signals recorded in ice cores. IVT values were large on the cyclone's eastern flank, and there were also high values over the South Atlantic, which was near 30°S and extended as an atmospheric river towards Antarctica (Figure 4.4d). One of the strongest AR events identified at IND33 occurred on 7 and 8 November 2015, with IVT values greater than the 99th percentile values of all AR occurrences at this location. The ARs at IND33 were found and tracked using the AR detection criteria of Wille et al. (2021). A detailed analysis of this AR is explained in the following section (section 4.2.5).

Extreme precipitation and temperature values during and following the landfall of an AR are shown in Figure 4.5. Most coastal areas exceeded the 95th percentile precipitation threshold and experienced snowfall extending inland on 9 November, concurrent with the intrusion of a blocking ridge. Simultaneously, 2 m temperatures displayed extreme values on the 9 and 10 November (Figure 4.5c, d), propagating inland after the event. As part of the analysis, atmospheric thickness (1000-500 hPa) was examined throughout the event (Figure 4.6), which depicted the heat content of the lower troposphere.

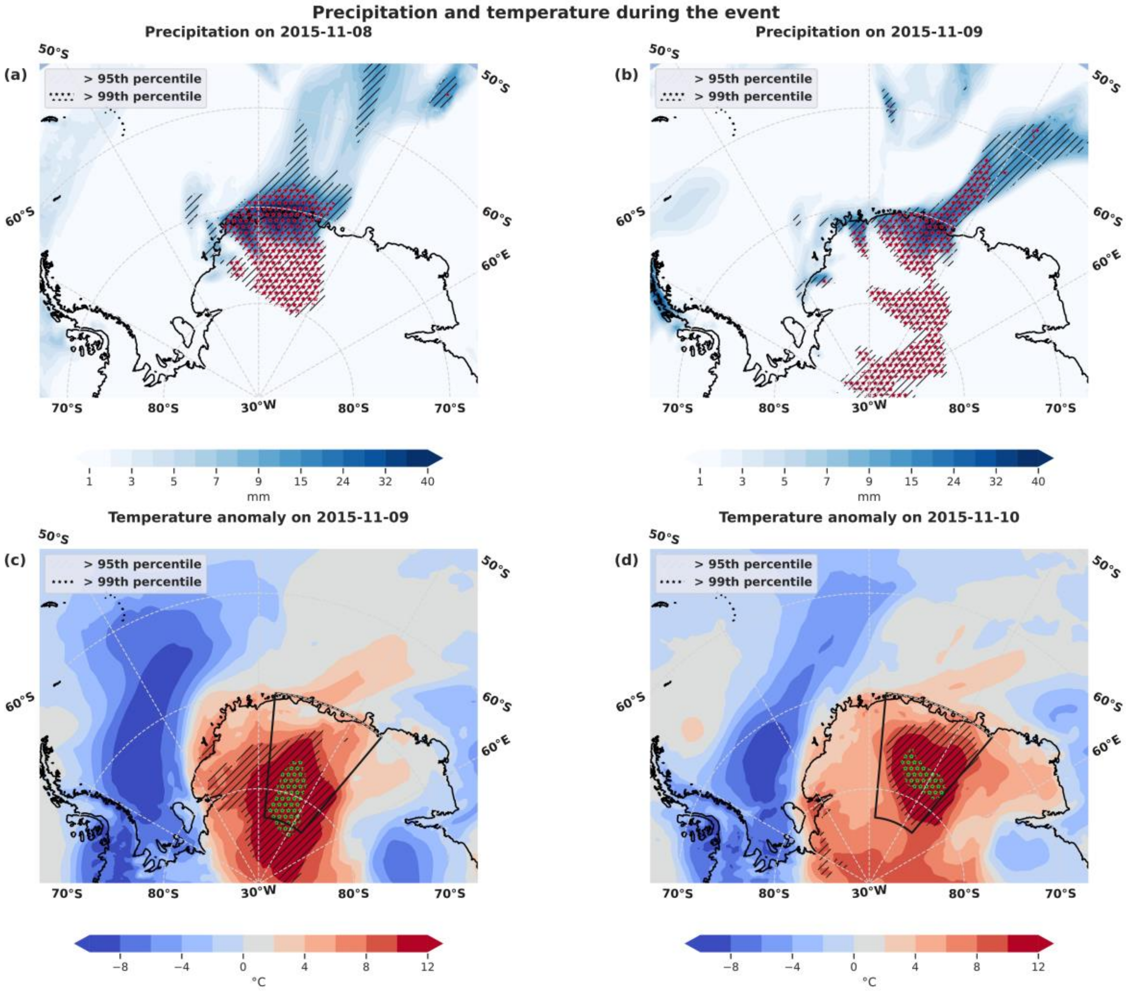

Figure 4.5: The locations of the extreme values found using percentile criteria (a) precipitation values during 8 November, (b) precipitation values during 9 November 2015, (c) 2-m temperature anomaly values during 8 November, and (d) 2-m temperature anomalies during 9 November 2015. Daily anomaly values were calculated using data for the climatology period 1979-2018. The box selected for temporal analysis of radiative and turbulent flux values is also marked in (c) and (d).

On 6 November, a northward extension of the trough region around 30°W indicated the movement of cold air from high to low latitudes, reflected in lower thickness values. The inland extension of high thickness values on 7 and 8 November demonstrated the advection of warm air towards the ice sheet, particularly over 0-30°E, resulting in higher temperatures.

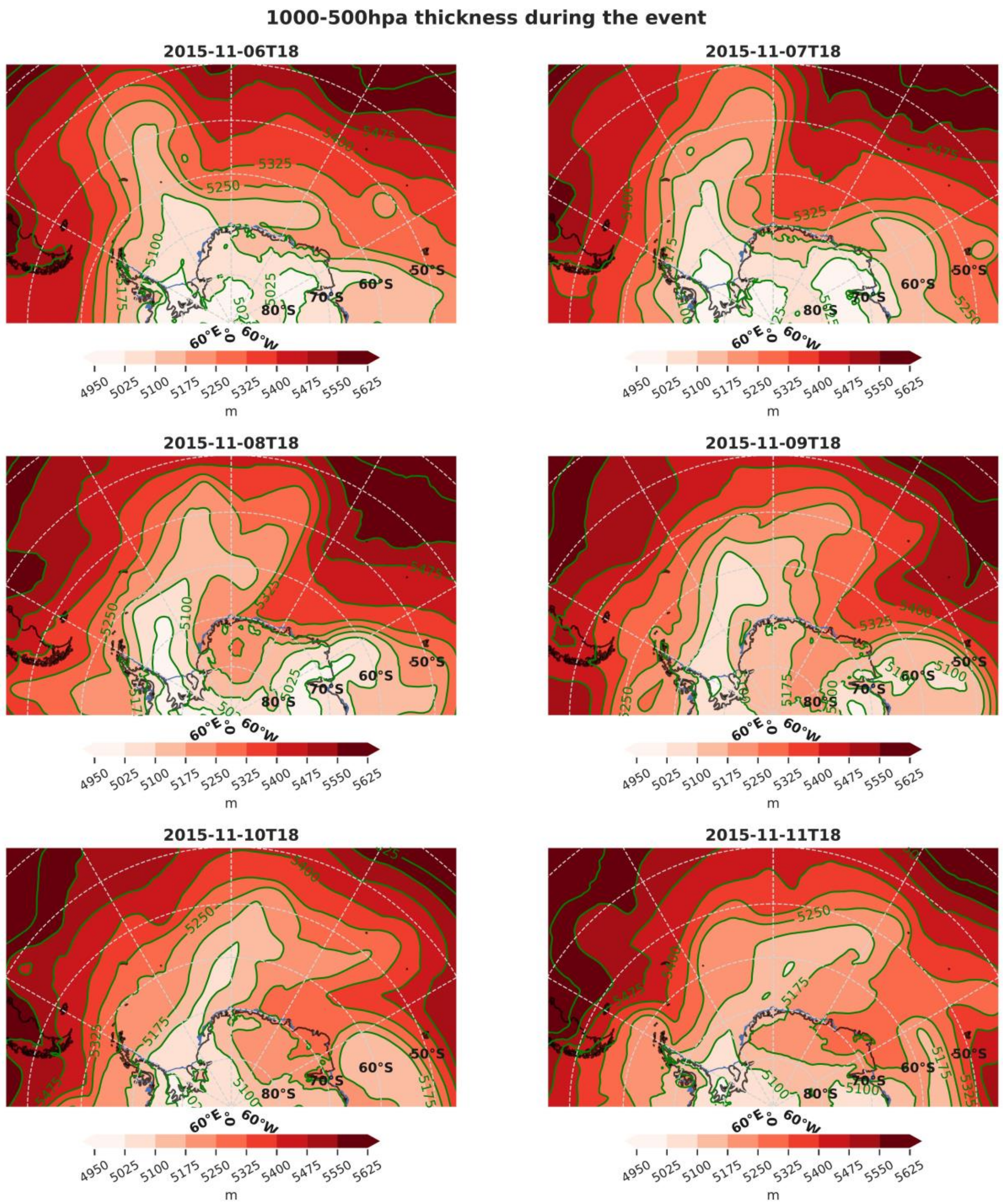

Figure 4.6: 1000-500 hPa thickness during and after the event. Data are shown for 18 UTC each day from 6 to 11 November.

This warm air advection was associated with the intrusion of a high-pressure ridge into the inland. Surface heat fluxes during the event in this high-temperature area (averaged over 5°E-35°E, 71°S-83°S, the selected box marked in Figure 4.5 c, d) revealed hourly changes in radiative and turbulent heat fluxes (Figure 4.7). Longwave (LW) radiation values (w m⁻

[2]) were less negative during the event, indicating downward LW radiation from clouds. Warmer conditions during the event also caused decreased heat loss from the ice sheet to the atmosphere. Clouds over the ice sheet reflected incoming solar radiation, decreasing net shortwave radiation.

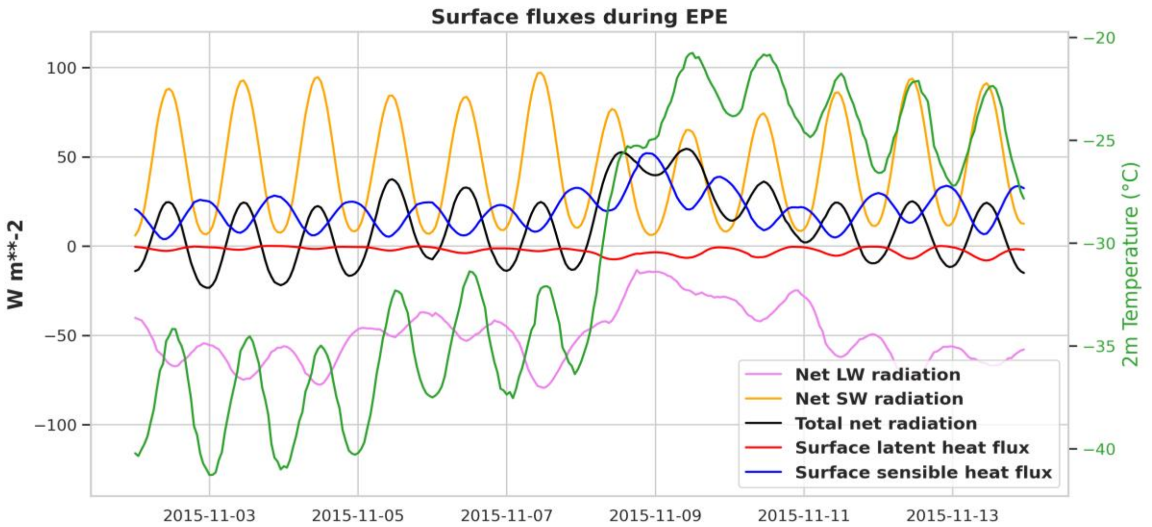

Figure 4.7: Radiative and turbulent surface fluxes over the box (5 - 35°E, 71 - 83°S) and 2 m temperature during the event. The time series of these variables are marked in different colors - net longwave radiation (magenta, (w/m^2)), net shortwave radiation (orange, (w/m^{-2})), Total radiation (black, (w/m^2)), surface latent heat flux (red, (w/m^2)), surface sensible heat flux (blue, (w/m^2)) and 2m-temperature (green, (˚C)).

Consequently, a warm airmass and clouds above the ice sheet surface resulted in a downward (more positive) surface sensible heat flux during the event. This demonstrates the warming due to cloud-longwave radiation and associated sensible heat fluxes contributing to changes in net radiation, primarily when 2-m temperatures increased sharply by nearly 15°C in less than 36 hours (from 1 UTC on 8 November to 10 UTC on 9 November). During similar EPEs, temperatures often rise significantly, with anomalies ranging from 10 to 20°C (as detailed in the climatological analysis in Chapter 3). These temperature spikes can introduce biases in ice core stable isotope records during snowfall events.

4.1.3 Genesis and track of the mid-latitude cyclone

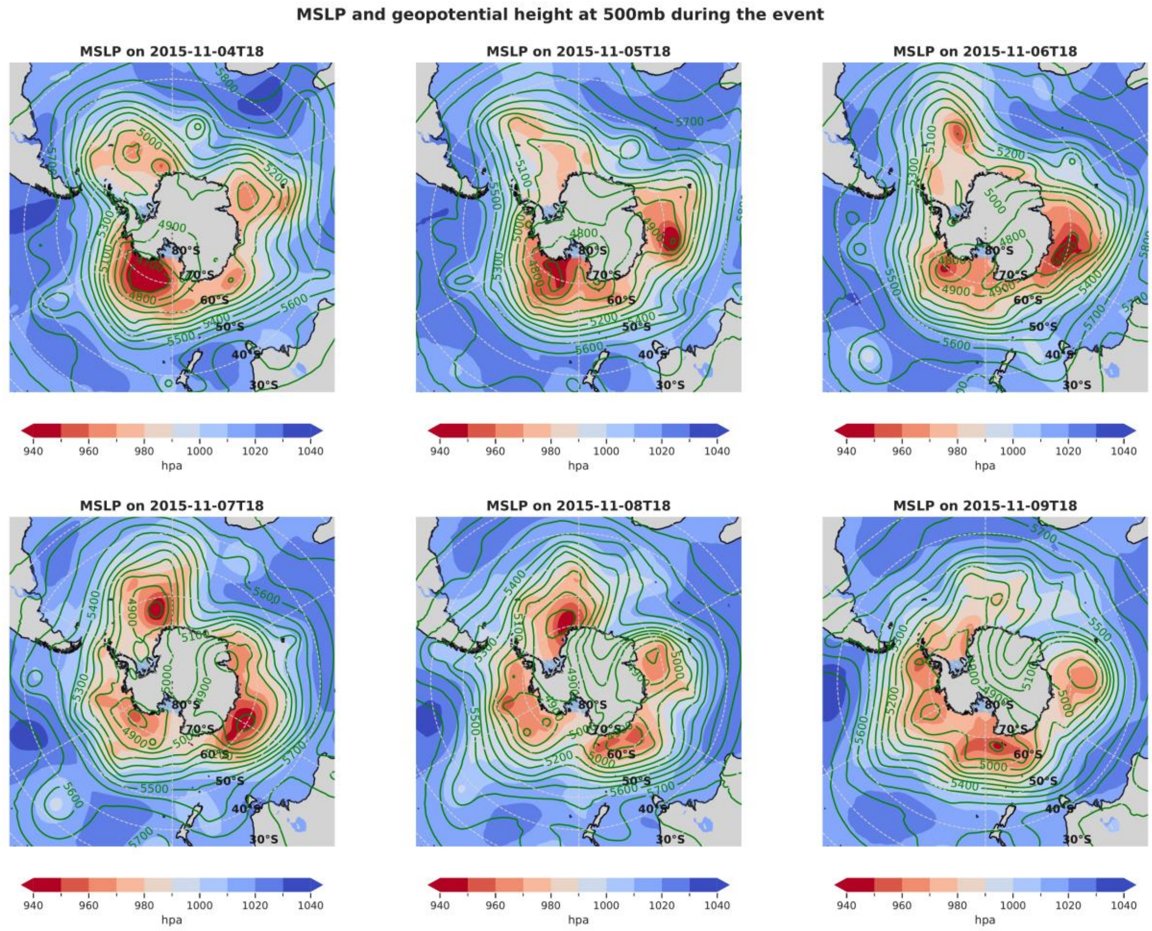

Figure 4.8: MSLP (shaded, hPa) overlaid by 500 hPa geopotential height (green lines, (m)) at 18 UTC on six days spanning the event.

Figure 4.8 illustrates the MSLP and 500 hPa geopotential height before and during the precipitation event. The synoptic processes behind this event were initiated on November 4. On that day, the area north of the Weddell Sea was characterized by multi-centered, quasi-stationary, low-pressure systems and the development of a highly amplified zonal wave pattern north of DML in the circumpolar trough (40°S - 60°S). On 5 November, the mid-troposphere had an upper-level short wave trough over the Weddell Sea (57°S, 15°W). This shortwave trough initiated the cyclogenesis, and as a result, a low-pressure system deepened near 55°S, 5°W in the South Atlantic on 6 November. On 7 November, this system underwent rapid deepening, with the lowest central pressure being ~950 hPa. In parallel with the deepening, this cyclone tracked poleward and arrived on the DML coast on 8 November. The MSLP exhibited a prominent zonal wave number 3 pattern, with low-pressure systems at 145°W, 120°E, and 5°W during the first week of November 2015. Between 7 and 8 November, a high-pressure ridge of record geopotential height developed east of the region, redirecting the low and facilitating substantial moisture transport towards the region. The 500 hPa geopotential height shows the extensive amplification of the planetary wave pattern in the mid-tropospheric north of the region, forming a high-pressure blocking ridge to the east. The sudden deepening of the low and the inland extension of the blocking ridge on 7 and 8 November served as the primary mechanisms steering the surface low toward land, generating a prolonged and narrow moisture pathway as an intense AR.

The extra-tropical cyclogenesis on 7 November occurred within the frontal boundary of warm and cold air masses. The frontal zones of large horizontal temperature gradient were on the eastern side of the surface low, and the interaction of warm and cold air over this boundary aided cyclogenesis. The 850 hPa potential temperature and gradient of 850 hPa wet-bulb temperature from the Polar WRF model (Figure 4.9b, 4.9c) confirm the presence of the frontal zones. The rising warm air over the frontal boundary led to the thick cloud on the eastern flank of the cyclone. The satellite images at the time of the event (Figure 4.10) also confirm the presence of a long band of cloud and moisture on the eastern side of the cyclonic system (Figure 4.9a). Figure 4.10 shows a typical AR cloud band structure with high moisture content from low-latitudes towards coastal Antarctica. These satellite images show the frontal cyclogenesis during the event and the poleward movement of warm low-latitude air. The northward movement of cold inland air led to the formation of a frontal boundary near the low's center and the system's deepening as it moved southwards (Figure

4.10). The landfall of the cyclone over DML on 8 November is also verified by the satellite images, with clouds extending well into the inland during the following hours.

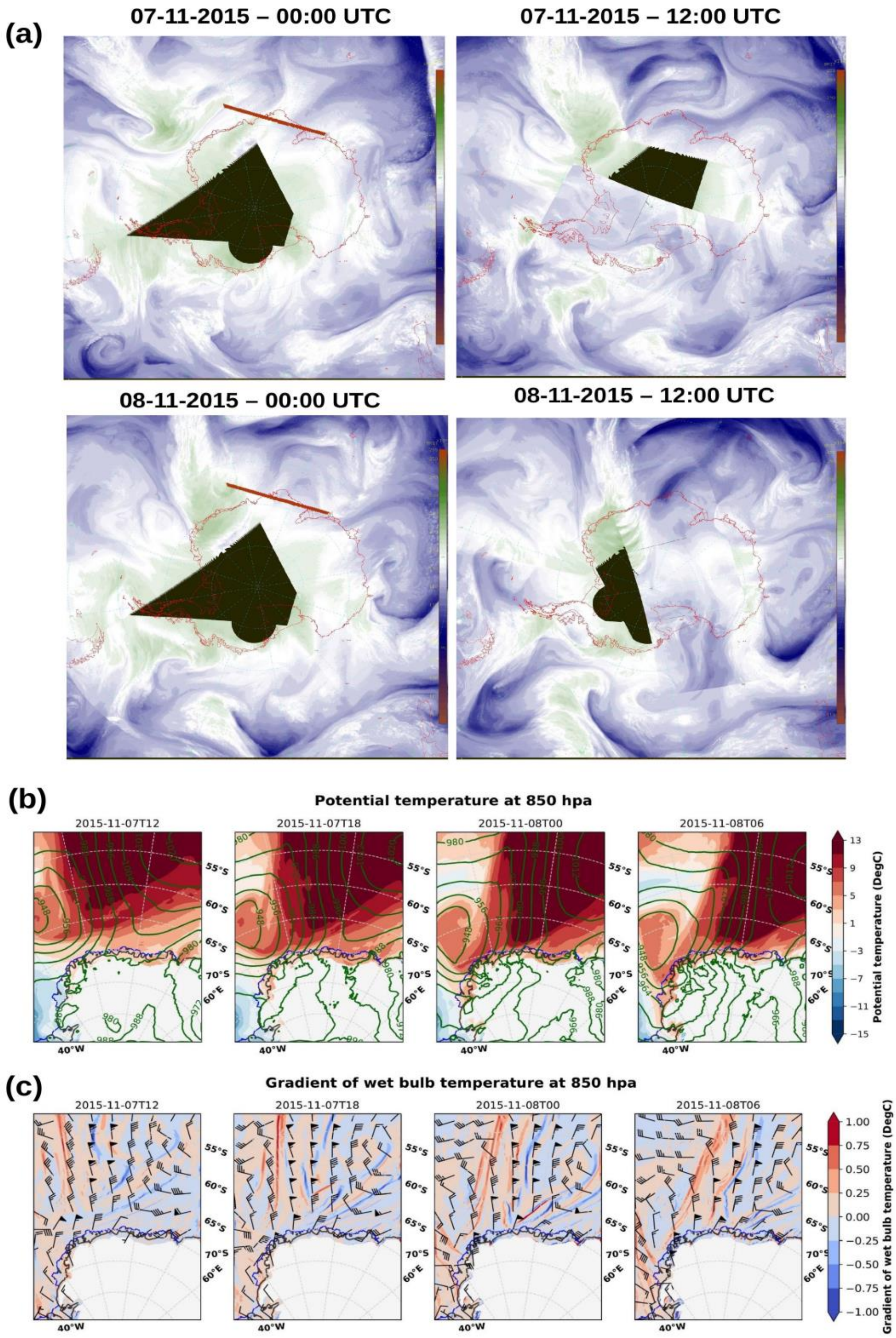

Figure 4.9: (a) Color-enhanced water vapor imagery (~6.7μ) for the selected hours before and during the event. (b) The potential temperature at 850 hPa from Polar WRF. (c) The gradient of wet bulb temperature and wind barbs at 850 hPa from Polar WRF output.

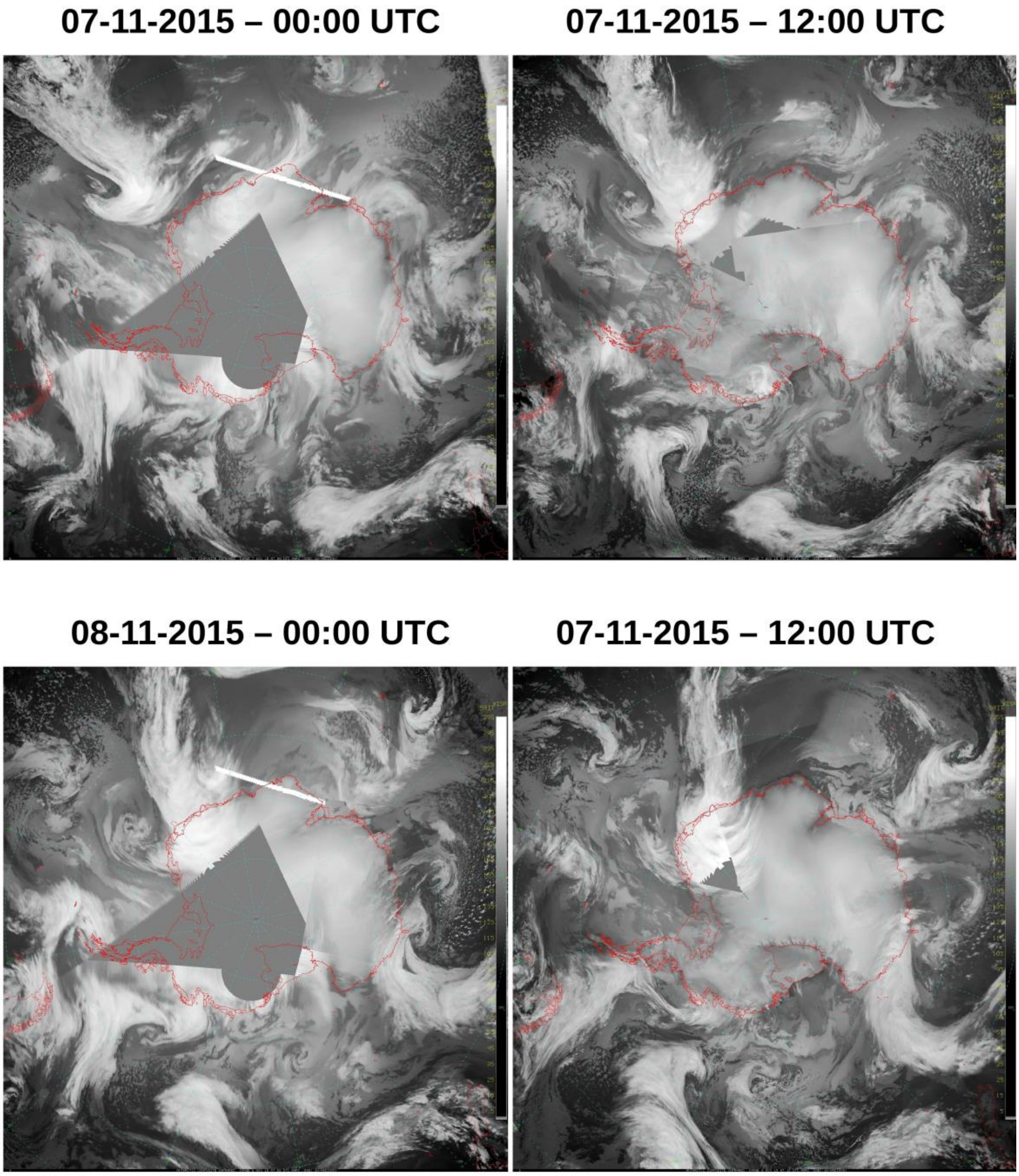

Figure 4.10: Infrared satellite imagery (IR) (~11μ) for the selected hours spanning the event.

4.1.4 Upper-level winds and the steering of the cyclone

To identify the influence of upper-level dynamics and the wind flow in the propagation of this event, the 250 hPa winds were analyzed. Figure 4.11 shows the 250 hPa wind and geopotential height from 5 to 10 November at 18 UTC each day. The upper-level winds show a highly amplified zonal wave across 50°S - 60°S with the genesis of the inland high-pressure ridge north of DML.

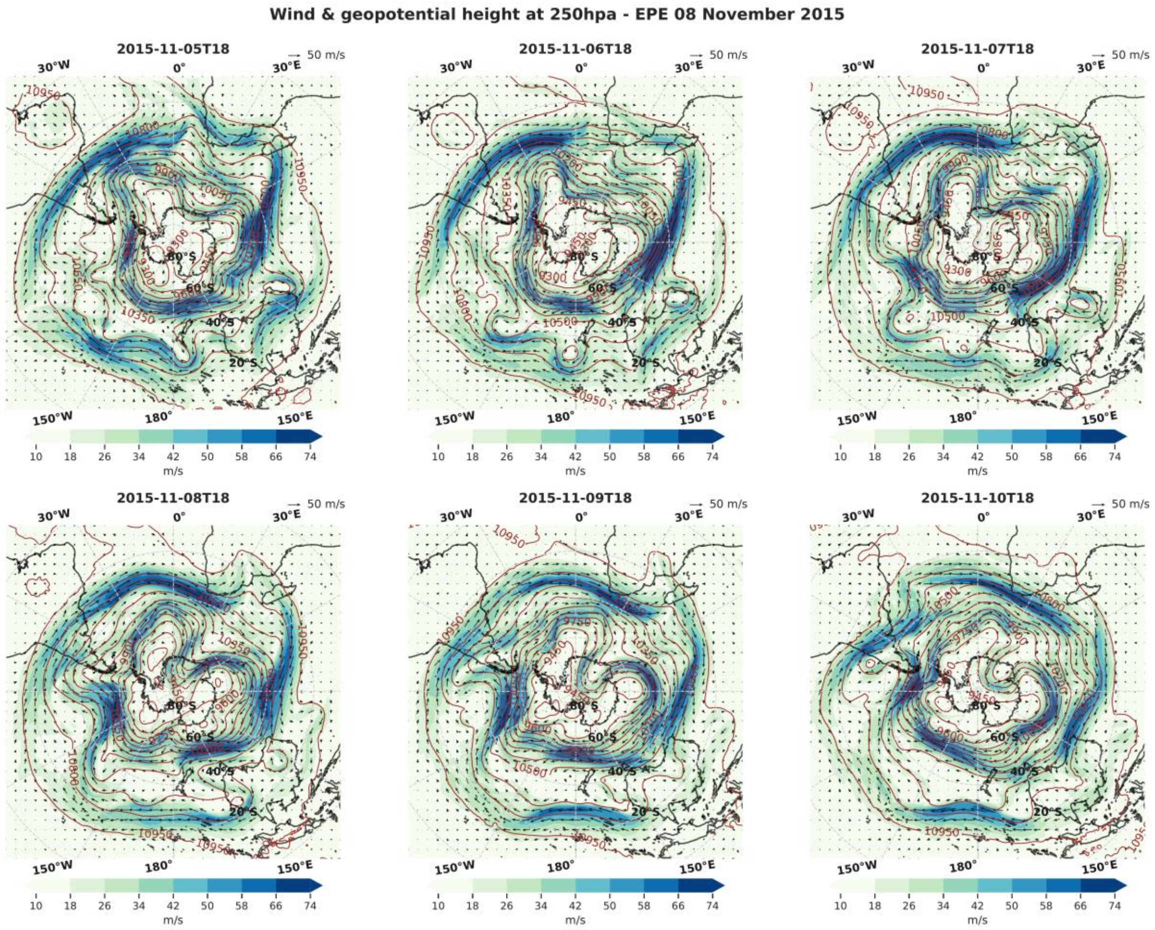

Figure 4.11: Wind speed (shaded, (m/s)), wind vectors, and 250 hPa geopotential height (brown lines, (m)) for different times spanning the event the event.

A pronounced quasi-stationary trough/ridge pattern started developing near 10°W on 5 November and amplified before the extreme precipitation days of 8 and 9 November 2015. The inland intrusion of the high-pressure ridge is evident from the upper-level geopotential height values, accompanied by changes in wind direction. This anomalous inland intrusion of the ridge, associated with the blocking mechanism, was the main feature responsible for directing the strong cyclone and high moisture levels to the landfall region (Figure 4.5). Notably, there was a close interaction between the sub-tropical and amplified polar jet streams north of the Weddell Sea (30°S, 20°W), where strong moisture uptake occurred (section 4.2.5). Through 6 and 7 November, the upper-level trough amplified and extended poleward, aided by a narrow band of strong meridional wind known as a 'jet streak' in the upper atmosphere, particularly over 10°W to 5°E.

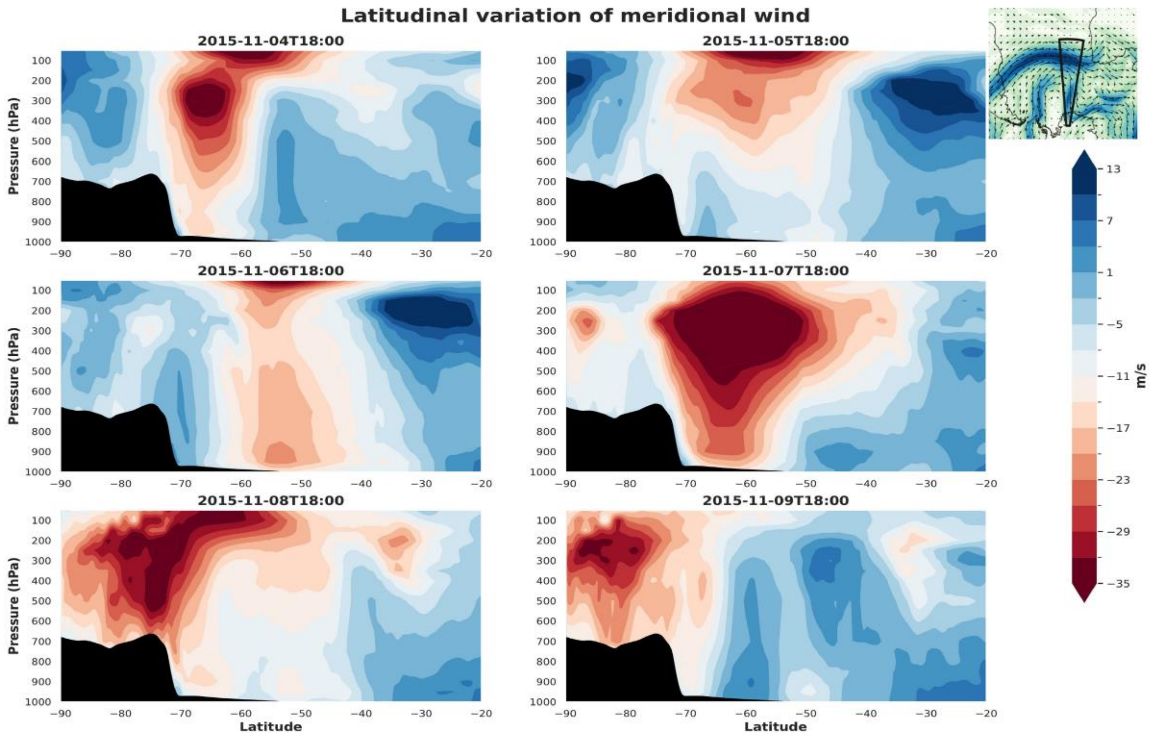

Figure 4.12: Vertical cross-section of the v component of wind (shaded, (m/s)) averaged through the jet streak area (5°W to 10°E) for selected times before the event. The insert shows the location of the respective cross-section (black box) relative to the wind speed (shaded) and wind direction (vectors). See Figure 4.11.

The core of this jet streak was on the eastern side of the upper-level trough and extended southward before the event. A cross-section of this strong wind region during the event confirms its banded form and poleward extension (Figure 4.12).

The meridional wind, averaged across longitudes 20°W to 10°E, is depicted in Figure 4.12. The strengthening and formation of the jet streak occurred on 6 and 7 November, generating a band of strong meridional wind over 50°S to 70°S at 18 UTC on 7 November. The core of this strong southward wind was close to 300 hPa, reaching coastal Antarctica on 8 November. These strong upper-level winds led to upper-level divergence balanced by low-level convergence and enhanced vertical motion. The vertical motion played a part in the deepening of the low-pressure system, and upper-level winds steered the system southwards. Therefore, the meridional jet streak in the upper atmosphere played a significant role in the sudden deepening of the low-pressure system and warm, moist airmass advection on 7 November. On 8 November, this band of strong wind reached coastal Antarctica and interacted with coastal orographic features.

The Hovmöller (time vs. longitude) diagram in Figure 4.13 illustrates changes in the zonal and meridional 250 hPa wind components averaged from 40°S to 70°S between 1 and 12 November 2015. The meridional wind (Figure 4.13a) revealed alternating strong winds from the south (positive values) to the north (negative values) over the circumpolar trough (Figure 4.13a, dashed line), beginning around 180°W on 1 November. This oscillation gradually propagated eastward over time, with significant northerly winds near 130°W on 2 November and 10°E on 7 November. This signifies the downstream movement of the Rossby waves, contributing to the development of the two strong ARs over the zones at 130°W and 10°E. The AR near 10°E was linked to the extreme event over DML, with a meridional jet streak giving strong northerly winds.

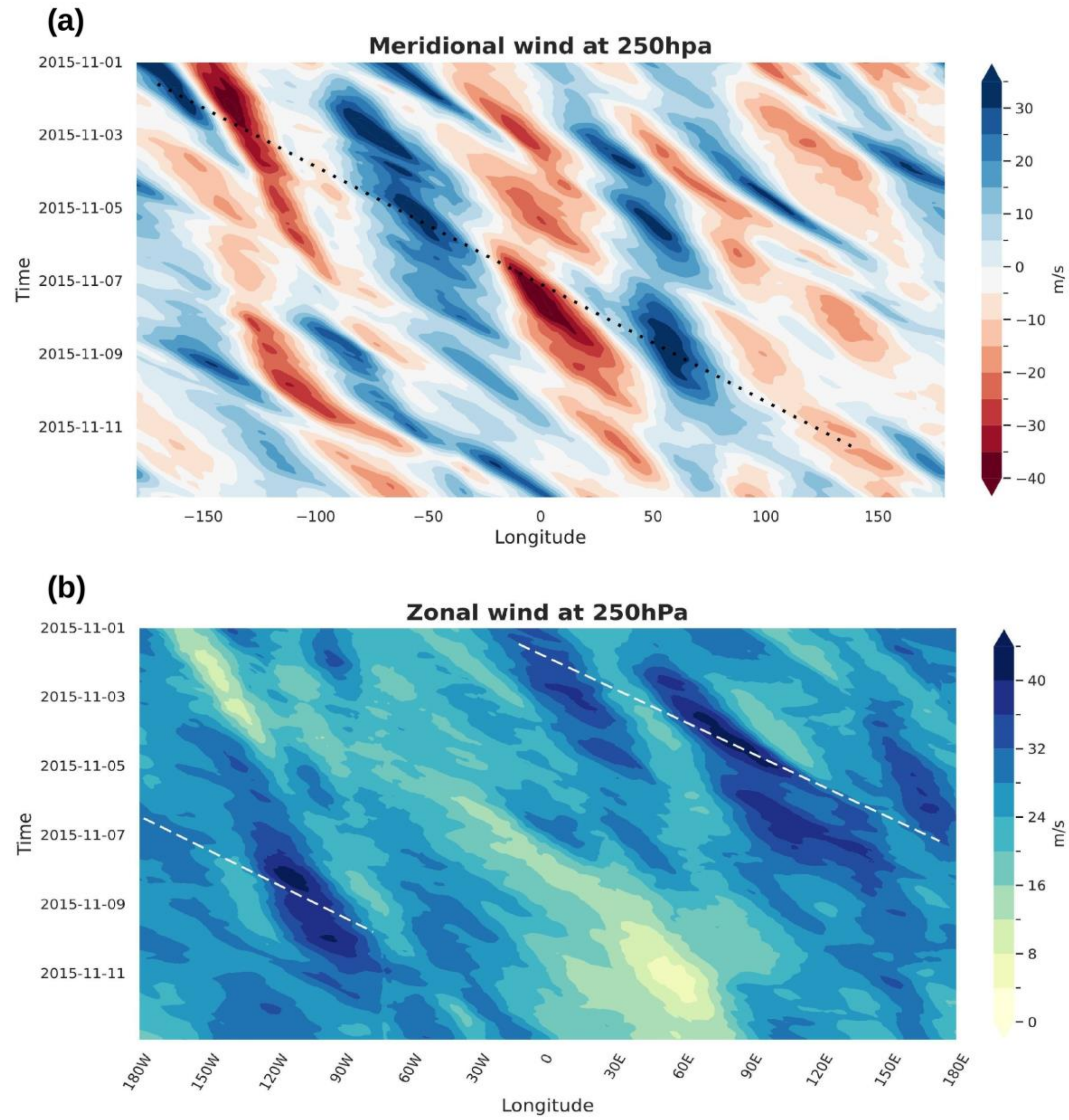

Figure 4.13: Hovmöller diagrams (time vs longitude, averaged between 40ºS to 70ºS) of a) meridional and b) zonal wind components at 250 hPa from 1 to 12 November 2015.

The zonal winds (Figure 4.13b) exhibited strong westerlies in the South Atlantic and Indian Ocean (30°E to 150°E) during the first week of November. However, from 7 to 10 November, the zonal winds weakened in the Weddell Sea and South Atlantic (30°W to 60°E) due to prevailing northerly winds and their eastward advancement. Simultaneously, the Ross Sea sector (180°W to 90°W) experienced strong zonal winds. The upper-level winds had a quasi-stationary wave pattern in the north-south flow, with changes in the wind pattern attributed to amplified planetary waves during the EPE period. The intensified Rossby wave pattern and the associated meridional jet streak in the upper atmosphere played a significant role as the primary steering mechanism. Wang et al., (2023) showed that blocking events are made possible by intensified Rossby waves within the circumpolar westerlies, coupled with the advection of warm and moist air through the western flank of these blockings. This study has also shown that these episodes of blocking make a significant contribution, accounting for almost 30% of EPEs over East Antarctica.

4.1.5 Moisture transport associated with the atmospheric river

Hourly IVT fields associated with intense moisture transport in the form of an AR and the development of the deep low in 6-hour intervals from 18 UTC on 6 November 2015 are shown in Figure 4.14. A pool of high IVT air, with values of ~1000 kg/m^{-1} s^{-1}, was present over the South Atlantic (30°S - 40°S, 30°E - 5°E) on 6 November. This region coincided with the northern end of the amplified upper-level trough discussed in Section 4.2.4, interacting with the sub-tropical jet stream where strong moisture uptake occurred (Figure 4.15). The moisture transport was strengthened and started to orient meridionally on 7 November, which was associated with the strengthening of the blocking high-pressure ridge to the east and the deepening of the low to the southwest. This quasi-stationary atmospheric pattern helped in the poleward steering of moisture and the formation of an AR that elongated southward along the eastern flank of the extra-tropical cyclone.

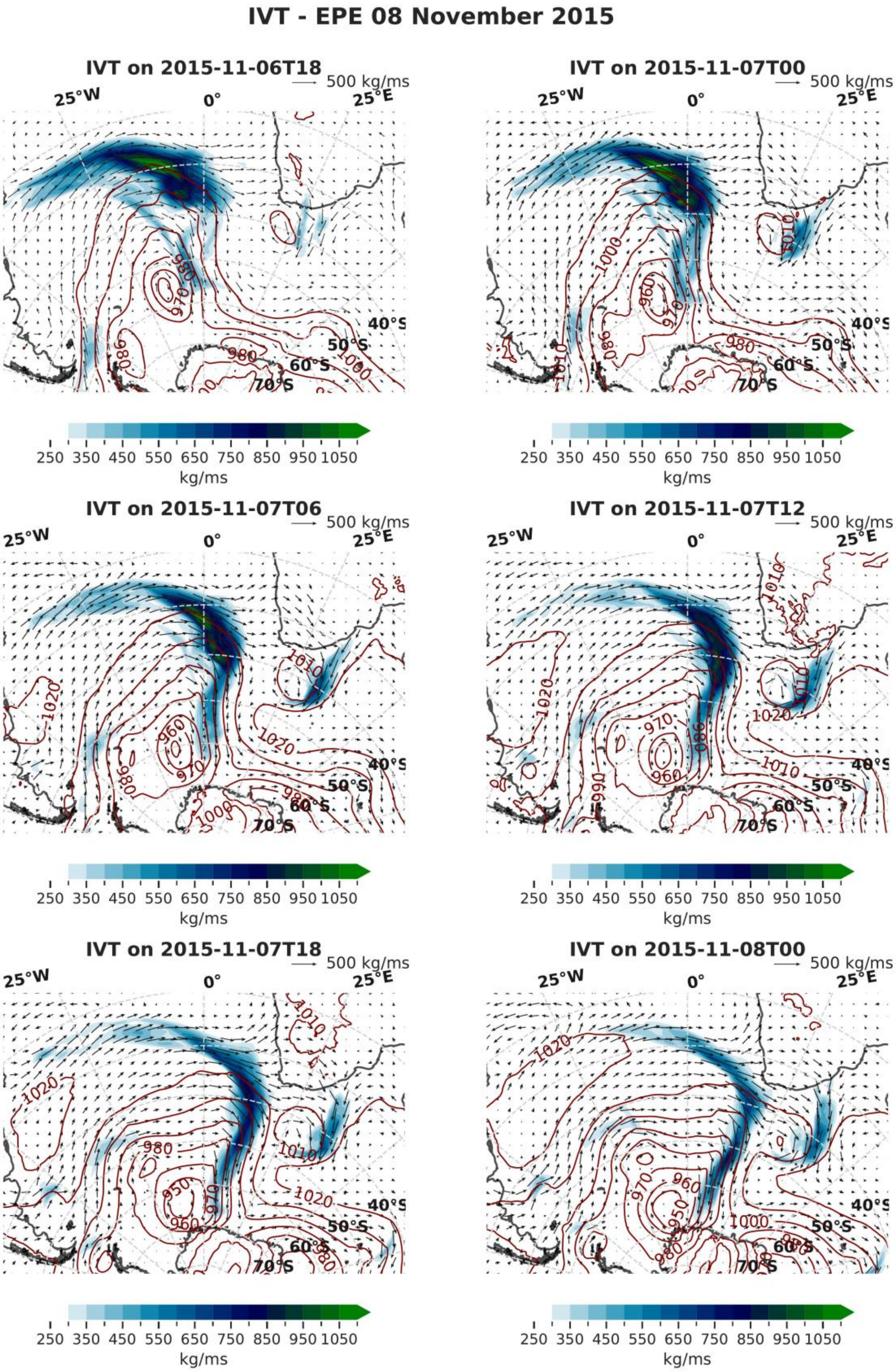

Figure 4.14: Temporal evolution of the AR, showing the vertically integrated vapor transport (IVT) (shading, (kg/ms)), moisture transport direction (vectors), and MSLP (brown lines, (hPa)) for 6-hourly intervals before the precipitation event.

To investigate the vertical structure of IVT, we examined the cross-section of moisture flux for the entire vertical atmospheric column along the eastern flank and warm sector of the surface low (averaged between longitudes 5˚W to 10˚E) (Figure 4.15). The contours of specific humidity (violet) and wind speed (tan) are overlaid. At 18 UTC on 6 November, large areas of enhanced moisture flux at the northern extent (nearly 30°S to 40°S) of the cyclone. Enhanced moisture flux values over this region on 7 November in the lower troposphere (750 hPa to 950 hPa) were mainly controlled by high specific humidity values and were the major moisture uptake region. The meridional form of this moisture pool took place throughout the remaining hours of 7 November with the support of upper and lower-level winds. The moisture flux had high values from 300 hPa to the surface. These plumes of intense moisture were heterogeneous over the lower troposphere and became two major bands of moisture flux over 60°S and 38°S at 12 UTC on 7 November. This two-band structure was also reflected in the coastal region's temporal distribution of precipitation at the PE station and IND33 (Figure 4.1d, Figure 4.2b). The poleward orientation and eastward movement of this long, narrow band of moisture were largely driven by the deepening and eastward movement of the low-pressure system, which made landfall over the coastal region on 8 November. The highly amplified zonal wave and blocking ridge contributed to the moisture transport into the coastal region associated with the cyclone's landfall. The AR formation and meridional elongation of the high moisture flux occurred within 24 hours. This occurred at the same time as the sudden deepening of the low-pressure system in the Atlantic Ocean steered by the upper-level winds. The onset of precipitation in the early hours of 8 November coincided with the interaction of these intense moisture bands with the orographic features of coastal DML.

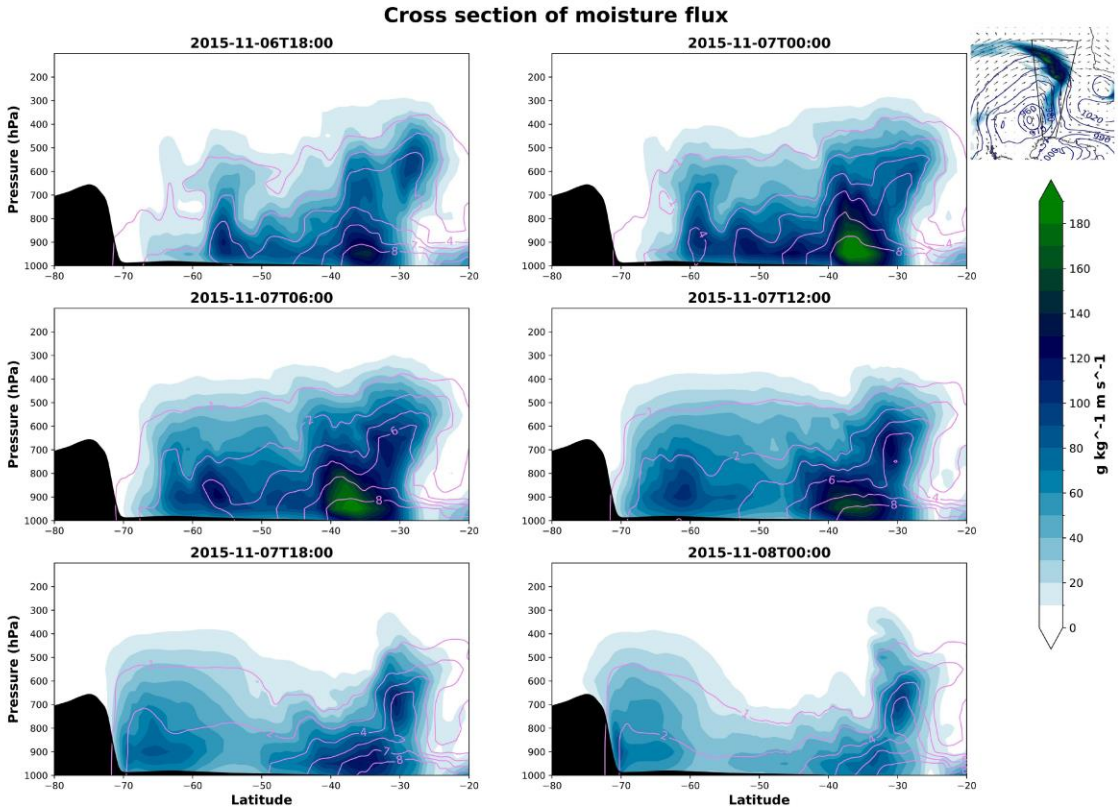

Figure 4.15: Vertical cross-sections of moisture flux (shaded, (g kg^{-1} ms^{-1})), specific humidity (violet lines, (g/kg)), averaged through the eastern flank of the cyclone (5˚W to 10˚E) for different times corresponding to Figure 8. The insert shows the location of the respective cross-sections (black box) relative to the IVT (shaded), MSLP (brown lines), and IVT vectors. See Figure 4.14.

4.1.6 Orographic Enhancement

On 8 November 2015, as previously discussed, coastal precipitation peaked due to the cyclone's landfall and the arrival of an AR from the South Atlantic. The region also experienced winds from the N-NE direction, which advected warm, moist air from northern latitudes. There is high precipitation over the oceanic region just north of the DML coast, which is due to the interaction of warm airmass with cold air from the continent inland. This interaction enhanced the rapid cooling, condensation, and precipitation near the coastal margins and over coastal ice shelves. The precipitation values were of record magnitude (Figure 4.5) in most of coastal DML. However, the distribution of precipitation was not homogeneous, and there was high spatial variability along the coast, with a three-band pattern of high and low values (Figure 4.16a). To understand better this high spatial variability, we utilized results from Polar WRF simulations on high precipitation days. Using the model output, we analyzed the vertical distribution of atmospheric variables during the event. Specifically, we chose a west-east oriented cross section that showed significant spatial variability in precipitation (Figure 4.16a). The cross-section captures the complex orography of the coastal region with the vertical variation in variables such as omega, mixing ratio of water vapor and snow, relative humidity, and moisture flux (Figure 4.16b, 4.16c, 4.16d, 4.16e, 4.16f) at 12 UTC on 8 November 2015, when hourly precipitation reached its peak. The orography of the region is complex, with steep slopes over a short distance due to mountain regions, nunataks, and ice rises. The synoptic patterns confirm the intense moisture transport in the form of ARs reaching the coastal region on November 8 (Figure 4.14). The interaction of warm, moist airmass with the orography of the region is illustrated in the vertical cross-section analysis, where Figure 4.16b shows the omega (pa/s) values with wind vectors showing vertical wind directions. The effect of coastal orography is evident in the vertical distribution of omega (pa/s) values along this selected cross-section zone (Figure 4.16b). Alternative positive and negative omega values were present over the lower troposphere, and significant negative values near the steep gradient zones (Figure 4.16b). The negative omega values indicate strong vertical motion of air parcels, which results in the orographic lifting and cooling, leading to enhanced precipitation over these windward regions. The regions with high precipitation values are near steep, complex terrain with strong updrafts, especially near the 5°W, 5°E, and 10°E. Alternate downdrafts, with relatively lower moisture content, balance these strong updrafts, resulting in minimum precipitation values.

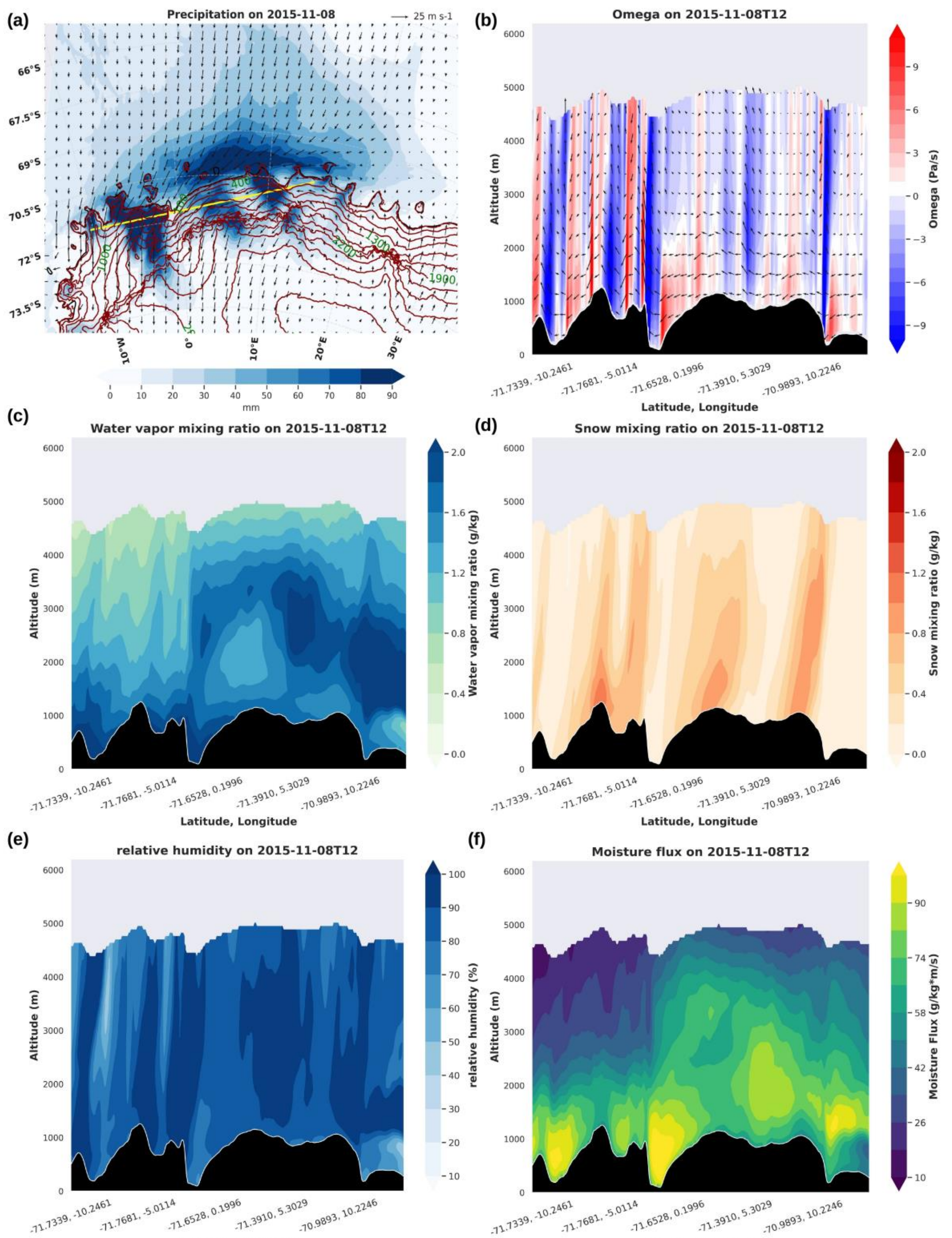

Figure 4.16: (a) Similar to Figure 1a. The area selected for vertical cross-section analysis is denoted with a yellow line. Vertical distribution of variables at 12 UTC on 8 November, 2015 over coastal DML from Polar WRF model output from the inner domain of 3 km resolution (b) Omega (pa s^{-1}), (c) Water vapor mixing ratio (g kg^{-1}), (d) Snow mixing ratio (g kg^{-1}), (e) Relative humidity (%), (f) Moisture flux (g kg^{-1}m s^{-1}).

The vertical wind vectors confirm this rapid updraft and downdraft pattern in the lower troposphere and indicate the close interaction of advected airmass with the complex orography of the region. The presence of alternating updraft-downdraft wind regions associated with the complex coastal orography was also demonstrated by Gehring et al., (2022), which explains the role of foehn and lower troposphere sublimation in creating low precipitation bands along the coast (Gehring et al., 2022). The cross-section of mixing ratio values of both water vapor (Figure 4.16c) and snow (Figure 4.16d) shows the distribution of moisture in different levels along the selected plane. The mixing ratio of water vapor shows the moisture advection in the lower atmospheric levels between 2,000 m to 4,000 m above sea level. This indicates the strong moisture associated with the AR in the lower troposphere, from the northeast region of DML. The near-surface and steep orographic regions show low values in the water vapor mixing ratio, complemented by high values of snow mixing ratio (Figure 4.16d), indicating the snowfall formation upon interacting with the orographic features. The snow mixing ratio has a distinct three-band structure with high values in the vertical distribution near the steep gradient terrain regions. This is in close agreement with the snowfall distribution pattern on 8 November 2015 (Figure 4.1a, 4.16a), with high values near the windward side of coastal orographic features. Similarly, the lower atmosphere had distinct vertical columns of high moisture content with 3-4 bands of completely saturated areas (RH = 100%) (Figure 4.16e). These highly saturated areas are also near the steep-gradient orographic features along the line of cross-section analysis. The derived high moisture flux regions (Figure 4.16d) also correspond to the coastal high precipitation bands, which align with steep-gradient orographic areas oriented perpendicular to the N-NE winds during the event. Hence, peak precipitation values were on the windward side of these gradients, while the leeward side experienced minimal values. The precipitation bands over the coastal region during this EPE event were associated with the four zones of high moisture flux values due to the orographic enhancement of winds and moisture upon reaching the coast. This indicates that despite considerable moisture transportation to coastal Antarctic areas, heavy precipitation was focused on specific locales, notably the windward side of steep orographic features, and implies that the precipitation distribution depends on the orientation of the coastal orography.

4.2 Conclusions

This chapter presents a detailed analysis of an EPE over DML on 8 and 9 November 2015, which marked the highest precipitation event at the coastal ice core site IND33. The study examined the role of orography in controlling precipitation distribution and triggering extreme atmospheric features during the landfall of the EPE. The event was initiated by a deep low-pressure system moving southward from the South Atlantic, influenced by a high-pressure ridge of record strength to the east. This interaction generated a strong AR originating over the South Atlantic between 30°S and 40°S. Using ERA5 data to analyze synoptic patterns, we identify quasi-stationary low-pressure systems over the Weddell Sea and an upper-level short-wave trough that initiated cyclone formation.

Examining the upper atmospheric data revealed a meandering jet stream and the intrusion of a high-pressure ridge east of DML a day before the event. This ridge acted as a blocking feature, steering the surface cyclone southward to make landfall over the coast. Hourly satellite images illustrated the frontal cyclogenesis, intensified by the advection of a warm, moist airmass towards the south. The interaction between this warm airmass from lower latitudes and the cold air from Antarctica's interior created a frontal boundary, leading to a frontal occlusion. A jet streak in the upper atmosphere triggered the sudden deepening of the mid-latitude cyclone by enhancing lower-level convergence, steering it poleward over the South Atlantic Ocean. Significant moisture uptake occurred on the eastern flank of the cyclone in the South Atlantic, between the 35°S-40°S band. During this EPE, extreme conditions were present in the upper and lower atmosphere, including a strong low-pressure cyclone with associated frontal structure, a high-pressure ridge extending inland, intense moisture influx as an AR, amplified Rossby waves, and a jet streak in the upper atmosphere. To complement the reanalysis data, this study employed Polar WRF to understand the influence of orography on precipitation distribution in coastal DML. Precipitation distribution exhibited a high-low banded structure, with more precipitation on the eastern side of steep slopes in the coastal region (Chapter 3). Even with intense moisture transport such as ARs, local orography heavily influences precipitation along the Antarctic coast. Such case studies can reveal unique atmospheric patterns during such events. At the same time, high-resolution models with improved orographic representation can demonstrate the detailed precipitation distribution influenced by local orography and help to explain the small-scale, complex features during precipitation over coastal Antarctica.

Chapter 5

The influence of extreme meteorological conditions on ice core records

Introduction

The surface snow accumulation or surface mass balance (SMB) over the ice sheet is influenced by numerous glaciological and meteorological processes, including precipitation, blowing snow, sublimation, and erosion (Lenaerts et al., 2019; Mottram et al., 2021). Sudden changes in surface snow accumulation often result from large meteorological events, such as significant precipitation events or major blowing snow episodes (Braaten, 2000). Precipitation is the primary input for accumulation, increasing snow surface height, while near-surface winds can either remove or add snow from a location (Souverijns et al., 2018). However, the relationship between precipitation and accumulation in wind-dominated regions needs to be better understood (Braaten, 2000).

Wind-driven accumulation and ablation play significant roles in the local net surface accumulation over the ice sheet (Bromwich et al., 2004; Scarchilli et al., 2010), contributing to interannual variability. Blowing snow, where winds lift snow into the air and transport it, and drifting snow, where snow is moved along the surface, can significantly alter the snow distribution, especially in areas of complex orographic in coastal Antarctica (King et al., 2004).

Ice cores from coastal regions are often drilled at high-elevation locations fringing ice shelves, called ice rises, which have high accumulation rates. Such areas can provide high-temporal resolution ice cores covering hundreds of years (Pratap et al., 2022). The highest point of an ice rise is ideal for drilling cores, as these regions experience minimal disturbance from horizontal ice flow (Matsuoka et al., 2015). Wind flow around ice rises also affects accumulation variability, significantly impacting snow redistribution. Consequently, seasonal variations in blowing snow transport could introduce errors in estimating annual mean temperatures using oxygen isotope ratios, particularly if there is a bias towards snow loss or gain in a specific season (Fisher et al., 1983). Thus, understanding the influence of meteorological conditions on annually-dated ice core accumulation is crucial for accurately interpreting these paleoclimate records.

While atmospheric reanalyses can indicate the occurrence of precipitation and surface winds over the Antarctic ice sheet, surface snow height (SSH) measurements are necessary to accurately identify changes in ice surface and net SMB values. However, due to technical challenges, these measurements are limited to a few locations in Antarctica (Braaten, 1997, 2000; Gorodetskaya et al., 2013, 2015). This chapter utilizes high-resolution SSH measurements from Princess Elisabeth (PE) station in Dronning Maud Land (DML) to quantify the impact of extreme meteorological conditions on sudden and episodic SSH changes. It also examines the significant role of these extreme conditions in shaping annual ice core accumulations, particularly focusing on precipitation and wind redistribution characteristics.

5.1 Snow surface height and extreme events

5.1.1 Temporal variability of surface snow heights (SSH) at Princess Elisabeth (PE) station, DML

5.1.1.1 The SSH changes during 2009-2019

High-resolution, in-situ snow surface height (SSH) measurements from the PE station were available from 2009 to 2019. The experimental methods, details of measurements, and instruments at the station are described in Chapter 2.

The snow surface height sensor provides precise elevation measurements between the snow surface and the sensor, which are converted into snow height changes by calculating their difference. Daily changes in SSH are determined by computing the difference in mean snow height values between each pair of consecutive days. Figure 5.1 depicts high-resolution surface elevation values alongside cumulative SSH changes derived from the daily values. Both elevation (blue line) and cumulative SSH change (red line) exhibit similar patterns. Yet, the cumulative values represent the absolute magnitude of height change, excluding periods with missing data. Over 2009 to 2019, the location had a positive accumulation trend, with a cumulative snow height change of 2.26 m. Notably, the cumulative SSH patterns have sudden and episodic changes, resulting in significant fluctuations in the SSH. Different processes, including precipitation, blowing or drifting snow, sublimation, snow melt, and evaporation, can cause changes in surface accumulation. However, many of these sudden and large fluctuations in SSH are the result of precipitation and wind-induced changes. Additionally, days with small SSH changes are present, with a lesser influence on the total change. These patterns underscore the complexities of surface snow accumulation, primarily driven by a range of meteorological and glaciological processes.

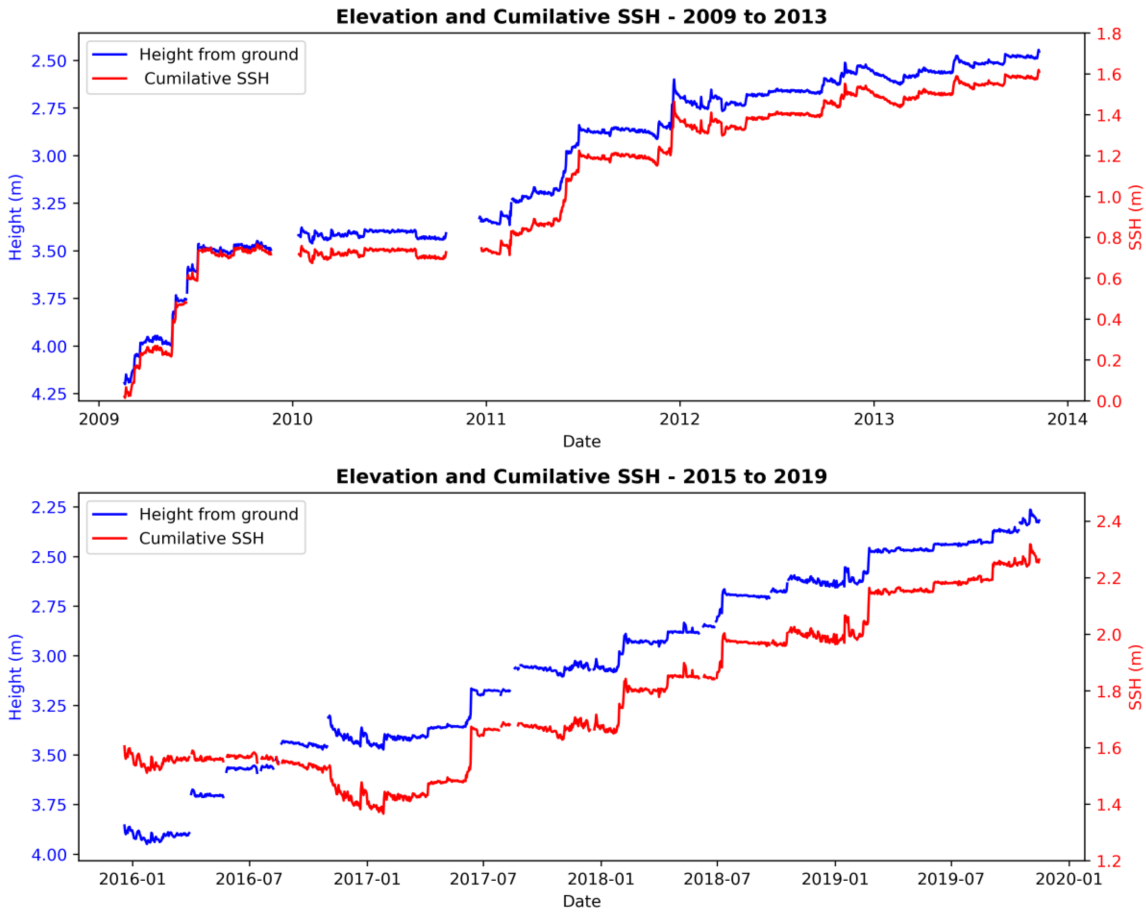

Figure 5.1: Temporal variability of daily snow surface to sensor elevation (blue) and cumulative SSH change (red) for 2009 to 2019 at Princess Elisabeth (PE) station. Measurements are illustrated in two-time ranges where the missing data for 2014 and 2015 have been omitted.

The analysis of annual accumulation on the ice surface reveals substantial interannual variability. In 2009, there was high snow accumulation caused by a few significant accumulation events, i.e., more than 50% of positive snow accumulation happened in nearly 13% of accumulation days. Similarly, in 2011, anomalously high snow accumulation occurred, with a significant contribution from a few atmospheric rivers (ARs) occurring during the winter and summer seasons (Gorodetskaya et al., 2014). Conversely, in 2010, the dominance of small-magnitude accumulation events was followed by snow removal, resulting in zero or negative net accumulation. The ice core records from the nearby Derwael ice rise showed these signals in annual accumulations in the years 2009 and 2011, which is attributed to high accumulation events (Philippe et al., 2016). A detailed analysis of daily SSH changes can give insight into the role of atmospheric parameters behind these sudden changes. Overall, the location experienced a net positive accumulation, and detailed analysis of in-situ surface meteorological parameters provides insights into the underlying processes driving sudden, episodic changes in SSH.

5.1.1.2 Daily SSH changes and the role of extreme meteorological conditions

The high-resolution daily SSH values are compared with the observed meteorological parameters of wind speed, wind direction, and 2-m temperature from the instruments attached to the AWS as the height sensor. Also, precipitation from the ERA5 model was used to understand precipitating systems at the location. The role of extreme meteorological conditions in causing surface accumulation changes is analyzed in the following. The selection of threshold values for extreme surface variables is based on percentile criteria calculated using daily values from 2009 to 2019. As per extreme value criteria, the days with precipitation greater than the 90th percentile of the long-term daily precipitation and wind speed values were taken as extreme precipitation (EP) and strong wind (SW) days. The threshold values for EP and SW days were found to be 3.08 mm and 11.095 m/s, respectively.

Figure 5.2 illustrates the daily changes in SSH (yellow line) and cumulative SSH (blue line) during four different time intervals (P1, P2, P3, P4) covering the total observation period. The days with little or no precipitation with high wind speeds are categorized as SW-only days, and precipitating days with moderate or low wind speeds that did not cross the threshold criteria are identified as EP-only events. The category EP accompanied by SW events is the high-intense extreme meteorological conditions, with heavy precipitation and significant wind speeds, which can cause significant changes in snow accumulation due to the high snowfall and redistribution of the precipitated snow (Chapter 3). This is also confirmed by in-situ SSH values showing a significant role for EP and SW conditions in making large-magnitude changes.

Figure 5.2: Daily snow height (yellow) and cumulative SSH (blue) changes for the measurement period, are represented in four-time intervals (P1, P2, P3, P4). Extreme precipitation (EP) and strong wind (SW) dates are indicated using separate markers, where EP (red star), SW (black circle), and combined EP and SW days (red star inside a black circle).

These sudden changes are infrequent and often smaller in number compared to the total number of days in each period. Co-occurring EP and SWs are more pronounced in causing high SSH change values, which are associated with strong easterlies or north-easterlies, advecting moisture from ocean areas and causing large deposits of snow. The SW-only events are more frequent during winter, mostly due to the presence of strong katabatic winds from the continental interior during these colder months.

5.1.1.3 Interannual variability in SSH and the contribution from extreme events

There is a large interannual variability in the annual sum of positive daily SSH changes and the corresponding sum of negative daily changes. These changes are mainly controlled by extreme precipitation and surface wind conditions. The contributions from these extremes in the increase and decrease of SSH are analyzed separately for each year (Figure 5.3). Since these events make changes in SSH over multiple days after the occurrence, three consecutive days are considered during each event for calculating their contribution to SSH changes. The number of extreme days and percentage contribution of these events in positive and negative changes in SSH are detailed in Figure 5.3. Annual positive snow accumulation values range between 0.7 m to 1.57 m, and large differences between each year are related to the number of precipitation and wind events (Figure 5.3 (a)). Large positive accumulation occurred in 2009 and 2011, with values of ~1.5 m per year, and the smallest during 2013, with nearly 0.69 m of increase in SSH. Similar changes are also observed in annual ice core accumulations from nearby regions (Philippe et al., 2016), indicating the influence of synoptic-scale precipitation events during these years. During 2009 and 2011, more than 50% of positive snow accumulation at this location was contributed by anomalous high-precipitation events. For the annual positive SSH changes, the contribution from combined EP and SW events was dominant during 2009-2013, and later SW-only days (the influence of strong winds) also showed a significant contribution to the increase in snow accumulation. From 2016 to 2019, SW events also contributed ~30% more to the annual increase in SSH compared to precipitation events.

Similarly, SW days have a major role in negative snow height changes, as indicated in most of the years when considering a decrease in SSH (Figure 5.3 (b)). Negative SSH also shows a large interannual variability, controlled by the number of SW days, and the annual values range between -0.7 and -1.1 m. The largest negative change (-1.1 m) occurred during 2016, where SW events contributed 42% towards this change. During 2009, along with the contribution of the SW events (34%), many combined EP and SW events contributed nearly 24% towards the negative snow height change.

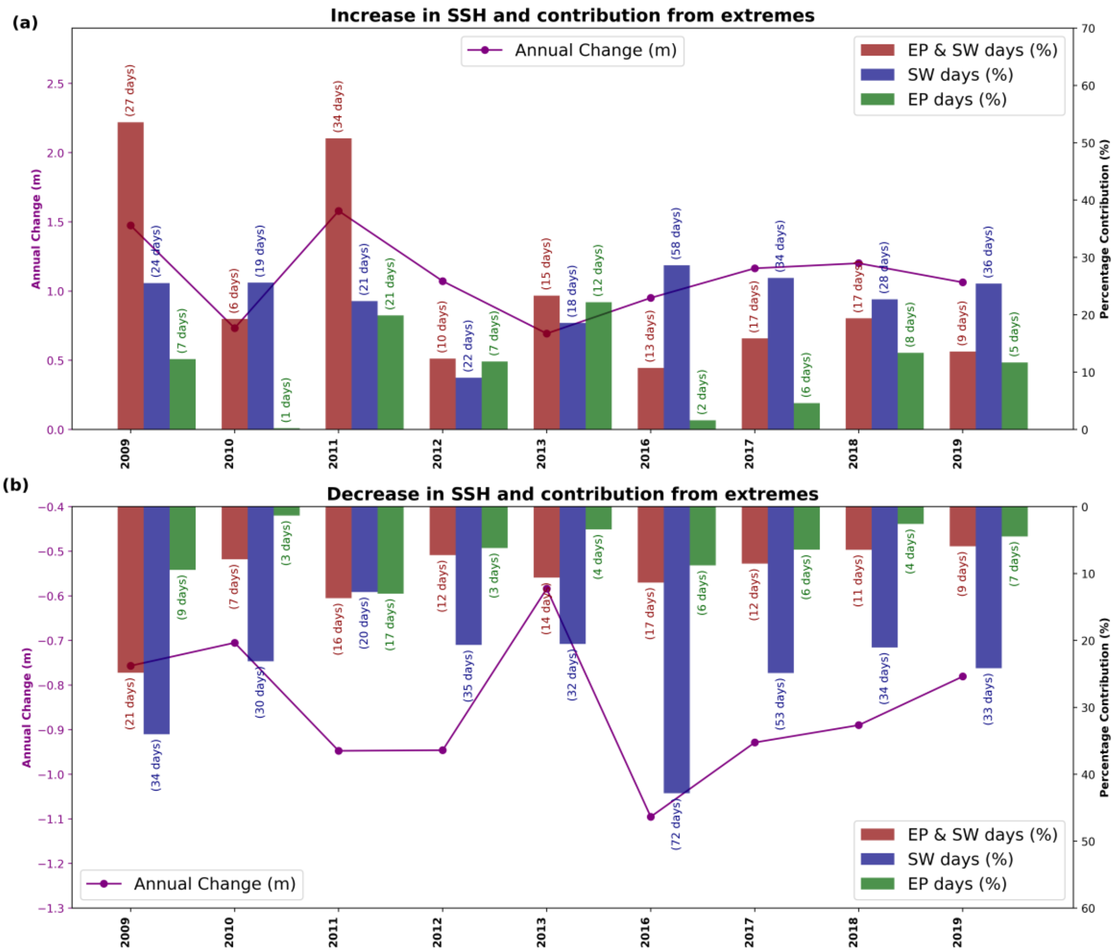

Figure 5.3: Interannual variability of annual SSH change (purple) separately for (a) positive SSH and (b) negative SSH days. The contribution from extreme conditions through combined EP and SW days (red bar), SW-only days (blue bar), and EP-only (green bar) for a total change in each year is given.

This indicates the major role of wind-induced decreases of SSH through both blowing and drifting snow episodes. The redistribution of snow is very variable, spatially and temporally, and depends on the nature of the snow particles and atmospheric conditions, such as wind speed (Bintanja & Reijmer, 2001; L. Li & Pomeroy, 1997). Also, over coastal Antarctica, the blowing and drifting snow effects can shape features of blue ice areas (kilometer scale), which are locations where all the loose surface snowfall has been removed, exposing the underlying compacted ice.

5.1.1.4 Role of wind direction on annual SSH change

Along with the wind speed-induced changes in surface snow, the importance of the wind direction in the positive and negative changes of surface snow variability is also analyzed. The wind rose (Figure 5.4) shows the spread in the direction of the wind at PE for the observation period. The wind direction ranges from ENE to SW, with a major contribution from southerlies (S) (~23%). The occurrence of higher wind speeds from an easterly direction is associated with the high-magnitude snowfall events causing large SSH changes. Since there are days with high SSH changes due to the wind, the wind direction during these wind-induced events is considered in detail. The dominant directions in the wind pattern are identified and grouped into two major directions. The winds blowing from between 30 to 155 degrees are considered here as 'Easterlies,' and winds in the range 155 to 280 are termed 'Southerlies.' The percentage contribution shows nearly equal occurrences of these directions, with 49% of winds from a southerly and 51% of winds in the easterly direction.

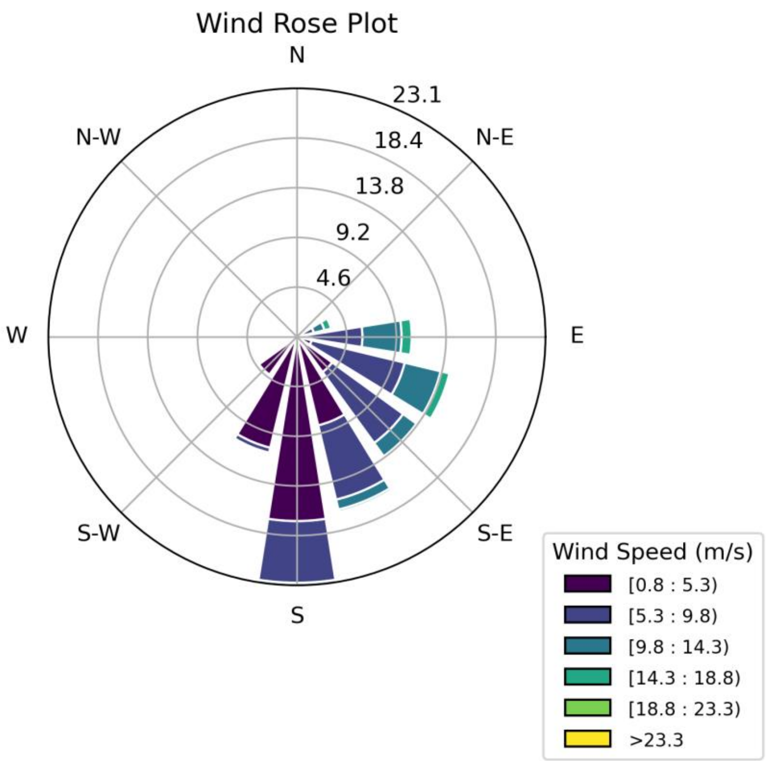

Figure 5.4: Wind rose showing wind speed and directions from the in-situ measurements at PE station for 2009 to 2019.

As in Figure 5.3, the contribution from easterly and southerly winds to annual SSH changes are considered separately for positive and negative SSH changes, as illustrated in Figure 5.5. During positive SSH days, there is a clear dominance of easterlies, and the contribution from southerly winds is limited. Similarly, southerlies show the maximum contribution to negative accumulation in surface snow. However, easterlies contribute ~30 to 40% during days of decreasing SSH, indicating strong easterlies can also remove surface snow during non-precipitating or low snowfall days. The importance of specific wind directions in the interannual variability of SSH was found to be weaker than the role of extreme conditions (EP, SW conditions) over the ice sheet. The annual mean contribution of extremes and different wind directions to SSH change is listed in Table 5.1, which gives a broad picture of the role of different meteorological factors in causing both positive and negative annual

SSH changes. Extreme conditions such as EP and SW days contribute significantly to the annual SSH change.

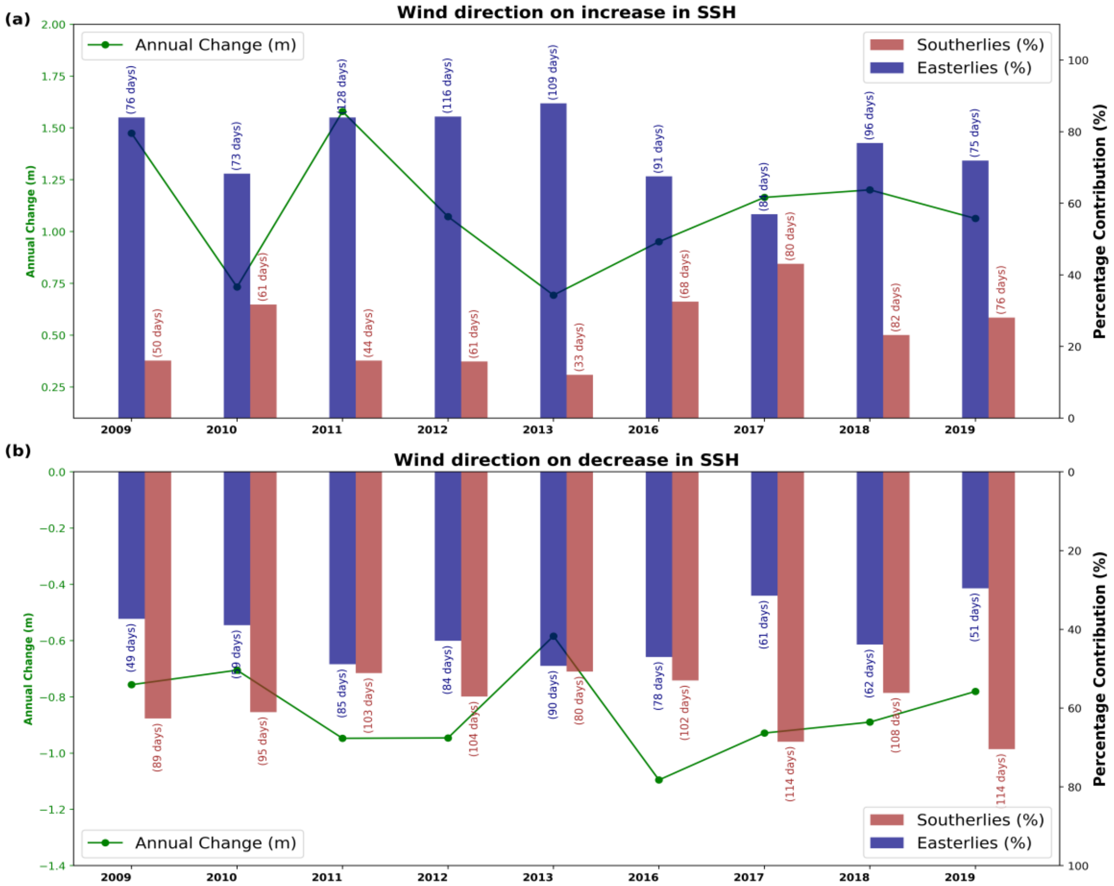

Figure 5.5: Interannual variability of annual SSH change (green) separately for (a) positive SSH and (b) negative SSH days. The contribution from the different wind directions, easterlies (red bar) and southerlies (blue bar), in total annual change, is given.

Most of the sudden SSH changes occurred during days with both EP and SW conditions, causing nearly 24.3% of positive changes in SSH within 16 days per year. These results specify that the major positive changes in SSH occur with heavy precipitation and strong winds occurring for fewer days. Also, SW-only events contribute to nearly 47.5% of annual SSH changes, considering both positive and negative SSH changes, with contributions around 22.7% and 24.8%, respectively. The mean number of days with SW-only events is slightly higher than EP and SW days, indicating slow but significant changes during these events in both increase and decrease in SSH. However, EP-only events occur less frequently and contribute in small proportions. Although EP and WS conditions occur for fewer days, they influence SSH changes significantly and contribute a major proportion to the annual change.

Annual Mean Values	Increase in SSH (Positive)	Decrease in SSH (Negative)
EP + SW	24.3% (16 days)	10.7% (13 days)
SW only	22.7% (28 days)	24.8% (38 days)
EP only	10.8% (7 days)	6.28% (6 days)
Easterlies	75.71%	41.04%
Southerlies	24.28%	58.96%

Table 5.1: Annual mean (averaged for 2009 to 2019) contributions from different extreme conditions (number of days of occurrence) and wind directions to the total positive and negative SSH changes.

As explained in the interannual variability analysis, the mean annual contribution shows the dominant role of two main wind directions in causing negative and positive changes in SSH. Overall, for positive SSH cases, easterly winds contribute 75.71%, and southerlies contribute a smaller proportion (24.28%). Similarly, for negative SSH, the dominant mean contribution is from southerly winds (~59%), and easterlies also cause ~41% of negative changes in SSH. So, winds with higher speed (> 11 m/s) from either direction can cause significant changes in SSH and redistribution of snow. The redistribution by wind can cause significant spatial and temporal variations in SSH, and these post-depositional factors are important over the regions of both complex and gentle orography (King et al., 2004).

5.1.2 Case studies of high-magnitude SSH change events

A detailed analysis of four cases with high-magnitude SSH changes was carried out with in-situ observation of surface meteorological variables from the PE station and reanalysis fields for spatial patterns. Figure 5.6 depicts the temporal analysis of selected cases of high SSH changes with observed surface variables, including daily and cumulative SSH change, wind direction, and 2-m temperature. Like Figure 5.2, the extreme conditions in precipitation and wind speed are marked, and the days with SSH change are shaded in Figure 5.6. The four events are taken according to the magnitude of SSH change and various meteorological regimes in which these events occurred. The four SSH change categories were (1) cold katabatic winds, (2) southerly warm winds, (3) highest precipitation events, and (4) easterly winds without precipitation. The spatial patterns of these events are illustrated in Figure 5.7 with contours of MSLP and wind vectors overlaid onto the spatial pattern of daily 2 m-temperature anomaly. This aids in understanding the large-scale and temporal changes during the event that caused changes in SSH.

5.1.2.1 Case 1 - cold katabatic winds

The first case is the common southerly wind scenario, where strong cold winds from the interior lead to changes in the SSH. Such an event occurred on 12 June 2017 and led to a positive change in SSH at the location of 0.128 m in a single day. The event occurred during a sudden cold outbreak of katabatic winds on 10 June, confirmed by the temporal changes in temperature and spatial pattern of temperature anomaly (Figures 5.7 and 5.8). Before the positive SSH day, there were two SW-only days on the 10 and 11 June, with wind speed peaks of up to 15 m s^{-1}. The wind was from the south, and there was a sharp dip in 2-m temperature from -24°C to -32°C, which indicated the strong influence of cold katabatic winds. The synoptic pattern confirmed the presence of a deep low-pressure system to the east of DML, which enhanced the flow from inland. The cold katabatic winds caused a temperature anomaly of -10°C over the coastal regions, especially towards the east of DML. The dry and strong katabatic winds from the plateau often remove surface snow, resulting in ablation at the surface. The SSH change due to this cold katabatic event marked the highest daily SSH change caused by wind-induced, non-precipitating conditions.

5.1.2.2 Case 2 - southerly winds

This was also a case with southerly winds, causing a significant negative change in SSH on 20 March 2012. This event was associated with a single SW-only day on 19 March, and the next day, the daily SSH change showed a decrease of -0.051 m in a single day. The winds were from the SSE with a speed of 13 m/s, and the synoptic pattern depicted the landfall of a mid-latitude cyclone to the west of DML. The southerly winds recorded on the east side of the cyclone showed a temperature rise before the event and recorded a 2-m temperature value of 17.5°C at the AWS. The cyclone's arrival induced a sudden southerly wind from inland, which reduced the SSH by ~0.05 m in a single day. The winds during this event were not katabatic, but they were still from the south direction, which was blowing clockwise under the influence of a small low-pressure system east of DML. This event shows the important role of SW-only events, especially southerly winds, in causing high-magnitude SSH changes without much precipitation.

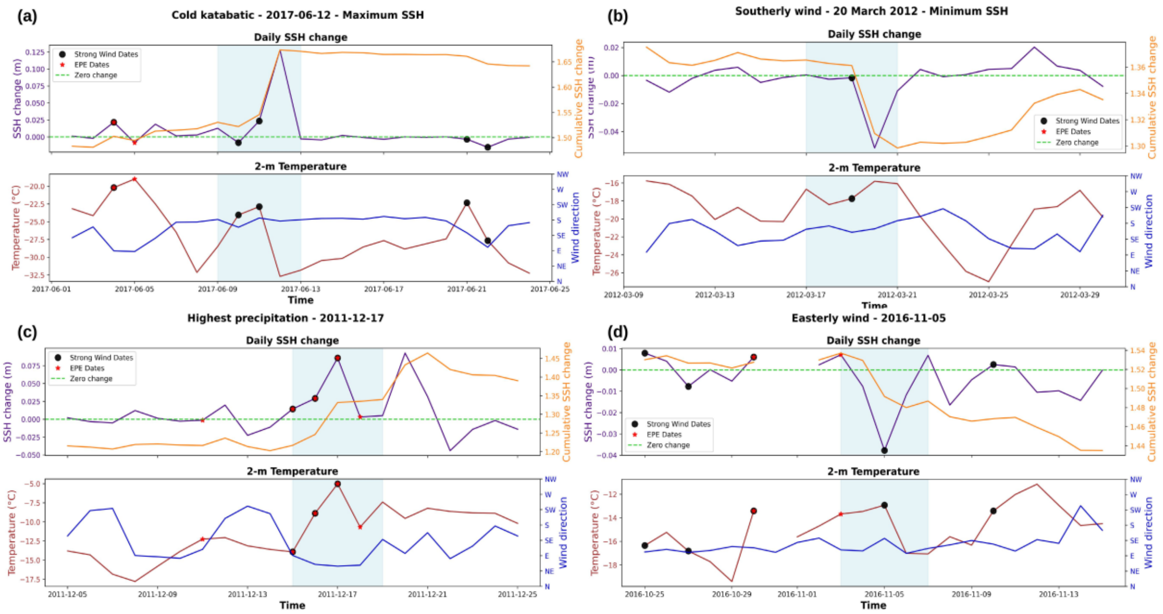

Figure 5.6: Temporal variability in meteorological variables and daily SSH values during selected case studies. (a) cold katabatic wind, b) southerly warm winds, c) highest precipitation event, and d) easterly winds. The extreme days and duration of the event are marked separately with markers and shading, respectively.

5.1.2.3 Case 3 – The largest precipitation event

The high-magnitude precipitation events are the primary cause of large, positive SSH changes, along with their intense winds. The sudden changes in daily SSH values are linked to combined EP and SW days. The selected event occurred for 3 days, from 15 to 17 December 2011, and marked the largest precipitation value of around 33 mm day^{-1} on 17 December. Surface height also increased over these 3 days, with a magnitude of 0.085 m on 17 December. The synoptic pattern indicated the landfall of a strong mid-latitude cyclone with intense E-NE winds over the PE station. Temperature increased from -15°C to -5°C, associated with the cyclone's landfall and warm air from lower latitudes. Synoptic observations confirm the typical pattern of an EPE event, with strong winds (~ 20 m s^{-1}) and elevated temperatures (~ +10°C change). This was a combined EP and SW event, with heavy snowfall related to cyclonic activity in the Southern Ocean. Snowfall in these events is contributed by moisture from the north, by the advection of warm airmasses to the location (Chapter 3). The combined EP and SW events are the primary atmospheric conditions causing sudden SSH changes in the measurements. Also, the change in SSH during the event continued over 15- 17 December with a total magnitude of +0.128 m of SSH.

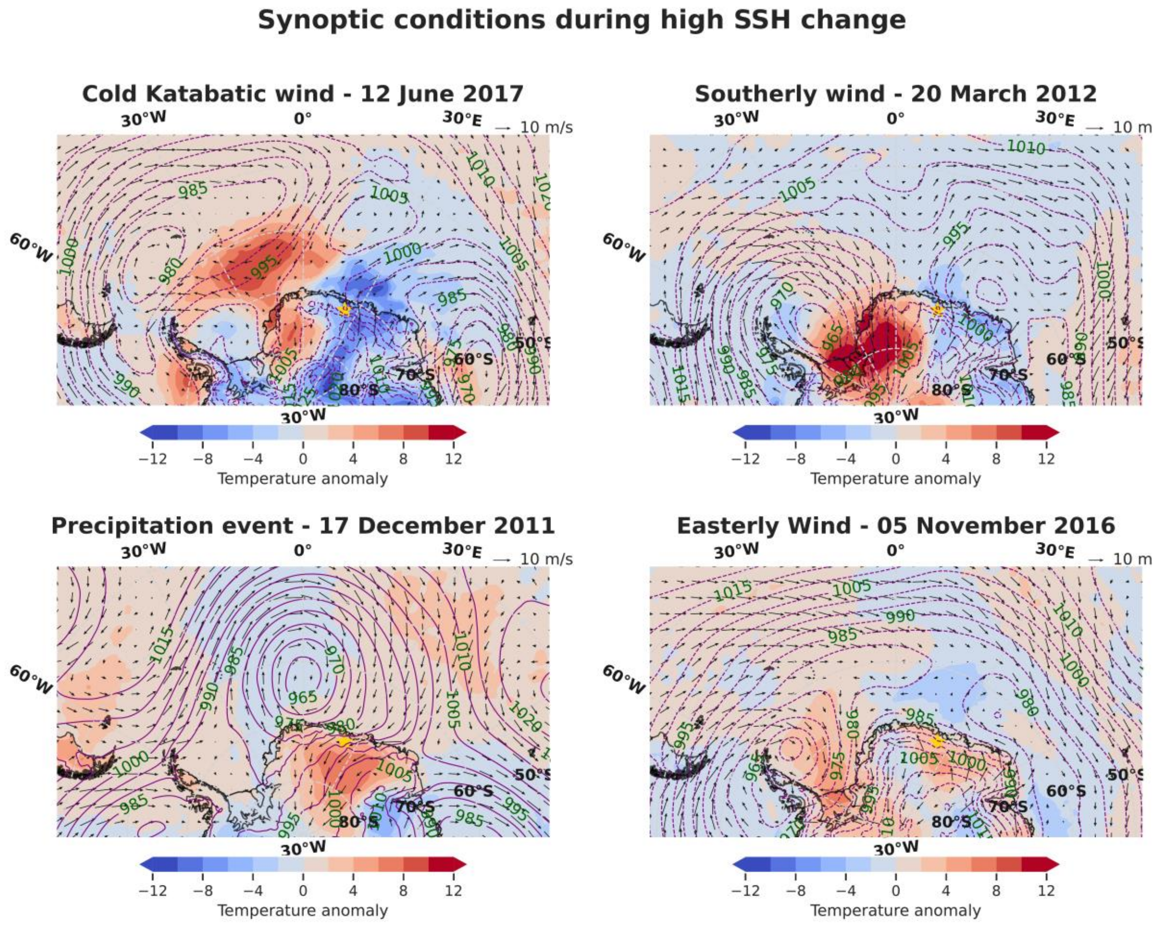

Figure 5.7: Similar to figure 5.7, but showing the synoptic pattern of MSLP (contours), 10-m wind vectors, and daily temperature anomalies during the event day of the selected cases are given.

5.1.2.4 Case 4 - easterly winds

Like southerly winds, winds from the east also cause high-magnitude SSH changes. This event occurred on 5 November 2016, when an easterly wind caused a change in SSH of -0.037 m. The event was associated with a single SW-only day blowing the surface snow away from the location. The presence of fresh precipitated snow due to an EP-only event on 3 November triggered snow blowing from the surface. The synoptic pattern indicates the presence of katabatic winds from the continental inland interior, turned to the left due to the Coriolis force and directed from the E-SE direction upon reaching the coastal region. The wind speed magnitude reached 15 m s^{-1} during the day of snow removal from the surface. The year 2016 also experienced a larger number of SW-only events and even contributed about 42% of the negative accumulation through these events.

5.1.2.5 Comparison with regional model SMB components

The SSH measurements from the height sensor capture net surface accumulation changes over the ice sheet. These SSH values correspond closely to the ice sheet's SMB, which indicates the net mass gain or loss at the surface. This section compares SMB data from two regional models, RACMO2.3p2 and MAR v3.11, over DML with in-situ SSH measurements at the PE station (Figure 5.8). Both models provide daily SMB values, and their daily variability during specific events is analyzed for comparison. Like the previous section, four cases were selected for this comparison: three events dominated by SW-only and one involving co-occurrence of both EP and SW, all causing significant SSH changes. Specific cases 1, 2, and 4 are wind-dominated events with cold katabatic, southerly, and easterly winds, respectively. The performance of the models during these wind-dominated events varied. Specifically, RACMO failed to represent wind-induced changes at the ice sheet surface, showing no significant changes during high-magnitude SSH events except during the highest precipitation event (case 3). However, the RACMO model accurately captured positive SMB changes during an EP-only event at the start of case 1 (on June 5, 2017), indicating its better performance in representing precipitation-induced SMB changes. Conversely, the MAR model displayed significant fluctuations in the SMB component related to changes in wind speed. However, compared with in situ SSH values, the MAR model performed poorly, overestimating the frequency of wind-induced changes.

The parameterization schemes for drifting snow effects in the MAR model trigger SMB changes whenever wind speeds fluctuate. Besides wind speed, surface snow changes are also influenced by the nature of snow particles, as freshly precipitated snow is more susceptible to drifting effects.

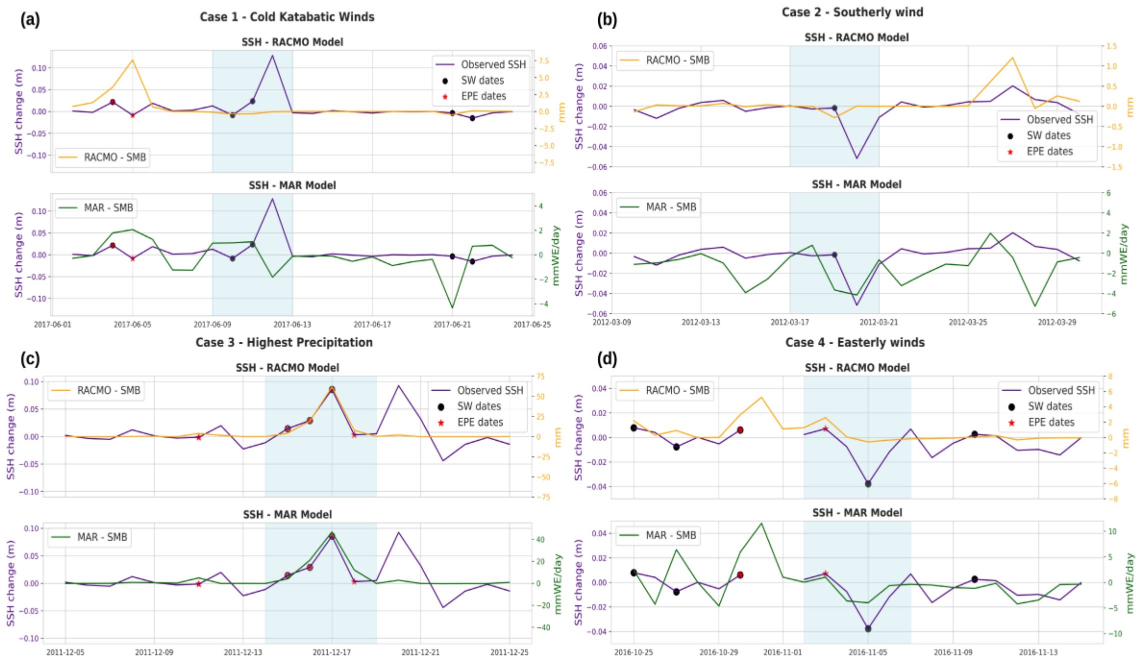

Figure 5.8: Temporal variability of SMB components from regional models and daily SSH values during selected case studies. (a) Cold katabatic wind, b) Southerly warm winds, c) Highest precipitation event, and d) Easterly winds. The extreme days and duration of the event are marked separately with markers and shading, respectively.

Both models effectively captured changes during case 3, the highest precipitation day, demonstrating their ability to represent surface changes during precipitation events. SSH measurements indicate that approximately 22-24% of changes occur during SW-only events, affecting both positive and negative SSH values. However, the regional models fail to accurately represent these changes in their surface components like SMB. Long-term analysis revealed similar model performance, especially concerning wind-induced SSH changes.

5.2 The role of extremes in ice core accumulation records

To interpret ice cores, it is essential to understand the different processes causing spatial and temporal variabilities in surface snow accumulation. The interannual changes in different proxies rely on these annual snow/ice accumulation values, ultimately reflected as past climate information derived from ice cores.

For a well-defined annual cycle of climate parameters, a steady year-round snow accumulation is important, which gives a steady sampling of different proxies of atmospheric chemistry and water vapor isotope composition (Noone et al., 1999). Also, the interpretation of the stable isotope in the ice core often uses the assumption of the climatological seasonally distributed precipitation; however, in reality, annual precipitation is dominated by a few days of intense precipitation (EPEs), especially over the coastal region. Also, these EPEs do not have a strong seasonal signal, and mostly, they occur throughout the year and are episodic (chapter 3). Along with that, days with strong winds favor significant snow redistribution and erosion, which often results in spatial and temporal variabilities in annual snow accumulation.

As explained in previous chapters, extreme conditions of EPEs and SWs occur over the ice sheets with different magnitudes and frequencies. This section investigates the influence of extreme conditions on the annually-dated ice core records by comparing the number of extreme events per year with the net accumulation values from each annual layer in the ice core. A few recent ice cores from coastal DML, with accumulation values available for 1979-2018, are considered for comparison with the number of extreme days (such as EPE and SW). The total annual number of EPEs and SW days for 1979-2018 was calculated from ERA5 reanalysis using the variables precipitation and 10-m wind speed values. The SW-days per year were calculated by removing the EPE dates from the data, which shows the number of non-precipitating, high wind-speed days each year. So, the number of SW days per year can be used as a proxy for the blowing or drifting snow effects over the ice sheet, as SW days show a clear signal of SSH changes associated with wind redistribution. Figure 5.9 depicts the annual accumulation record from ice cores for the two ice rises in DML, the Derwael ice rise and Hammarryggen ice rise, and their relation to interannual variability in the number of extremes. More details about the selected ice core locations and results are discussed below.

Derwael ice rise: The location (70.25°S, 26.34°E, elevation - 450 masl) is situated in coastal DML, where a 120 m long ice core was drilled in 2012 from the highest elevation point (Philippe et al., 2016). The ice rise has high variability in SMB, where high values are on the upwind side, as it acts as an orographic barrier to precipitating systems arriving from the ocean (Lenaerts et al., 2014). This core provided climate proxy for the past 250 years, covering 1759 to 2011. Also, the annual accumulation from this ice core demonstrated a large interannual variability, with an increasing trend in accumulation, especially for the last 50 years (1962 to 2011). This was the first coastal ice core from East Antarctica with such a trend in annual accumulation, which is due to changes in atmospheric circulation (Philippe et al., 2016). Comparison between the number of extreme precipitation days with annual ice core accumulation (mm) showed a close relationship (Figure 5.9 (a)). With a statistically significant ($p < 0.05$) positive correlation coefficient of 0.64, the number of EPE days shows a significant role in controlling the annual ice core accumulation. This implies that most of the snow accumulated during these years came from the high-magnitude snowfall events. The high accumulation in the years 1988, 1996, 2001, 2009, and 2011 is well-matched with the number of EPEs during these years and the presence of anomalous snowfall from a few ARs during the years 2009 and 2011. The correlation between the annual precipitation and ice core accumulation is 0.71, implying that precipitation is the main input for the net ice core accumulation and similarly, the number of EPEs has a significant role in annual accumulation.

However, there was no significant correlation between accumulation and the number of SW-only days at this location. But in 1992, when there were fewer days with EPEs, the year exhibited a high annual accumulation, likely influenced by numerous SW days that likely transported snow to the area in strong wind conditions. While winds also contribute to ice core accumulation, EPEs notably impact the overall accumulation at this location.

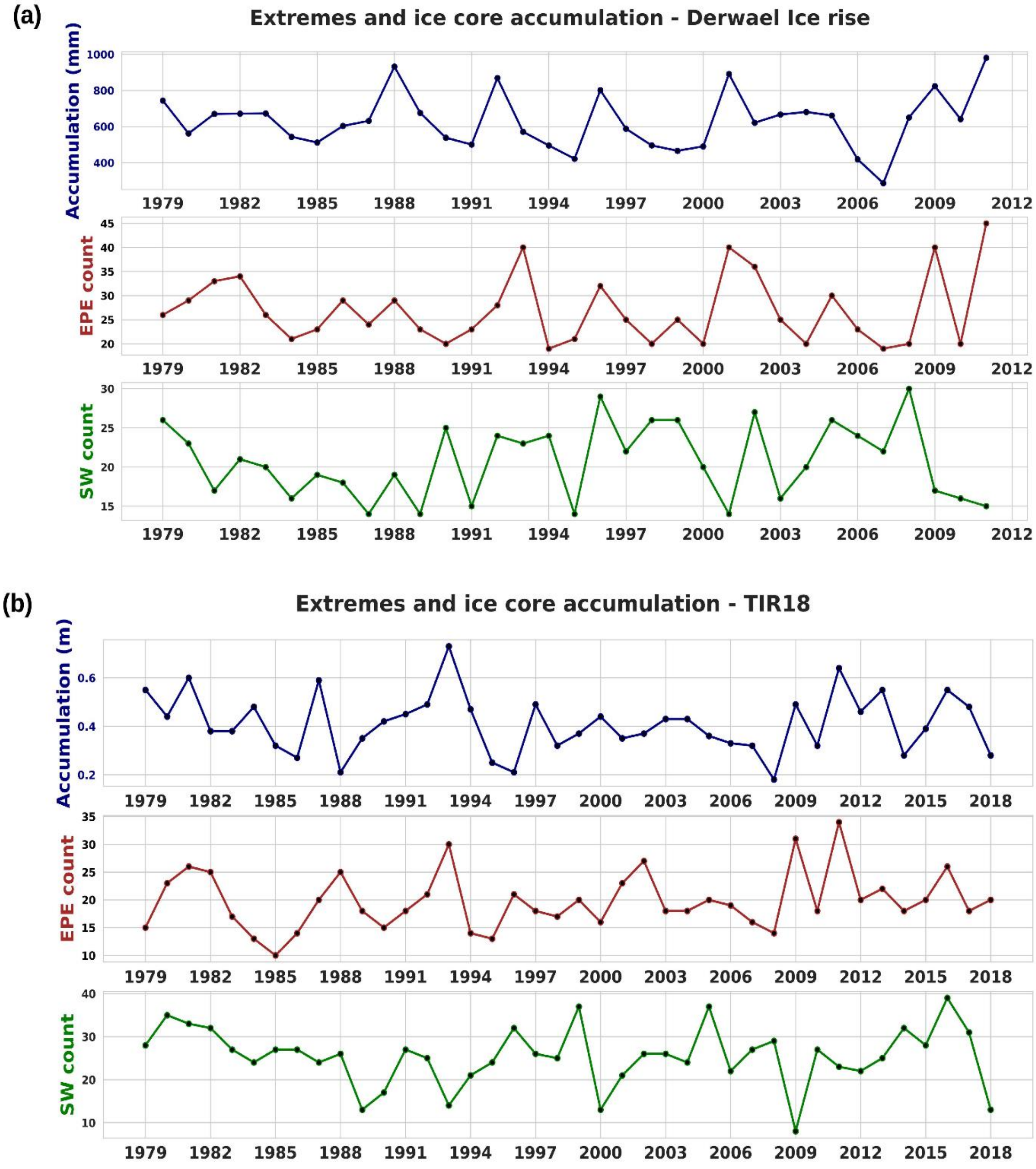

Figure 5.9: Comparison of the ice core annual accumulation and the total annual number of EPEs and SWs from (a) Derwael ice rise and (b) Hammarryggen ice rise (TIR18) for the period with the availability of both ice core records and reanalysis data.

TIR18: This 206 m ice core was drilled from the highest point of Hammarryggen ice rise (70.4996°S, 21.88°E, elevation - 348 masl) during the summer of 2018/19. This ice core covers the period 1780 to 2018 with annually-dated accumulation (m), paleo proxies such as sea salts, and water vapor components (Wauthy et al., 2024). Like the Derwael ice rise location, there was high accumulation on the windward side of the ice rise, as it perturbs moisture pathways from the ocean and induces orographic snowfall events. Thus, the comparison between annual ice core accumulation and the number of EPEs shows a significant ($p<0.05$) positive correlation of 0.46 (Figure 5.9 (b)). Especially for the years - 1993, 2009, and 2011, the high ice core accumulation was associated with a higher number of EPE days. The number of SW-only days is also less for these years, which promoted high annual accumulation without many ablation events due to strong winds. During 1988, there were 25 EPE days, but very low values of ice core accumulation, which was related to a high number of SW-only days. In 1988, the strong winds throughout the year removed much of the snow precipitated, resulting in low ice core accumulation. Similarly, 1996 had low ice core accumulation due to many SW-only days. This indicates the role of both EPEs and SWs in making significant changes in annual ice core accumulation.

FB9817: This ice core location is situated inland of DML at 75°S, 6.5°W, in the high-altitude ice sheet with an elevation of 2,680 masl. The ice core record covers nearly 200 years, from 1800 to 1997 (Oerter et al., 2000). A comparison of extreme events and ice core accumulation is illustrated in Figure 5.10 (a). The ice core annual accumulation shows a significant negative correlation with SW-only days, indicating the importance of the winds in influencing the accumulation at this location. Although the magnitude of precipitation and frequency of events are very limited over inland DML locations (Chapter 3), the winds have an important role in shaping annual ice core accumulation. With a correlation coefficient of -0.46, the analysis indicated that the SW-only days significantly contributed to removing the surface snow from the ice sheet. In the years 1982 and 1990, many SW-only days (~ 35 days) contributed to less annual ice core accumulation. Vice versa, in 1983 and 1989, a low number of SW-only (~ 10 to 14 days) days helped maintain the precipitated snow in the ground. Thus, there was a high accumulation in ice core annual layers.

a)

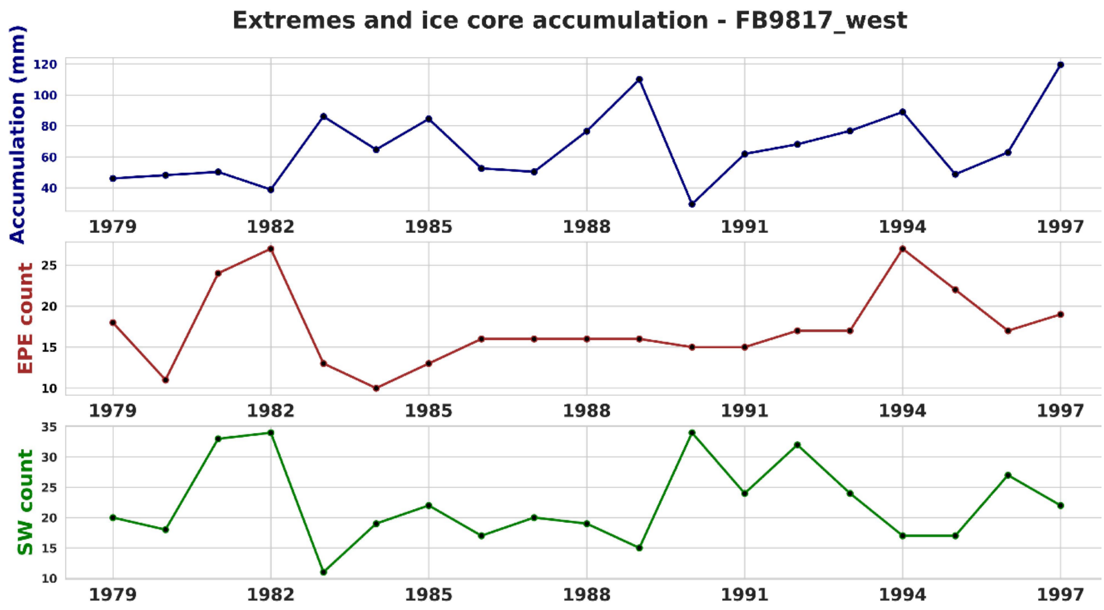

)

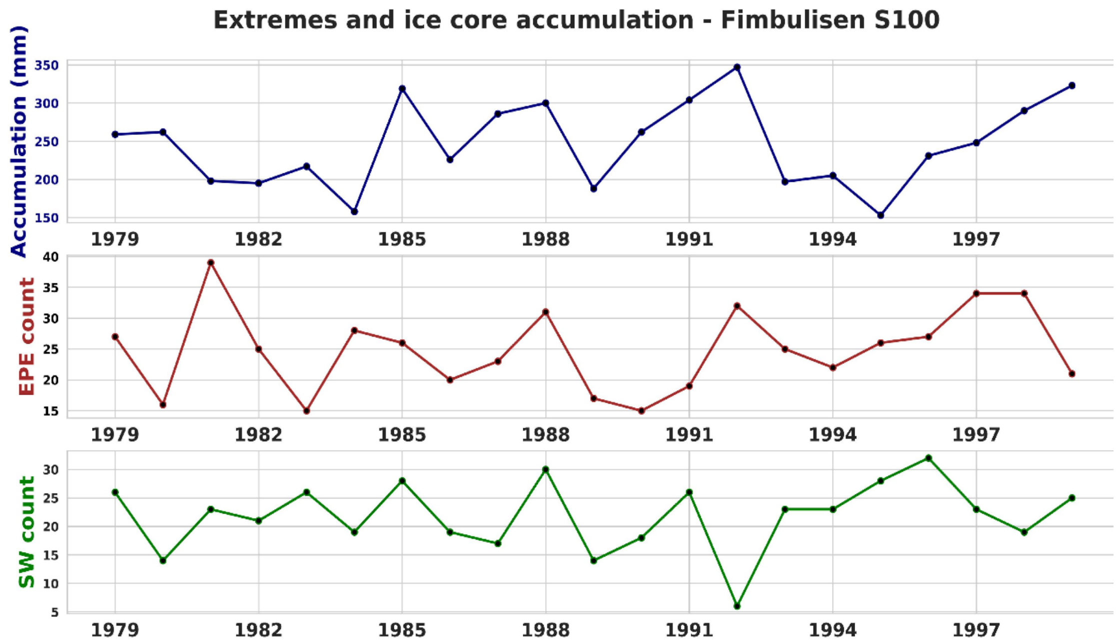

Figure 5.10: Similar to figure 5.9, but for (a) FB9817 ice core and (b) Fimbulisen S100 for the period with the availability of both ice core records and reanalysis data

Fimbulisen S100: Fimbulisen S100 is a near-coastal ice core location at 70.24°S, 4.8°E and at a low-elevation area of 48 masl with annual dating covering 1737 to 1999

(Kaczmarska et al., 2006). There was no significant relationship between the number of extremes and ice core accumulation at this location, but the temporal analysis indicated the different scenarios in which extreme events influenced the ice core accumulation (Figure 5.10 (b)). Firstly, many EPE days contributed to high annual ice core accumulation during 1985, 1988, 1992, and 1997, where more precipitation acted as an input to the annual accumulation. Secondly, a high number of SW-only days, but a small number of EPE days in 1983 and 1991 contributed to high annual accumulation, where wind-induced positive accumulation occurred due to snow blowing to the location. Finally, during 1995, the number of EPE was high, but annual accumulation had low values, which was due to the presence of many SW-only days (~ 30 days), where the wind blew away most of the snow from the surface. Since this location was low-lying and situated very close to the ocean, both precipitation and winds together impacted the spatial and temporal surface snow accumulation and will be reflected in annual layers in the ice cores. Even though precipitation acts as a primary input factor in ice core accumulation, winds contribute in both ways, with an increase and decrease in net accumulation by blowing in and out the surface snow.

The comparison of snow accumulation data of selected ice core locations from coastal and inland locations of DML indicated the significant role of extreme meteorological conditions in shaping the annual accumulation values in ice core records. The number of EPEs per year mostly controls the interannual variability in annual accumulation and years with high accumulation. This implies that the large amount of snow in these annual layers is precipitated from these short-living, episodic EPEs. The highest positive correlation values were found for the ice cores drilled at the ice rise locations (like Derwael and Hammarryggen), which are prone to orographic snowfall events. SW-only days also have a distinct role in shaping the annual layer in the ice core, although they do not have a significant relationship with annual accumulation in most ice cores. The snow blowing onto or out of the location is strongly related to the number of SW-only days each year, and these can be used as a proxy for wind-induced snow redistribution over the ice sheet. Compared to the coastal regions, inland ice core locations are mostly affected by SW-only conditions (like FB9817), with a significant contribution from strong cold katabatic southerly winds blowing over the region. Overall, there are different scenarios in which extremes control the ice core's annual accumulation. Primarily, a high number of EPEs contribute to high ice core accumulation, where episodic high-magnitude precipitation systems deposit a large amount of snow at the drilling location. The other scenarios are related to high SW-only days, where more non-precipitating, high wind days blow away the surface snow, causing decreased snow accumulation. Lastly, the number of SW-only days blowing snow from different regions into the ice core location, resulting in high annual accumulation even without a high number of weather systems precipitating at the site.

5.3 Conclusions

This chapter carried out an analysis of the influence of extreme meteorological conditions in controlling surface snow height changes and, implicitly, annual snow accumulations in ice cores from the DML region. High-resolution SSH measurements from the PE station are used to demonstrate the role of extreme atmospheric conditions in changing surface accumulation. The study assessed the influence of extreme meteorological conditions on daily mean SSH changes. Also, it quantified their annual contribution as these extreme conditions were found to be major factors controlling the sudden, episodic changes in SSH. PE station had positive accumulation, where input was greater than ablation, with a cumulative snow height change of 2.26 m. The analysis revealed that sudden SSH changes were primarily driven by extreme precipitation (EP) and strong winds (SW) conditions. EP, SW, and combined EP & SW events contribute to increased and decreased SSH, exhibiting high interannual variability. The frequency and duration of these events (combined EP and SW) were predominant in causing positive SSH changes, where in some years, more than 50% of changes occurred in fewer EP and SW days. Negative changes in SSH were mainly controlled by SW-only days, where winds caused significant redistribution. Certain wind directions, especially easterlies and southerlies, can also impact the positive and negative changes in SSH, where easterlies dominate during accumulation and southerlies during ablation events. However, the large interannual variability in SSH is controlled by extreme conditions, particularly combined EP and SW days on positive accumulation and SW-only days on negative accumulation days. Notably, days with co-occurring EP and SW conditions account for 24.3% of positive SSH changes within 16 days year^{-1}. Case studies of high-magnitude SSH change days highlight the significant impact of strong southerly or easterly winds on SSH, even without substantial precipitation. However, the regional models fail to capture these wind-induced changes over ice sheets in their output of surface parameters, and this signifies the need for better drifting and blowing snow parameterizations in models. Results from this chapter are limited to one location over the ice sheet, but a similar effect of extreme meteorological conditions can be expected in shaping surface snow accumulation at different parts of the Antarctic ice sheet.

Considering the significant influence of extreme conditions in precipitation and surface winds in causing a major fraction of surface snow height changes, this study identified the signals of these events in annual ice core accumulations of ice cores drilled from different parts of DML. The number of EPEs per year was found to be closely related to the annual accumulation rates at ice cores drilled from a number of ice rise locations over DML. The ice core annual accumulation showed a significant positive correlation with the number of high precipitation events, which indicated that the orographically-induced snowfall events, which are intermittent and intense over the years, are primarily contributing to the annual snow accumulations in these ice cores. The major control of EPEs in annual accumulation can disrupt the seasonal pattern in ice cores making the seasonal accumulation biased toward particular months or days of heavy precipitation. Results also show that the number of SW-only days can influence the annual ice core accumulation, basically by blowing snow in and out of the ice core locations. Especially for inland cores, where strong katabatic winds often dominate over snowfall events, the surface snow gets re-deposited to far locations, leading to ablation events in these regions. Overall, from these analyses, it is demonstrated the significant role of these short-living, intense, and randomly occurring extreme atmospheric conditions in shaping the major portion of annual ice core accumulation. In addition to such biases introduced by EPEs, various other stratigraphic noises could also complicate the relationship between the ice core record and local climate (Jackson et al., 2022; Mahalinganathan et al., 2022). Therefore, a careful examination of various factors, including the role of EPEs, is critically important while interpreting ice core records from coastal Antarctica.

Chapter 6

Summary and Future Perspectives

This study has explored extreme precipitation events (EPEs) over Dronning Maud Land (DML) and their impact on ice-core-based climate records from this region. EPEs are episodic and intense, resulting in significant precipitation over a short period. These events are pivotal in determining the annual total precipitation in Antarctica, particularly in coastal regions with complex orography. Ice cores serve as natural archives of past climate variability and use various proxies to record data from sub-annual to glacial-interglacial periods. However, this study demonstrates that the episodic nature of EPEs and the accompanying meteorological conditions can introduce significant biases into the annual ice core records by disproportionately affecting annual accumulations.

This is the first comprehensive investigation into the influence of EPEs on ice core records by integrating multiple data sources and methods. These include reanalysis data, regional models, satellite imagery, in-situ observations, and ice core records from the DML region. Through climatological analysis, annual variability studies, and case studies using high-resolution models, the meteorological context of these EPEs over the study area was examined. The key findings of this thesis are summarized in the following sections.

6.1 Spatial and temporal variability of EPEs and their controlling factors

The EPEs are characterized by large daily precipitation values that exceed high percentile thresholds. A climatological analysis of EPEs over 1979-2018 reveals that their spatial distribution in DML was highly variable and influenced by the complex coastal orography. The windward sides of orographic barriers frequently experienced the highest precipitation. During these events, surface meteorological variables, such as surface winds, are stronger and more consistent in direction, often triggering blowing snow. Surface temperatures during EPEs had large positive anomalies, indicating warm-air advection from lower latitudes, which can introduce a warm bias in stable isotope records in ice cores.

Temporal analysis shows that 40-60% of the annual precipitation occurs in just 10-15 EPE days, potentially skewing the annual layers in ice cores towards these events. The synoptic structure during EPEs typically features a dipole of a low-pressure cyclone to the west and a high-pressure anticyclone to the east, located north of DML. The occurrence of blocking anticyclones to the northeast of DML significantly controls interannual variability. There has been a notable increasing trend in EPEs over DML, driven by enhanced moisture transport from the South Atlantic through poleward winds and atmospheric rivers (ARs). Over 40% of EPEs at ice core sites are associated with ARs, highlighting the significance of low-latitude moisture sources. Thus, the meteorological conditions during EPEs, their frequency, increasing trend, moisture sources, and post-depositional effects due to strong winds are crucial considerations for selecting ice core records from the coastal regions.

6.2 Case study of an EPE event using a high-resolution regional model

A detailed examination of an EPE event using reanalysis data and a high horizontal resolution model revealed the extreme atmospheric conditions that triggered intense EPEs over DML. This significant precipitation event was associated with an intense AR from 30°S - 40°S in the South Atlantic. The atmosphere had a blocking anticyclone of record strength to the east and a strong mid-latitude cyclone to the west of the precipitation area. The sudden intensification of the mid-latitude cyclone was driven by meridional jet streaks in the upper atmosphere, causing the cyclone to make landfall over DML. Moisture uptake occurred in the South Atlantic, with moisture transported through the cyclone's eastern flank. The interaction between the warm airmass from lower latitudes and the cold airmass from Antarctica's interior led to a frontal boundary where a frontal occlusion developed.

Regional model output highlighted the significant role of the complex coastal orography in the spatial distribution of precipitation. Orographic lift of warm, moist air by these features resulted in regional maxima and minima in precipitation, particularly on the windward side. Elevated temperatures during the event were associated with the advection of warm airmasses. Thus, Antarctic snow accumulation hinges on complex mechanisms involving large-scale circulation, precipitation microphysics, local wind patterns, intense moisture transport, and the nature of local topography.

6.3 Influence of extreme meteorological conditions on annual ice core records

In-situ measurements of surface snow height (SSH) and meteorological parameters at Princess Elisabeth station in DML were analysed to assess the impact of extreme weather conditions on SSH. Extreme precipitation (EP) and strong wind (SW) were identified as critical factors causing changes in SSH, with days experiencing both EP and SW showing sudden, episodic changes. Even SW-only days, without significant precipitation, contributed to positive changes in surface height. However, winds predominantly caused negative changes in SSH by drifting or blowing snow. Easterly winds, common during precipitation events, typically increased snow height, while southerly winds, including strong katabatic winds, were major contributors to negative SSH changes. In general, strong winds from any direction could blow snow in or out of the location. Case studies of significant SSH changes also highlighted the dominant role of SW-only days in causing substantial surface height variations. However, regional models struggled to capture these wind-induced changes in surface mass balance components, underscoring the need for improved drifting snow parameterizations. These wind-induced processes are crucial over the ice sheet surface and local conditions, potentially affecting the accumulation values in ice cores. Thus, the combination of spatial variability in snowfall and wind-driven snow redistribution explains a large part of surface accumulation variability.

This study demonstrated that extreme precipitation and strong wind conditions significantly impact ice core annual accumulations, showing a strong correlation between the number of EPEs per year and the annual accumulations. This correlation is particularly high for cores from ice-rise locations, frequently affected by orographically influenced snowfall in the near-coastal regions. In these coastal areas, ice cores drilled even a short distance apart can exhibit very different temporal trends in annual accumulations, highlighting the complexities in interpreting climate records from these cores. These complexities raise questions about the spatial and temporal representativeness of ice cores from coastal regions. In inland areas, snow removal by wind redistribution, particularly on SW-only days, also impacts snow accumulation, further complicating the reconstruction of paleoclimate records. Wind-driven processes and episodic high-magnitude precipitation events can introduce biases into these records, underscoring the importance of careful site selection to minimize the impact of blowing snow. Stratigraphic noises and factors, such as sublimation and melting, also affect annual snow accumulation records. Still, extreme conditions dominate to influence the paleoclimate signals in ice cores, which may reflect intense, episodic events rather than average conditions.

Direct comparisons of annual extremes with ice core accumulation are only reliable for well-dated cores, as dating errors of one or two years are common. Moreover, short-duration extreme events may not be easily detectable in annually dated cores. However, the total number of events per year can still offer valuable insights into the accumulation mechanisms.

This study exploring the impact of meteorological extremes on paleoclimate signals in Antarctic ice cores offers important insights for the ice core research community. The key recommendations include:

1. Ice core site selection should account for the influence of EPEs and snow transport processes. Coastal ice rises, often chosen for their high accumulation and temporal resolution, are heavily affected by EPEs and strong wind, leading to significant snow transport. Ideal locations should have minimal snow redistribution, ensuring freshly fallen snow remains relatively undisturbed. A detailed assessment of meteorological conditions, particularly horizontal snow transport, is essential before drilling ice cores.
2. The frequency and intensity of EPEs in the site must be considered when interpreting ice-core data, as these events can distort annual climate signals by elevated temperatures and large accumulations. Moisture transported from northern sources through ARs may introduce subtropical signals, further complicating data interpretation. A thorough understanding of EPEs, ARs, and the meteorological processes influencing precipitation in Antarctica is critical for improving the accuracy of ice-core-derived climate records.

6.4 Future perspectives

Extreme weather events are intermittent but highly impactful over the Antarctic ice sheet. With each degree of Celsius of atmospheric warming, a 7% increase in moisture content is projected for the lower layers of the atmosphere (Douville et al., 2021). This moisture increase will be accompanied by intensified wind-driven water transport, particularly towards convergent zones of atmospheric circulation, including high latitudes. Consequently, an increase in the frequency and intensity of extreme events on the Antarctic continent is anticipated (Seneviratne et al., 2021). Long-range transport of warmer tropical moisture to coastal Antarctica could lead to a shift towards rainfall events and could cause significant melting over the coastal ice sheet and ice shelves. Therefore, more in-depth analyses of precipitation extremes in Antarctica are essential to enhance our understanding of how these areas will respond to potential future global climate changes. Focused investigations of future occurrences of these extreme events using climate model simulations under different greenhouse gas emission scenarios and ozone hole recovery will give insight into possible future changes and options for mitigation plans for the ice sheets of Antarctica.

Further, it is important to have advanced observational campaigns that collect a full set of in-situ data along with reanalysis data, and regional model simulations to gain further knowledge of the relationship between meteorological parameters and snow accumulation as depicted in ice cores. This will quantify the changes in annual accumulations from the whole range of meteorological conditions, including extremes. This approach will also identify the dominance of multiple extreme events in each annual layer of ice core and their signals in different ice core proxies.

Bibliography

Adusumilli, S., A. Fish, M., Fricker, H. A., & Medley, B. (2021). Atmospheric River Precipitation Contributed to Rapid Increases in Surface Height of the West Antarctic Ice Sheet in 2019. *Geophysical Research Letters*, *48*(5), e2020GL091076. https://doi.org/10.1029/2020GL091076

Agosta, C., Amory, C., Kittel, C., Orsi, A., Favier, V., Gallée, H., van den Broeke, M. R., Lenaerts, J. T. M., van Wessem, J. M., van de Berg, W. J., & Fettweis, X. (2019). Estimation of the Antarctic surface mass balance using the regional climate model MAR (1979–2015) and identification of dominant processes. *The Cryosphere*, *13*(1), 281–296. https://doi.org/10.5194/tc-13-281-2019

Amory, C., Kittel, C., Le Toumelin, L., Agosta, C., Delhasse, A., Favier, V., & Fettweis, X. (2021). Performance of MAR (v3.11) in simulating the drifting-snow climate and surface mass balance of Adélie Land, East Antarctica. *Geoscientific Model Development*, *14*(6), 3487–3510. https://doi.org/10.5194/gmd-14-3487-2021

Baiman, R., Winters, A. C., Lenaerts, J., & Shields, C. A. (2023). Synoptic Drivers of Atmospheric River Induced Precipitation Near Dronning Maud Land, Antarctica. *Journal of Geophysical Research: Atmospheres*, *128*(7), e2022JD037859. https://doi.org/10.1029/2022JD037859

Bamber, J. L., Riva, R. E. M., Vermeersen, B. L. A., & LeBrocq, A. M. (2009). Reassessment of the Potential Sea-Level Rise from a Collapse of the West Antarctic Ice Sheet. *Science*, *324*(5929), 901–903. https://doi.org/10.1126/science.1169335

Bintanja, R., & Oerlemans, J. (1995). The influence of the albedo-temperature feed-back on climate sensitivity. *Annals of Glaciology*, *21*, 353–360. https://doi.org/10.3189/S0260305500016062

Bintanja, R., & Reijmer, C. H. (2001). A simple parameterization for snowdrift sublimation over Antarctic snow surfaces. *Journal of Geophysical Research: Atmospheres*, *106*(D23), 31739–31748. https://doi.org/10.1029/2000JD000107

Birnbaum, G., Brauner, R., & Ries, H. (2006). Synoptic situations causing high precipitation rates on the Antarctic plateau: Observations from Kohnen Station, Dronning Maud Land. *Antarctic Science*, *18*(2), 279–288. https://doi.org/10.1017/S0954102006000320

Blanchard-Wrigglesworth, E., Cox, T., Espinosa, Z. I., & Donohoe, A. (2023). The Largest Ever Recorded Heatwave—Characteristics and Attribution of the Antarctic

Heatwave of March 2022. *Geophysical Research Letters*, *50*(17), e2023GL104910. https://doi.org/10.1029/2023GL104910

Boening, C., Lebsock, M., Landerer, F., & Stephens, G. (2012). Snowfall-driven mass change on the East Antarctic ice sheet. *Geophysical Research Letters*, *39*(21). https://doi.org/10.1029/2012GL053316

Bozkurt, D., Rondanelli, R., Marín, J. C., & Garreaud, R. (2018). Foehn Event Triggered by an Atmospheric River Underlies Record-Setting Temperature Along Continental Antarctica. *Journal of Geophysical Research: Atmospheres*, *123*(8), 3871–3892. https://doi.org/10.1002/2017JD027796

Braaten, D. A. (1997). A detailed assessment of snow accumulation in katabatic wind areas on the Ross Ice Shelf, Antarctica. *Journal of Geophysical Research: Atmospheres*, *102*(D25), 30047–30058. https://doi.org/10.1029/97JD02337

Braaten, D. A. (2000). Direct measurements of episodic snow accumulation on the Antarctic polar plateau. *Journal of Geophysical Research: Atmospheres*, *105*(D8), 10119–10128. https://doi.org/10.1029/2000JD900099

Broeke, M. R. van den, Winther, J.-G., Isaksson, E., Pinglot, J. F., Karlöf, L., Eiken, T., & Conrads, L. (1999). Climate variables along a traverse line in Dronning Maud Land, East Antarctica. *Journal of Glaciology*, *45*(150), 295–302. https://doi.org/10.3189/S0022143000001799

Bromwich, D. H. (1988). Snowfall in high southern latitudes. *Reviews of Geophysics*, *26*(1), 149–168. https://doi.org/10.1029/RG026i001p00149

Bromwich, D. H. (1989). An Extraordinary Katabatic Wind Regime at Terra Nova Bay, Antarctica. *Monthly Weather Review*, *117*(3), 688–695. https://doi.org/10.1175/1520-0493(1989)117<0688:AEKWRA>2.0.CO;2

Bromwich, D. H., Guo, Z., Bai, L., & Chen, Q. (2004). Modeled Antarctic Precipitation. Part I: Spatial and Temporal Variability. *Journal of Climate*, *17*(3), 427–447. https://doi.org/10.1175/1520-0442(2004)017<0427:MAPPIS>2.0.CO;2

Bromwich, D. H., Nicolas, J. P., & Monaghan, A. J. (2011). An Assessment of Precipitation Changes over Antarctica and the Southern Ocean since 1989 in Contemporary Global Reanalyses. *Journal of Climate*, *24*(16), 4189–4209. https://doi.org/10.1175/2011JCLI4074.1

Bromwich, D. H., Otieno, F. O., Hines, K. M., Manning, K. W., & Shilo, E. (2013). Comprehensive evaluation of polar weather research and forecasting model performance in the Antarctic. *Journal of Geophysical Research: Atmospheres*, *118*(2), 274–292. https://doi.org/10.1029/2012JD018139

Carrasco, J. F., Bromwich, D. H., & Monaghan, A. J. (2003). Distribution and Characteristics of Mesoscale Cyclones in the Antarctic: Ross Sea Eastward to the Weddell Sea. *Monthly Weather Review*, *131*(2), 289–301. https://doi.org/10.1175/1520-0493(2003)131<0289:DACOMC>2.0.CO;2

Casado, M., Landais, A., Picard, G., Münch, T., Laepple, T., Stenni, B., Dreossi, G., Ekaykin, A., Arnaud, L., Genthon, C., Touzeau, A., Masson-Delmotte, V., & Jouzel, J. (2018). Archival processes of the water stable isotope signal in East Antarctic ice cores. *The Cryosphere*, *12*(5), 1745–1766. https://doi.org/10.5194/tc-12-1745-2018

Cassano, E. N., Glisan, J. M., Cassano, J. J., Jr, W. J. G., & Seefeldt, M. W. (2015). Self-organizing map analysis of widespread temperature extremes in Alaska and Canada. *Climate Research*, *62*(3), 199–218. https://doi.org/10.3354/cr01274

Cook, A. J., Fox, A. J., Vaughan, D. G., & Ferrigno, J. G. (2005). Retreating Glacier Fronts on the Antarctic Peninsula over the Past Half-Century. *Science*, *308*(5721), 541–544. https://doi.org/10.1126/science.1104235

Danielson, J. J., & Gesch, D. B. (n.d.). *Global Multi-resolution Terrain Elevation Data 2010 (GMTED2010)*.

Dansgaard, W. (1964). Stable isotopes in precipitation. *Tellus*, *16*(4), 436–468. https://doi.org/10.3402/tellusa.v16i4.8993

Davis, C. H., Li, Y., McConnell, J. R., Frey, M. M., & Hanna, E. (2005). Snowfall-Driven Growth in East Antarctic Ice Sheet Mitigates Recent Sea-Level Rise. *Science*, *308*(5730), 1898–1901. https://doi.org/10.1126/science.1110662

Deb, P., Orr, A., Bromwich, D. H., Nicolas, J. P., Turner, J., & Hosking, J. S. (2018). Summer Drivers of Atmospheric Variability Affecting Ice Shelf Thinning in the Amundsen Sea Embayment, West Antarctica. *Geophysical Research Letters*, *45*(9), 4124–4133. https://doi.org/10.1029/2018GL077092

Deb, P., Orr, A., Hosking, J. S., Phillips, T., Turner, J., Bannister, D., Pope, J. O., & Colwell, S. (2016). An assessment of the Polar Weather Research and Forecasting (WRF) model representation of near-surface meteorological variables over West Antarctica. *Journal of Geophysical Research: Atmospheres*, *121*(4), 1532–1548. https://doi.org/10.1002/2015JD024037

Dee, D. P., Uppala, S. M., Simmons, A. J., Berrisford, P., Poli, P., Kobayashi, S., Andrae, U., Balmaseda, M. A., Balsamo, G., Bauer, P., Bechtold, P., Beljaars, A. C. M., van de Berg, L., Bidlot, J., Bormann, N., Delsol, C., Dragani, R., Fuentes, M., Geer, A. J., … Vitart, F. (2011). The ERA-Interim reanalysis: Configuration and performance of the data assimilation system. *Quarterly Journal of the Royal Meteorological Society*, *137*(656), 553–597. https://doi.org/10.1002/qj.828

Delaygue, G., Jouzel, J., Masson, V., Koster, R. D., & Bard, E. (2000). Validity of the isotopic thermometer in central Antarctica: Limited impact of glacial precipitation seasonality and moisture origin. *Geophysical Research Letters*, *27*(17), 2677–2680. https://doi.org/10.1029/2000GL011530

Dey, R., Thamban, M., Laluraj, C. M., Mahalinganathan, K., Redkar, B. L., Kumar, S., & Matsuoka, K. (2023). Application of visual stratigraphy from line-scan images to constrain chronology and melt features of a firn core from coastal Antarctica. *Journal of Glaciology*, *69*(273), 179–190. https://doi.org/10.1017/jog.2022.59

Doswell, C. A., Brooks, H. E., & Maddox, R. A. (1996). Flash Flood Forecasting: An Ingredients-Based Methodology. *Weather and Forecasting*, *11*(4), 560–581. https://doi.org/10.1175/1520-0434(1996)011<0560:FFFAIB>2.0.CO;2

Doswell, C. A., Ramis, C., Romero, R., & Alonso, S. (1998). A Diagnostic Study of Three Heavy Precipitation Episodes in the Western Mediterranean Region. *Weather and Forecasting*, *13*(1), 102–124. https://doi.org/10.1175/1520-0434(1998)013<0102:ADSOTH>2.0.CO;2

Douville, H., Raghavan, K., Renwick, J. A., Allan, R. P., Arias, P. A., Barlow, M., Cerezo Mota, R., Cherchi, A., Gan, T. Y., Gergis, J., Jiang, D., Khan, A., Pokam Mba, W., Rosenfeld, D., Tierney, J., & Zolina, O. (2021). Water cycle changes. In V. Masson-Delmotte, P. Zhai, A. Pirani, S. L. Connors, C. Péan, S. Berger, N. Caud, Y. Chen, L. Goldfarb, M. I. Gomis, M. Huang, K. Leitzell, E. Lonnoy, J. B. R. Matthews, T. K. Maycock, T. Waterfield, Ö. Yelekçi, R. Yu, & B. Zhou (Eds.), *Climate Change 2021: The Physical Science Basis. Contribution of Working Group I to the Sixth Assessment Report of the Intergovernmental Panel on Climate Change* (pp. 1055–1210). Cambridge University Press. https://doi.org/10.1017/9781009157896.001

Ejaz, T., Rahaman, W., C M, L., Mahalinganathan, K., & Thamban, M. (2021). Sea Ice Variability and Trends in the Western Indian Ocean Sector of Antarctica During the Past Two Centuries and Its Response to Climatic Modes. *Journal of Geophysical Research: Atmospheres*, *126*. https://doi.org/10.1029/2020JD033943

Enomoto, H., Motoyama, H., Shiraiwa, T., Saito, T., Kameda, T., Furukawa, T., Takahashi, S., Kodama, Y., & Watanabe, O. (1998). Winter warming over Dome Fuji, East

Antarctica and semiannual oscillation in the atmospheric circulation. *Journal of Geophysical Research: Atmospheres*, *103*(D18), 23103–23111. https://doi.org/10.1029/98JD02001

Ettema, J., van den Broeke, M. R., van Meijgaard, E., & van de Berg, W. J. (2010). Climate of the Greenland ice sheet using a high-resolution climate model – Part 2: Near-surface climate and energy balance. *The Cryosphere*, *4*(4), 529–544. https://doi.org/10.5194/tc-4-529-2010

Fettweis, X., Box, J. E., Agosta, C., Amory, C., Kittel, C., Lang, C., van As, D., Machguth, H., & Gallée, H. (2017). Reconstructions of the 1900–2015 Greenland ice sheet surface mass balance using the regional climate MAR model. *The Cryosphere*, *11*(2), 1015–1033. https://doi.org/10.5194/tc-11-1015-2017

Fisher, D. A., Koerner, R. M., Paterson, W. S. B., Dansgaard, W., Gundestrup, N., & Reeh, N. (1983). Effect of wind scouring on climatic records from ice-core oxygen-isotope profiles. *Nature*, *301*(5897), Article 5897. https://doi.org/10.1038/301205a0

Fisher, D. A., Reeh, N., & Clausen, H. B. (1985). Stratigraphic Noise in Time Series Derived from Ice Cores. *Annals of Glaciology*, *7*, 76–83. https://doi.org/10.3189/S0260305500005942

Fortuin, J. P. F., & Oerlemans, J. (1990). Parameterization of the Annual Surface Temperature and Mass Balance of Antarctica. *Annals of Glaciology*, *14*, 78–84. https://doi.org/10.3189/S0260305500008302

Fretwell, P., Pritchard, H. D., Vaughan, D. G., Bamber, J. L., Barrand, N. E., Bell, R., Bianchi, C., Bingham, R. G., Blankenship, D. D., Casassa, G., Catania, G., Callens, D., Conway, H., Cook, A. J., Corr, H. F. J., Damaske, D., Damm, V., Ferraccioli, F., Forsberg, R., … Zirizzotti, A. (2013). Bedmap2: Improved ice bed, surface and thickness datasets for Antarctica. *The Cryosphere*.

Gallée, H., & Schayes, G. (1994). Development of a Three-Dimensional Meso-γ Primitive Equation Model: Katabatic Winds Simulation in the Area of Terra Nova Bay, Antarctica. *Monthly Weather Review*, *122*(4), 671–685. https://doi.org/10.1175/1520-0493(1994)122<0671:DOATDM>2.0.CO;2

Gehring, J., Vignon, É., Billault-Roux, A.-C., Ferrone, A., Protat, A., Alexander, S. P., & Berne, A. (2022). Orographic Flow Influence on Precipitation During an Atmospheric River Event at Davis, Antarctica. *Journal of Geophysical Research: Atmospheres*, *127*(2), e2021JD035210. https://doi.org/10.1029/2021JD035210

Giovinetto, M. B., & Bull, C. (1987). *Summary and analyses of surface mass balance compilations for Antarctica, 1960-1985*. Byrd Polar Research Center, The Ohio State University. https://kb.osu.edu/bitstream/handle/1811/51730/1/BPRC_Rept_1.pdf

Godfred-Spenning, C. R., & Simmonds, I. (1996). An Analysis of Antarctic Sea-Ice and Extratropical Cyclone Associations. *International Journal of Climatology*, *16*(12), 1315–1332. https://doi.org/10.1002/(SICI)1097-0088(199612)16:12<1315::AID-JOC92>3.0.CO;2-M

Goel, V., Matsuoka, K., Berger, C. D., Lee, I., Dall, J., & Forsberg, R. (2020). Characteristics of ice rises and ice rumples in Dronning Maud Land and Enderby Land, Antarctica. *Journal of Glaciology*, *66*(260), 1064–1078. https://doi.org/10.1017/jog.2020.77

González-Herrero, S., Vasallo, F., Bech, J., Gorodetskaya, I., Elvira, B., & Justel, A. (2023). Extreme precipitation records in Antarctica. *International Journal of Climatology*, *n/a*(n/a). https://doi.org/10.1002/joc.8020

Gorodetskaya, I. V., Kneifel, S., Maahn, M., Van Tricht, K., Thiery, W., Schween, J. H., Mangold, A., Crewell, S., & Van Lipzig, N. P. M. (2015). Cloud and precipitation properties from ground-based remote-sensing instruments in East Antarctica. *The Cryosphere*, *9*(1), 285–304. https://doi.org/10.5194/tc-9-285-2015

Gorodetskaya, I. V., Silva, T., Schmithüsen, H., & Hirasawa, N. (2020). Atmospheric River Signatures in Radiosonde Profiles and Reanalyses at the Dronning Maud Land Coast, East Antarctica. *Advances in Atmospheric Sciences*, *37*(5), 455–476. https://doi.org/10.1007/s00376-020-9221-8

Gorodetskaya, I. V., Tsukernik, M., Claes, K., Ralph, M. F., Neff, W. D., & Lipzig, N. P. M. V. (2014). The role of atmospheric rivers in anomalous snow accumulation in East Antarctica. *Geophysical Research Letters*, *41*(17), 6199–6206. https://doi.org/10.1002/2014GL060881

Gorodetskaya, I. V., Van Lipzig, N. P. M., Van den Broeke, M. R., Mangold, A., Boot, W., & Reijmer, C. H. (2013). Meteorological regimes and accumulation patterns at Utsteinen, Dronning Maud Land, East Antarctica: Analysis of two contrasting years. *Journal of Geophysical Research: Atmospheres*, *118*(4), 1700–1715. https://doi.org/10.1002/jgrd.50177

Gossart, A., Helsen, S., Lenaerts, J. T. M., Broucke, S. V., Lipzig, N. P. M. van, & Souverijns, N. (2019). An Evaluation of Surface Climatology in State-of-the-Art

Reanalyses over the Antarctic Ice Sheet. *Journal of Climate*, *32*(20), 6899–6915. https://doi.org/10.1175/JCLI-D-19-0030.1

Grotjahn, R., Black, R., Leung, R., Wehner, M. F., Barlow, M., Bosilovich, M., Gershunov, A., Gutowski, W. J., Gyakum, J. R., Katz, R. W., Lee, Y.-Y., Lim, Y.-K., & Prabhat. (2016). North American extreme temperature events and related large scale meteorological patterns: A review of statistical methods, dynamics, modeling, and trends. *Climate Dynamics*, *46*(3–4), 1151–1184. https://doi.org/10.1007/s00382-015-2638-6

Guo, Z., Bromwich, D. H., & Cassano, J. J. (2003). Evaluation of Polar MM5 Simulations of Antarctic Atmospheric Circulation. *Monthly Weather Review*, *131*(2), 384–411. https://doi.org/10.1175/1520-0493(2003)131<0384:EOPMSO>2.0.CO;2

Hammer, C. U., Clausen, H. B., Dansgaard, W., Gundestrup, N., Johnsen, S. J., & Reeh, N. (1978). Dating of Greenland Ice Cores by Flow Models, Isotopes, Volcanic Debris, and Continental Dust. *Journal of Glaciology*, *20*(82), 3–26. https://doi.org/10.3189/S0022143000021183

Hersbach, H., Bell, B., Berrisford, P., Hirahara, S., Horányi, A., Muñoz-Sabater, J., Nicolas, J., Peubey, C., Radu, R., Schepers, D., Simmons, A., Soci, C., Abdalla, S., Abellan, X., Balsamo, G., Bechtold, P., Biavati, G., Bidlot, J., Bonavita, M., … Thépaut, J.-N. (2020). The ERA5 global reanalysis. *Quarterly Journal of the Royal Meteorological Society*, *146*(730), 1999–2049. https://doi.org/10.1002/qj.3803

Hewitson, B. C., & Crane, R. G. (2002). Self-organizing maps: Applications to synoptic climatology. *Climate Research*, *22*(1), 13–26. https://doi.org/10.3354/cr022013

Hirasawa, N., Nakamura, H., & Yamanouchi, T. (2000). Abrupt changes in meteorological conditions observed at an inland Antarctic Station in association with wintertime blocking. *Geophysical Research Letters*, *27*(13), 1911–1914. https://doi.org/10.1029/1999GL011039

Hofmann, D. J., Oltmans, S. J., Harris, J. M., Johnson, B. J., & Lathrop, J. A. (1997). Ten years of ozonesonde measurements at the south pole: Implications for recovery of springtime Antarctic ozone. *Journal of Geophysical Research: Atmospheres*, *102*(D7), 8931–8943. https://doi.org/10.1029/96JD03749

Holland, M. M., & Bitz, C. M. (2003). Polar amplification of climate change in coupled models. *Climate Dynamics*, *21*(3), 221–232. https://doi.org/10.1007/s00382-003-0332-6

Jackson, S. L., Vance, T. R., Crockart, C., Moy, A., Plummer, C., & Abram, N. J. (2022). Climatology of the Mount Brown South ice core site in East Antarctica: Implications for the interpretation of a water isotope record. *EGUsphere*, 1–36. https://doi.org/10.5194/egusphere-2022-1171

Jahn, A., Holland, M. M., & Kay, J. E. (2024). Projections of an ice-free Arctic Ocean. *Nature Reviews Earth & Environment*, *5*(3), 164–176. https://doi.org/10.1038/s43017-023-00515-9

Jones, A. E., & Shanklin, J. D. (1995). Continued decline of total ozone over Halley, Antarctica, since 1985. *Nature*, *376*(6539), 409–411. https://doi.org/10.1038/376409a0

Jones, J. M., Gille, S. T., Goosse, H., Abram, N. J., Canziani, P. O., Charman, D. J., Clem, K. R., Crosta, X., de Lavergne, C., Eisenman, I., England, M. H., Fogt, R. L., Frankcombe, L. M., Marshall, G. J., Masson-Delmotte, V., Morrison, A. K., Orsi, A. J., Raphael, M. N., Renwick, J. A., … Vance, T. R. (2016). Assessing recent trends in high-latitude Southern Hemisphere surface climate. *Nature Climate Change*, *6*(10), Article 10. https://doi.org/10.1038/nclimate3103

Jouzel, J., Alley, R. B., Cuffey, K. M., Dansgaard, W., Grootes, P., Hoffmann, G., Johnsen, S. J., Koster, R. D., Peel, D., Shuman, C. A., Stievenard, M., Stuiver, M., & White, J. (1997). Validity of the temperature reconstruction from water isotopes in ice cores. *Journal of Geophysical Research: Oceans*, *102*(C12), 26471–26487. https://doi.org/10.1029/97JC01283

Jouzel, J., & Merlivat, L. (1984). Deuterium and oxygen 18 in precipitation: Modeling of the isotopic effects during snow formation. *Journal of Geophysical Research: Atmospheres*, *89*(D7), 11749–11757. https://doi.org/10.1029/JD089iD07p11749

Kaczmarska, M., Isaksson, E., Karlöf, L., Brandt, O., Winther, J.-G., Wal, R. S. W. van de, Broeke, M. van den, & Johnsen, S. J. (2006). Ice core melt features in relation to Antarctic coastal climate. *Antarctic Science*, *18*(2), 271–278. https://doi.org/10.1017/S0954102006000319

Karlöf, L., Isaksson, E., Winther, J.-G., Gundestrup, N., Meijer, H. A. J., Mulvaney, R., Pourchet, M., Hofstede, C., Lappegard, G., Pettersson, R., Broeke, M. V. D., & Wal, R. S. W. V. D. (2005). Accumulation variability over a small area in east Dronning Maud Land, Antarctica, as determined from shallow firn cores and snow pits: Some implications for ice-core records. *Journal of Glaciology*, *51*(174), 343–352. https://doi.org/10.3189/172756505781829232

Kendall, M. G. (1975). *Rank correlation methods* (4th ed., 2d impression). Griffin.

King, J. C., Anderson, P. S., Vaughan, D. G., Mann, G. W., Mobbs, S. D., & Vosper, S. B. (2004). Wind-borne redistribution of snow across an Antarctic ice rise. *Journal of Geophysical Research: Atmospheres*, *109*(D11). https://doi.org/10.1029/2003JD004361

King, J. C., & Turner, J. (1997). *Antarctic climatology and meteorology*. Cambridge University Press.

Kittel, C., Amory, C., Agosta, C., Delhasse, A., Doutreloup, S., Huot, P.-V., Wyard, C., Fichefet, T., & Fettweis, X. (2018). Sensitivity of the current Antarctic surface mass balance to sea surface conditions using MAR. *The Cryosphere*, *12*(12), 3827–3839. https://doi.org/10.5194/tc-12-3827-2018

Kohonen, T. (2012). *Self-Organizing Maps*. Springer Science & Business Media.

Kohrs, R. A., Lazzara, M. A., Robaidek, J. O., Santek, D. A., & Knuth, S. L. (2014). Global satellite composites—20 years of evolution. *Atmospheric Research*, *135–136*, 8–34. https://doi.org/10.1016/j.atmosres.2013.07.023

Laepple, T., Münch, T., Casado, M., Hoerhold, M., Landais, A., & Kipfstuhl, S. (2018). On the similarity and apparent cycles of isotopic variations in East Antarctic snow pits. *The Cryosphere*, *12*(1), 169–187. https://doi.org/10.5194/tc-12-169-2018

Lazzara, M. A., Keller, L. M., Stearns, C. R., Thom, J. E., & Weidner, G. A. (2003). Antarctic Satellite Meteorology: Applications for Weather Forecasting. *Monthly Weather Review*, *131*(2), 371–383. https://doi.org/10.1175/1520-0493(2003)131<0371:ASMAFW>2.0.CO;2

Legg, S. (2021). IPCC, 2021: Climate Change 2021 - the Physical Science basis. *Interaction*. https://search.informit.org/doi/abs/10.3316/informit.315096509383738

Lenaerts, J. T. M., Medley, B., van den Broeke, M. R., & Wouters, B. (2019). Observing and Modeling Ice Sheet Surface Mass Balance. *Reviews of Geophysics*, *57*(2), 376–420. https://doi.org/10.1029/2018RG000622

Lenaerts, J. T. M., Meijgaard, E. van, Broeke, M. R. van den, Ligtenberg, S. R. M., Horwath, M., & Isaksson, E. (2013). Recent snowfall anomalies in Dronning Maud Land, East Antarctica, in a historical and future climate perspective. *Geophysical Research Letters*, *40*(11), 2684–2688. https://doi.org/10.1002/grl.50559

Lenaerts, J. T. M., Smeets, C. J. P. P., Nishimura, K., Eijkelboom, M., Boot, W., van den Broeke, M. R., & van de Berg, W. J. (2014). Drifting snow measurements on the

Greenland Ice Sheet and their application for model evaluation. *The Cryosphere*, *8*(2), 801–814. https://doi.org/10.5194/tc-8-801-2014

Li, L., & Pomeroy, J. W. (1997). Estimates of Threshold Wind Speeds for Snow Transport Using Meteorological Data. *Journal of Applied Meteorology and Climatology*, *36*(3), 205–213. https://doi.org/10.1175/1520-0450(1997)036<0205:EOTWSF>2.0.CO;2

Li, X., Cai, W., Meehl, G. A., Chen, D., Yuan, X., Raphael, M., Holland, D. M., Ding, Q., Fogt, R. L., Markle, B. R., Wang, G., Bromwich, D. H., Turner, J., Xie, S.-P., Steig, E. J., Gille, S. T., Xiao, C., Wu, B., Lazzara, M. A., … Song, C. (2021). Tropical teleconnection impacts on Antarctic climate changes. *Nature Reviews Earth & Environment*, *2*(10), 680–698. https://doi.org/10.1038/s43017-021-00204-5

Listowski, C., & Lachlan-Cope, T. (2017). The microphysics of clouds over the Antarctic Peninsula – Part 2: Modelling aspects within Polar WRF. *Atmospheric Chemistry and Physics*, *17*(17), 10195–10221. https://doi.org/10.5194/acp-17-10195-2017

Liu, Y., Li, F., Hao, W., Barriot, J.-P., & Wang, Y. (2019). Evaluation of Synoptic Snowfall on the Antarctic Ice Sheet Based on CloudSat, In-Situ Observations and Atmospheric Reanalysis Datasets. *Remote Sensing*, *11*(14), Article 14. https://doi.org/10.3390/rs11141686

Loon, H. van. (1967). The Half-Yearly Oscillations in Middle and High Southern Latitudes and the Coreless Winter. *Journal of the Atmospheric Sciences*, *24*(5), 472–486. https://doi.org/10.1175/1520-0469(1967)024<0472:THYOIM>2.0.CO;2

Mahalinganathan, K., Thamban, M., Ejaz, T., Srivastava, R., Redkar, B. L., & Laluraj, C. M. (2022). Spatial variability and post-depositional diffusion of stable isotopes in high accumulation regions of East Antarctica. *Frontiers in Earth Science*, *10*. https://doi.org/10.3389/feart.2022.925447

Mann, H. B. (1945). Nonparametric Tests Against Trend. *Econometrica*, *13*(3), 245–259. https://doi.org/10.2307/1907187

Markle, B. R., Bertler, N. a. N., Sinclair, K. E., & Sneed, S. B. (2012). Synoptic variability in the Ross Sea region, Antarctica, as seen from back-trajectory modeling and ice core analysis. *Journal of Geophysical Research: Atmospheres*, *117*(D2). https://doi.org/10.1029/2011JD016437

Marshall, G. J. (2003). Trends in the Southern Annular Mode from Observations and Reanalyses. *Journal of Climate*, *16*(24), 4134–4143. https://doi.org/10.1175/1520-0442(2003)016<4134:TITSAM>2.0.CO;2

Marshall, G. J., Thompson, D. W. J., & van den Broeke, M. R. (2017). The Signature of Southern Hemisphere Atmospheric Circulation Patterns in Antarctic Precipitation. *Geophysical Research Letters*, *44*(22), 11,580-11,589. https://doi.org/10.1002/2017GL075998

Massom, R. A., Pook, M. J., Comiso, J. C., Adams, N., Turner, J., Lachlan-Cope, T., & Gibson, T. T. (2004). Precipitation over the Interior East Antarctic Ice Sheet Related to Midlatitude Blocking-High Activity. *Journal of Climate*, *17*(10), 1914–1928. https://doi.org/10.1175/1520-0442(2004)017<1914:POTIEA>2.0.CO;2

Masson-Delmotte, V., Hou, S., Ekaykin, A., Jouzel, J., Aristarain, A., Bernardo, R. T., Bromwich, D., Cattani, O., Delmotte, M., Falourd, S., Frezzotti, M., Gallée, H., Genoni, L., Isaksson, E., Landais, A., Helsen, M. M., Hoffmann, G., Lopez, J., Morgan, V., … White, J. W. C. (2008). A Review of Antarctic Surface Snow Isotopic Composition: Observations, Atmospheric Circulation, and Isotopic Modeling. *Journal of Climate*, *21*(13), 3359–3387. https://doi.org/10.1175/2007JCLI2139.1

Matsuoka, K., Hindmarsh, R. C. A., Moholdt, G., Bentley, M. J., Pritchard, H. D., Brown, J., Conway, H., Drews, R., Durand, G., Goldberg, D., Hattermann, T., Kingslake, J., Lenaerts, J. T. M., Martín, C., Mulvaney, R., Nicholls, K. W., Pattyn, F., Ross, N., Scambos, T., & Whitehouse, P. L. (2015). Antarctic ice rises and rumples: Their properties and significance for ice-sheet dynamics and evolution. *Earth-Science Reviews*, *150*, 724–745. https://doi.org/10.1016/j.earscirev.2015.09.004

Mayewski, P. A., Meredith, M. P., Summerhayes, C. P., Turner, J., Worby, A., Barrett, P. J., Casassa, G., Bertler, N. a. N., Bracegirdle, T., Naveira Garabato, A. C., Bromwich, D., Campbell, H., Hamilton, G. S., Lyons, W. B., Maasch, K. A., Aoki, S., Xiao, C., & van Ommen, T. (2009). State of the Antarctic and Southern Ocean climate system. *Reviews of Geophysics*, *47*(1). https://doi.org/10.1029/2007RG000231

Medley, B., & Thomas, E. R. (2019). Increased snowfall over the Antarctic Ice Sheet mitigated twentieth-century sea-level rise. *Nature Climate Change*, *9*(1), Article 1. https://doi.org/10.1038/s41558-018-0356-x

Morcrette, J.-J. (2002). Assessment of the ECMWF Model Cloudiness and Surface Radiation Fields at the ARM SGP Site. *Monthly Weather Review*, *130*(2), 257–277. https://doi.org/10.1175/1520-0493(2002)130<0257:AOTEMC>2.0.CO;2

Morgan, V. I. (1985). An oxygen isotope—Climate record from the Law Dome, Antarctica. *Climatic Change*, *7*(4), 415–426. https://doi.org/10.1007/BF00139056

Mottram, R., Hansen, N., Kittel, C., van Wessem, J. M., Agosta, C., Amory, C., Boberg, F., van de Berg, W. J., Fettweis, X., Gossart, A., van Lipzig, N. P. M., van Meijgaard, E., Orr, A., Phillips, T., Webster, S., Simonsen, S. B., & Souverijns, N. (2021). What is the surface mass balance of Antarctica? An intercomparison of regional climate model estimates. *The Cryosphere*, *15*(8), 3751–3784. https://doi.org/10.5194/tc-15-3751-2021

Münch, T., Kipfstuhl, S., Freitag, J., Meyer, H., & Laepple, T. (2017). Constraints on post-depositional isotope modifications in East Antarctic firn from analysing temporal changes of isotope profiles. *The Cryosphere*, *11*(5), 2175–2188. https://doi.org/10.5194/tc-11-2175-2017

Münch, T., & Laepple, T. (2018). What climate signal is contained in decadal- to centennial-scale isotope variations from Antarctic ice cores? *Climate of the Past*, *14*(12), 2053–2070. https://doi.org/10.5194/cp-14-2053-2018

Nigro, M. A., Cassano, J. J., & Knuth, S. L. (2012). Evaluation of Antarctic Mesoscale Prediction System (AMPS) cyclone forecasts using infrared satellite imagery. *Antarctic Science*, *24*(2), 183–192. https://doi.org/10.1017/S0954102011000745

Noone, D., & Simmonds, I. (1998). Implications for the interpretation of ice-core isotope data from analysis of modelled Antarctic precipitation. *Annals of Glaciology*, *27*, 398–402. https://doi.org/10.3189/1998AoG27-1-398-402

Noone, D., & Simmonds, I. (2002). Annular variations in moisture transport mechanisms and the abundance of δ18O in Antarctic snow. *Journal of Geophysical Research: Atmospheres*, *107*(D24), ACL 3-1-ACL 3-11. https://doi.org/10.1029/2002JD002262

Noone, D., Turner, J., & Mulvaney, R. (1999). Atmospheric signals and characteristics of accumulation in Dronning Maud Land, Antarctica. *Journal of Geophysical Research: Atmospheres*, *104*(D16), 19191–19211. https://doi.org/10.1029/1999JD900376

Oerter, H., Drücker, C., Kipfstuhl, S., & Wilhelms, F. (n.d.). *Kohnen Station – the Drilling Camp for the EPICA Deep Ice Core in Dronning Maud Land*.

Parish, T. R., & Bromwich, D. H. (1987). The surface windfield over the Antarctic ice sheets. *Nature*, *328*(6125), 51–54. https://doi.org/10.1038/328051a0

Pattyn, F., & Morlighem, M. (2020). The uncertain future of the Antarctic Ice Sheet. *Science*, *367*(6484), 1331–1335. https://doi.org/10.1126/science.aaz5487

Perkins-Kirkpatrick, S. E., & Gibson, P. B. (2017). Changes in regional heatwave characteristics as a function of increasing global temperature. *Scientific Reports*, *7*(1), 12256. https://doi.org/10.1038/s41598-017-12520-2

Pezza, A., Sadler, K., Uotila, P., Vihma, T., Mesquita, M. D. S., & Reid, P. (2016). Southern Hemisphere strong polar mesoscale cyclones in high-resolution datasets. *Climate Dynamics*, *47*(5), 1647–1660. https://doi.org/10.1007/s00382-015-2925-2

Pfahl, S., & Wernli, H. (2012). Quantifying the Relevance of Cyclones for Precipitation Extremes. *Journal of Climate*, *25*(19), 6770–6780. https://doi.org/10.1175/JCLI-D-11-00705.1

Philippe, M., Tison, J.-L., Fjøsne, K., Hubbard, B., Kjær, H. A., Lenaerts, J. T. M., Drews, R., Sheldon, S. G., De Bondt, K., Claeys, P., & Pattyn, F. (2016). Ice core evidence for a 20th century increase in surface mass balance in coastal Dronning Maud Land, East Antarctica. *The Cryosphere*, *10*(5), 2501–2516. https://doi.org/10.5194/tc-10-2501-2016

Pohl, B., Favier, V., Wille, J., Udy, D. G., Vance, T. R., Pergaud, J., Dutrievoz, N., Blanchet, J., Kittel, C., Amory, C., Krinner, G., & Codron, F. (2021). Relationship Between Weather Regimes and Atmospheric Rivers in East Antarctica. *Journal of Geophysical Research: Atmospheres*, *126*(24), e2021JD035294. https://doi.org/10.1029/2021JD035294

Powers, J. G. (2007). Numerical Prediction of an Antarctic Severe Wind Event with the Weather Research and Forecasting (WRF) Model. *Monthly Weather Review*, *135*(9), 3134–3157. https://doi.org/10.1175/MWR3459.1

Pratap, B., Dey, R., Matsuoka, K., Moholdt, G., Lindbäck, K., Goel, V., Laluraj, C. M., & Thamban, M. (2022). Three-decade spatial patterns in surface mass balance of the Nivlisen Ice Shelf, central Dronning Maud Land, East Antarctica. *Journal of Glaciology*, *68*(267), 174–186. https://doi.org/10.1017/jog.2021.93

Ralph, F. M., Neiman, P. J., & Wick, G. A. (2004). Satellite and CALJET Aircraft Observations of Atmospheric Rivers over the Eastern North Pacific Ocean during the Winter of 1997/98. *Monthly Weather Review*, *132*(7), 1721–1745. https://doi.org/10.1175/1520-0493(2004)132<1721:SACAOO>2.0.CO;2

Reijmer, C. H., & Broeke, M. R. V. D. (2001). Moisture source of precipitation in Western Dronning Maud Land, Antarctica. *Antarctic Science*, *13*(2), 210–220. https://doi.org/10.1017/S0954102001000293

Reijmer, C. H., & Broeke, M. R. van den. (2003). Temporal and spatial variability of the surface mass balance in Dronning Maud Land, Antarctica, as derived from automatic weather stations. *Journal of Glaciology*, *49*(167), 512–520. https://doi.org/10.3189/172756503781830494

Reijmer, C. H., Broeke, M. R. van den, & Scheele, M. P. (2002). Air Parcel Trajectories and Snowfall Related to Five Deep Drilling Locations in Antarctica Based on the ERA-15 Dataset. *Journal of Climate*, *15*(14), 1957–1968. https://doi.org/10.1175/1520-0442(2002)015<1957:APTASR>2.0.CO;2

Reijmer, C. H., Van Meijgaard, E., & Van Den Broeke, M. R. (2004). Numerical Studies with a Regional Atmospheric Climate Model Based on Changes in the Roughness Length for Momentum and Heat Over Antarctica. *Boundary-Layer Meteorology*, *111*(2), 313–337. https://doi.org/10.1023/B:BOUN.0000016470.23403.ca

Rotschky, G., Holmlund, P., Isaksson, E., Mulvaney, R., Oerter, H., Broeke, M. R. V. D., & Winther, J.-G. (2007). A new surface accumulation map for western Dronning Maud Land, Antarctica, from interpolation of point measurements. *Journal of Glaciology*, *53*(182), 385–398. https://doi.org/10.3189/002214307783258459

Roussel, M.-L., Lemonnier, F., Genthon, C., & Krinner, G. (2020). Brief communication: Evaluating Antarctic precipitation in ERA5 and CMIP6 against CloudSat observations. *The Cryosphere*, *14*(8), 2715–2727. https://doi.org/10.5194/tc-14-2715-2020

Scarchilli, C., Frezzotti, M., Grigioni, P., De Silvestri, L., Agnoletto, L., & Dolci, S. (2010). Extraordinary blowing snow transport events in East Antarctica. *Climate Dynamics*, *34*(7), 1195–1206. https://doi.org/10.1007/s00382-009-0601-0

Schlosser, E. (1999). Effects of seasonal variability of accumulation on yearly mean δ18O values in Antarctic snow. *Journal of Glaciology*, *45*(151), 463–468. https://doi.org/10.3189/S0022143000001325

Schlosser, E., Duda, M. G., Powers, J. G., & Manning, K. W. (2008). Precipitation regime of Dronning Maud Land, Antarctica, derived from Antarctic Mesoscale Prediction System (AMPS) archive data. *Journal of Geophysical Research: Atmospheres*, *113*(D24). https://doi.org/10.1029/2008JD009968

Schlosser, E., Manning, K. W., Powers, J. G., Duda, M. G., Birnbaum, G., & Fujita, K. (2010). Characteristics of high-precipitation events in Dronning Maud Land, Antarctica. *Journal of Geophysical Research: Atmospheres*, *115*(D14). https://doi.org/10.1029/2009JD013410

Schlosser, E., & Oerter, H. (2002). Shallow firn cores from Neumayer, Ekströmisen, Antarctica: A comparison of accumulation rates and stable-isotope ratios. *Annals of Glaciology*, *35*, 91–96. https://doi.org/10.3189/172756402781816915

Schlosser, E., Powers, J. G., Duda, M. G., & Manning, K. W. (2011). Interaction between Antarctic sea ice and synoptic activity in the circumpolar trough: Implications for ice-core interpretation. *Annals of Glaciology*, *52*(57), 9–17. https://doi.org/10.3189/172756411795931859

Schlosser, E., Powers, J. G., Duda, M. G., Manning, K. W., Reijmer, C. H., & van den Broeke, M. R. (2010). An extreme precipitation event in Dronning Maud Land, Antarctica: A case study with the Antarctic Mesoscale Prediction System. *Polar Research*, *29*(3), 330–344. https://doi.org/10.3402/polar.v29i3.6072

Schlosser, E., Stenni, B., Valt, M., Cagnati, A., Powers, J. G., Manning, K. W., Raphael, M., & Duda, M. G. (2016). Precipitation and synoptic regime in two extreme years 2009 and 2010 at Dome C, Antarctica – implications for ice core interpretation. *Atmospheric Chemistry and Physics*, *16*(8), 4757–4770. https://doi.org/10.5194/acp-16-4757-2016

Seneviratne, S. I., Zhang, X., Adnan, M., Badi, W., Dereczynski, C., Di Luca, A., Ghosh, S., Iskandar, I., Kossin, J., Lewis, S., Otto, F., Pinto, I., Satoh, M., Vicente-Serrano, S. M., Wehner, M., & Zhou, B. (2021). Weather and climate extreme events in a changing climate. In V. Masson-Delmotte, P. Zhai, A. Pirani, S. L. Connors, C. Péan, S. Berger, N. Caud, Y. Chen, L. Goldfarb, M. I. Gomis, M. Huang, K. Leitzell, E. Lonnoy, J. B. R. Matthews, T. K. Maycock, T. Waterfield, Ö. Yelekçi, R. Yu, & B. Zhou (Eds.), *Climate Change 2021: The Physical Science Basis. Contribution of Working Group I to the Sixth Assessment Report of the Intergovernmental Panel on Climate Change* (pp. 1513–1766). Cambridge University Press. https://doi.org/10.1017/9781009157896.001

Servettaz, A. P. M., Orsi, A. J., Curran, M. A. J., Moy, A. D., Landais, A., Agosta, C., Winton, V. H. L., Touzeau, A., McConnell, J. R., Werner, M., & Baroni, M. (2020). Snowfall and Water Stable Isotope Variability in East Antarctica Controlled by Warm Synoptic Events. *Journal of Geophysical Research: Atmospheres*, *125*(17), e2020JD032863. https://doi.org/10.1029/2020JD032863

Shepherd, A., Ivins, E., Rignot, E., Smith, B., van den Broeke, M., Velicogna, I., Whitehouse, P., Briggs, K., Joughin, I., Krinner, G., Nowicki, S., Payne, T., Scambos, T., Schlegel, N., A, G., Agosta, C., Ahlstrøm, A., Babonis, G., Barletta, V., … The IMBIE team. (2018). Mass balance of the Antarctic Ice Sheet from 1992 to 2017. *Nature*, *558*(7709), 219–222. https://doi.org/10.1038/s41586-018-0179-y

Shepherd, A., Wingham, D., & Rignot, E. (2004). Warm ocean is eroding West Antarctic Ice Sheet. *Geophysical Research Letters*, *31*(23). https://doi.org/10.1029/2004GL021106

Simmonds, I., Keay, K., & Lim, E.-P. (2003). Synoptic Activity in the Seas around Antarctica. *Monthly Weather Review*, *131*(2), 272–288. https://doi.org/10.1175/1520-0493(2003)131<0272:SAITSA>2.0.CO;2

Sinclair, K. E., Bertler, N. a. N., & Trompetter, W. J. (2010). Synoptic controls on precipitation pathways and snow delivery to high-accumulation ice core sites in the Ross Sea region, Antarctica. *Journal of Geophysical Research: Atmospheres*, *115*(D22). https://doi.org/10.1029/2010JD014383

Sinclair, M. R. (1981). Record-High Temperatures in the Antarctic–A Synoptic Case Study. *Monthly Weather Review*, *109*(10), 2234–2242. https://doi.org/10.1175/1520-0493(1981)109<2234:RHTITA>2.0.CO;2

Sinclair, M. R. (1997). Objective Identification of Cyclones and Their Circulation Intensity, and Climatology. *Weather and Forecasting*, *12*(3), 595–612. https://doi.org/10.1175/1520-0434(1997)012<0595:OIOCAT>2.0.CO;2

Somos-Valenzuela, M., & Manquehual-Cheuque, F. (2020). Evaluating Multiple WRF Configurations and Forcing over the Northern Patagonian Icecap (NPI) and Baker River Basin. *Atmosphere*, *11*(8), Article 8. https://doi.org/10.3390/atmos11080815

Souverijns, N., Gossart, A., Gorodetskaya, I. V., Lhermitte, S., Mangold, A., Laffineur, Q., Delcloo, A., & van Lipzig, N. P. M. (2018). How does the ice sheet surface mass balance relate to snowfall? Insights from a ground-based precipitation radar in East Antarctica. *The Cryosphere*, *12*(6), 1987–2003. https://doi.org/10.5194/tc-12-1987-2018

Souverijns, N., Gossart, A., Lhermitte, S., Gorodetskaya, I. V., Kneifel, S., Maahn, M., Bliven, F. L., & van Lipzig, N. P. M. (2017). Estimating radar reflectivity—Snowfall rate relationships and their uncertainties over Antarctica by combining disdrometer and radar observations. *Atmospheric Research*, *196*, 211–223. https://doi.org/10.1016/j.atmosres.2017.06.001

Stenni, B., Scarchilli, C., Masson-Delmotte, V., Schlosser, E., Ciardini, V., Dreossi, G., Grigioni, P., Bonazza, M., Cagnati, A., Karlicek, D., Risi, C., Udisti, R., & Valt, M. (2016). Three-year monitoring of stable isotopes of precipitation at Concordia

Station, East Antarctica. *The Cryosphere*, *10*(5), 2415–2428. https://doi.org/10.5194/tc-10-2415-2016

Swetha Chittella, S. P., Deb, P., & Melchior van Wessem, J. (2022). Relative Contribution of Atmospheric Drivers to “Extreme” Snowfall Over the Amundsen Sea Embayment. *Geophysical Research Letters*, *49*(16), e2022GL098661. https://doi.org/10.1029/2022GL098661

Tang, M. S. Y., Chenoli, S. N., Samah, A. A., & Hai, O. S. (2018). An assessment of historical Antarctic precipitation and temperature trend using CMIP5 models and reanalysis datasets. *Polar Science*, *15*, 1–12. https://doi.org/10.1016/j.polar.2018.01.001

Tastula, E.-M., & Vihma, T. (2011). WRF Model Experiments on the Antarctic Atmosphere in Winter. *Monthly Weather Review*, *139*(4), 1279–1291. https://doi.org/10.1175/2010MWR3478.1

Terpstra, A., Gorodetskaya, I. V., & Sodemann, H. (2021). Linking Sub-Tropical Evaporation and Extreme Precipitation Over East Antarctica: An Atmospheric River Case Study. *Journal of Geophysical Research: Atmospheres*, *126*(9), e2020JD033617. https://doi.org/10.1029/2020JD033617

Tetzner, D., Thomas, E., & Allen, C. (2019). A Validation of ERA5 Reanalysis Data in the Southern Antarctic Peninsula—Ellsworth Land Region, and Its Implications for Ice Core Studies. *Geosciences*, *9*(7), Article 7. https://doi.org/10.3390/geosciences9070289

Thiery, W., Gorodetskaya, I. V., Bintanja, R., Van Lipzig, N. P. M., Van den Broeke, M. R., Reijmer, C. H., & Kuipers Munneke, P. (2012). Surface and snowdrift sublimation at Princess Elisabeth station, East Antarctica. *The Cryosphere*, *6*(4), 841–857. https://doi.org/10.5194/tc-6-841-2012

Thomas, E. R., van Wessem, J. M., Roberts, J., Isaksson, E., Schlosser, E., Fudge, T. J., Vallelonga, P., Medley, B., Lenaerts, J., Bertler, N., van den Broeke, M. R., Dixon, D. A., Frezzotti, M., Stenni, B., Curran, M., & Ekaykin, A. A. (2017). Regional Antarctic snow accumulation over the past 1000 years. *Climate of the Past*, *13*(11), 1491–1513. https://doi.org/10.5194/cp-13-1491-2017

Thompson, D. W. J., & Solomon, S. (2002). Interpretation of Recent Southern Hemisphere Climate Change. *Science*, *296*(5569), 895–899. https://doi.org/10.1126/science.1069270

Turner, J. (2004). The El Niño–southern oscillation and Antarctica. *International Journal of Climatology*, *24*(1), 1–31. https://doi.org/10.1002/joc.965

Turner, J. (2009). *Antarctic Climate Change and the Environment*. https://rosap.ntl.bts.gov/view/dot/18418

Turner, J., Colwell, S. R., & Harangozo, S. (1997). Variability of precipitation over the coastal western Antarctic Peninsula from synoptic observations. *Journal of Geophysical Research: Atmospheres*, *102*(D12), 13999–14007. https://doi.org/10.1029/96JD03359

Turner, J., Colwell, S. R., Marshall, G. J., Lachlan-Cope, T. A., Carleton, A. M., Jones, P. D., Lagun, V., Reid, P. A., & Iagovkina, S. (2004). The SCAR READER Project: Toward a High-Quality Database of Mean Antarctic Meteorological Observations. *Journal of Climate*, *17*(14), 2890–2898. https://doi.org/10.1175/1520-0442(2004)017<2890:TSRPTA>2.0.CO;2

Turner, J., Colwell, S. R., Marshall, G. J., Lachlan-Cope, T. A., Carleton, A. M., Jones, P. D., Lagun, V., Reid, P. A., & Iagovkina, S. (2005). Antarctic climate change during the last 50 years. *International Journal of Climatology*, *25*(3), 279–294. https://doi.org/10.1002/joc.1130

Turner, J., Lachlan-Cope, T. A., Thomas, J. P., & Colwell, S. R. (1995). The synoptic origins of precipitation over the Antarctic Peninsula. *Antarctic Science*, *7*(3), 327–337. https://doi.org/10.1017/S0954102095000447

Turner, J., Lu, H., King, J. C., Carpentier, S., Lazzara, M., Phillips, T., & Wille, J. (2022). An Extreme High Temperature Event in Coastal East Antarctica Associated With an Atmospheric River and Record Summer Downslope Winds. *Geophysical Research Letters*, *49*(4), e2021GL097108. https://doi.org/10.1029/2021GL097108

Turner, J., Phillips, T., Thamban, M., Rahaman, W., Marshall, G. J., Wille, J. D., Favier, V., Winton, V. H. L., Thomas, E., Wang, Z., Broeke, M. van den, Hosking, J. S., & Lachlan-Cope, T. (2019). The Dominant Role of Extreme Precipitation Events in Antarctic Snowfall Variability. *Geophysical Research Letters*, *46*(6), 3502–3511. https://doi.org/10.1029/2018GL081517

van Wessem, J. M., van de Berg, W. J., Noël, B. P. Y., van Meijgaard, E., Amory, C., Birnbaum, G., Jakobs, C. L., Krüger, K., Lenaerts, J. T. M., Lhermitte, S., Ligtenberg, S. R. M., Medley, B., Reijmer, C. H., van Tricht, K., Trusel, L. D., van Ulft, L. H., Wouters, B., Wuite, J., & van den Broeke, M. R. (2018). Modelling the climate and surface mass balance of polar ice sheets using RACMO2 – Part 2:

Antarctica (1979–2016). *The Cryosphere*, *12*(4), 1479–1498. https://doi.org/10.5194/tc-12-1479-2018

Vaughan, D. G., Comiso, J. C., Allison, I., Carrasco, J., Kaser, G., Kwok, R., Mote, P., Murray, T., Paul, F., & Ren, J. (2013). Observations: Cryosphere. *Climate Change*, *2103*, 317–382.

Vaughan, D. G., Marshall, G. J., Connolley, W. M., Parkinson, C., Mulvaney, R., Hodgson, D. A., King, J. C., Pudsey, C. J., & Turner, J. (2003). Recent Rapid Regional Climate Warming on the Antarctic Peninsula. *Climatic Change*, *60*(3), 243–274. https://doi.org/10.1023/A:1026021217991

Vignon, É., Roussel, M.-L., Gorodetskaya, I. V., Genthon, C., & Berne, A. (2021). Present and Future of Rainfall in Antarctica. *Geophysical Research Letters*, *48*(8), e2020GL092281. https://doi.org/10.1029/2020GL092281

Vimeux, F., Masson, V., Jouzel, J., Stievenard, M., & Petit, J. R. (1999). Glacial–interglacial changes in ocean surface conditions in the Southern Hemisphere. *Nature*, *398*(6726), Article 6726. https://doi.org/10.1038/18860

Wang, Q. (2021). Stronger Variability in the Arctic Ocean Induced by Sea Ice Decline in a Warming Climate: Freshwater Storage, Dynamic Sea Level and Surface Circulation. *Journal of Geophysical Research: Oceans*, *126*(3), e2020JC016886. https://doi.org/10.1029/2020JC016886

Wang, S., Ding, M., Liu, G., Li, G., & Chen, W. (2023). Blocking Events in East Antarctica: Impact on Precipitation and Their Association with Large-scale Atmospheric Circulation Modes. *Journal of Climate*, *1*(aop). https://doi.org/10.1175/JCLI-D-23-0419.1

Wauthy, S., Tison, J.-L., Inoue, M., El Amri, S., Sun, S., Fripiat, F., Claeys, P., & Pattyn, F. (2024). Spatial and temporal variability of environmental proxies from the top 120 m of two ice cores in Dronning Maud Land (East Antarctica). *Earth System Science Data*, *16*(1), 35–58. https://doi.org/10.5194/essd-16-35-2024

Welker, C., Martius, O., Froidevaux, P., Reijmer, C. H., & Fischer, H. (2014). A climatological analysis of high-precipitation events in Dronning Maud Land, Antarctica, and associated large-scale atmospheric conditions. *Journal of Geophysical Research: Atmospheres*, *119*(21), 11,932-11,954. https://doi.org/10.1002/2014JD022259

Werner, M., Mikolajewicz, U., Heimann, M., & Hoffmann, G. (2000). Borehole versus isotope temperatures on Greenland: Seasonality does matter. *Geophysical Research Letters*, *27*(5), 723–726. https://doi.org/10.1029/1999GL006075

Wille, J. D., Favier, V., Gorodetskaya, I. V., Agosta, C., Kittel, C., Beeman, J. C., Jourdain, N. C., Lenaerts, J. T. M., & Codron, F. (2021). Antarctic Atmospheric River Climatology and Precipitation Impacts. *Journal of Geophysical Research: Atmospheres*, *126*(8), e2020JD033788. https://doi.org/10.1029/2020JD033788

Yu, L., Yang, Q., Vihma, T., Jagovkina, S., Liu, J., Sun, Q., & Li, Y. (2018). Features of Extreme Precipitation at Progress Station, Antarctica. *Journal of Climate*, *31*(22), 9087–9105. https://doi.org/10.1175/JCLI-D-18-0128.1

Zhu, Y., & Newell, R. E. (1998). A Proposed Algorithm for Moisture Fluxes from Atmospheric Rivers. *Monthly Weather Review*, *126*(3), 725–735. https://doi.org/10.1175/1520-0493(1998)126<0725:APAFMF>2.0.CO;2

Zuhr, A. M., Münch, T., Steen-Larsen, H. C., Hörhold, M., & Laepple, T. (2021). Local-scale deposition of surface snow on the Greenland ice sheet. *The Cryosphere*, *15*(10), 4873–4900. https://doi.org/10.5194/tc-15-4873-2021

Annexure I

The Polar WRF model simulation

Model domains: To simulate the cyclone over coastal DML, we selected model domains covering the East Antarctic ice sheet and the Atlantic Ocean north of DML (Figure 2.3). The model was run with two-way nested domains with a horizontal grid spacing of 27, 9, and 3 km, with the output from the model domain with a 9-km resolution used for sensitivity analysis. The domain locations are depicted in Figure 2.3, and all domains were on a polar stereographic projection, which is appropriate for polar regions. For each domain, 61 vertical levels were chosen, and 100 hPa was taken as the model top level, identical to the AMPS setup. The outermost domain, containing 165 × 150 grid points and having a resolution of 27 km, covered the East Antarctic ice sheet and a wide ocean area of the South Atlantic and South Indian Ocean. Within the largest domain, a smaller area with a 9 km resolution and 361 × 295 grid points covered the coast of DML and included four coastal stations: Neumayer (Germany), Novolazarevskaya (Russia), Syowa (Japan), and Molodezhnaya (Russia). The innermost domain of 3 km resolution was selected to cover the landfall location of the cyclone and consisted of 727 × 658 grid points. It encompassed central DML and better resolved the ice sheet and ice shelves.

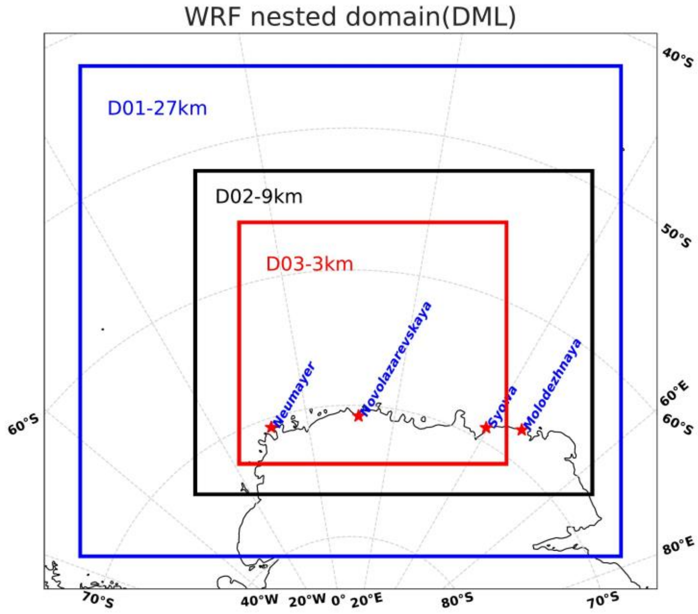

Figure 2.3: The Polar WRF nested domains used for the simulation of the cyclone

Model Boundary conditions: The model surface and lateral boundary conditions were provided by the European Centre for Medium-range Weather Forecasts (ECMWF) ERA-Interim reanalysis (Dee et al., 2011), which were available every 6 hours from January 1979 to August 2019. ECMWF's Integrated Forecast System (IFS) consists of the ERA-Interim atmospheric model and reanalysis system (operationally in September 2006). The fields have a spatial resolution of ~80 km (T255 in spectral resolution) on 60 vertical levels extending from the surface to 0.1 hPa. The system has a 12-hour analysis window, and a 4-dimensional variational analysis (4D-Var) was used to generate the analysis fields. The Polar WRF model dynamically downscales the forcing data to the chosen nested domains selected to follow a 3:1 ratio between model resolutions. Additionally, the orographic heights were obtained from the WRF standard orography using the Global Multi-resolution Terrain Elevation Data 2010 (GMTED2010) (Danielson & Gesch, 2011), while land use and land cover data was from the Moderate Resolution Imaging Spectroradiometer (MODIS) dataset at a resolution of 1 km. The basic physics options used for this study are listed below in Table 2.1.

Model configuration	Physics scheme/ details
Longwave radiation	Rapid Radiative Transfer Model for general circulation model (RRTMG)
Shortwave radiation	Goddard shortwave scheme
Cloud microphysics	WRF Single Moment 5-class (WSM5)
Land surface physics	Noah Land Surface model
Planetary Boundary layer physics	Mellor-Yamada-Janjic (MYJ) boundary layer scheme
Cumulus parameterization	Kain-Fritsch scheme

To assess the sensitivity of the Polar WRF model in simulating this cyclonic event with different physics options, additional schemes were tested in place of the standard longwave radiation, cloud microphysics, and PBL physics, as outlined in the following sections.

Observational data: A collection of surface observations in the area of cyclone landfall was obtained to evaluate the Polar WRF model's ability to dynamically downscale the cyclonic event. Four coastal stations in DML provided near-surface meteorological data (stations marked in Figure 2.3), which were obtained as part of the Scientific Committee on Antarctic Research (SCAR) Reference Antarctic Data for Environmental Research (READER) project and subjected to a strict quality control procedure (Turner et al., 2004). Observations at Syowa and Neumayer stations have 1-hour and 3-hour temporal resolution, respectively, whereas Novolazarevskaya and Molodezhnaya provide a 6-hour temporal resolution. Table 2.2 shows the latitude and longitude of the coastal stations used in this study, as well as a comparison of the actual surface elevation at each station to the Polar

WRF elevation from the nearest grid point. The 9 km model domain agrees well with actual station elevations despite DML's complex orography. Still, the height at the nearest grid position for Novolazarevskaya station is 46 m higher than the actual elevation. The difference in surface elevation between actual and model elevation at Syowa station is 20 m. In comparison, the remaining coastal stations in DML have a much smaller discrepancy of less than 10 m. Thus, the model simulated surface pressure, temperature, and wind speed were precisely adjusted for height variations using the hypsometric equation, lapse rate correction, and logarithmic wind profile, respectively. These height corrections are essential for accurately comparing the model results and the observed data (Deb et al., 2016).

Methodology: From 10 April to 19 April 1992, the Polar WRF model was run continuously for ten days, with all the experiments running starting at 00 UTC on 10 April and ending at 18 UTC on 19 April 1992. Polar region conditions such as sea-ice thickness, snow depth, sea-ice albedo values, and physics schemes for the basic run were used in the same way as the AMPS setup. Surface pressure, 10 m zonal and meridional wind components, and 2 m temperature from the 27, 9, and 3 km gridded domains of model runs at 3-hourly intervals were used to generate time series of variables at the model grid point

Surface elevation and location of the stations used in the model validation								
Station Name	Location	The nearest grid point on the Polar WRF model			Actual elevation (m)	Elevation in Polar WRF model (m)		
		Domain 1 (27 km)	Domain 2 (9 km)	Domain 3 (3 km)		D01	D02	D03
Syowa	69.00°S, 39.58°E	68.99°S, 39.32°E	69.02°S, 39.63°E	69.00°S, 39.59°E	21	3.766	30.136	11.264
Neumayer	70.64°S, 8.26°W	70.70°S, 8.05°W	70.67°S,8.28°W	70.65°S, 8.26°W	50	29.757	41.426	37.436
Novolazarevskaya	70.76°S, 11.81°E	70.87°S, 11.90°E	70.79°S, 11.89°E	70.76°S,11.811°E	119	558.537	165.86	71.054
Molodezhnaya	67.66°S, 45.83°E	67.73°S,45.91°E	67.66°S, 45.78°E	NA	40	250.169	43.401	NA

Table 2.2: Details of coastal DML stations and their locations. The locations of the nearest grid point to the station in each model domain are given. Also, a comparison with actual elevation and elevation in different model domains is listed.

closest to the location of the stations. Each time series was subsampled to coincide with the temporal resolution of each station's observations. The correlation coefficient, bias, and root-mean-square error (RMSE) between model output from the different domains and in-situ station observations were used to calculate a statistical measure of model performance. Accurately simulating atmospheric processes over the complex coastal regions that experience frequent cold katabatic winds necessitates precise representation of the boundary layer dynamics, cloud microphysics, and radiation parameterizations within the model. To examine the sensitivity of the Polar WRF model in recreating the cyclonic event, nine sensitivity experiments were carried out with several PBL, cloud-microphysics, and longwave radiation parameterizations. Along with the MYJ scheme in the AMPS configuration, sensitivity runs were conducted with different PBL schemes such as the one developed at Yonsei University Scheme (YSU), Mellor–Yamada Nakanishi Nino (MYNN) scheme, and Asymmetric Convection Model 2 (ACM2) scheme. Misrepresentation of cloud thermodynamics can produce considerable radiative biases at the surface due to cloud radiative effects, so a better representation of Antarctic clouds in numerical models is required (Listowski & Lachlan-Cope, 2017). So, to evaluate the model's sensitivity towards the selection of cloud microphysics, schemes such as the WRF double moment 6-class scheme (WDM-6), Morrison 2–2-moment Scheme, and Thompson Scheme were used with the AMPS default configuration. Longwave radiation sensitivity is also determined using the CAM scheme, RRTM longwave scheme, and New Goddard scheme.

Results of the model assessment

Validation using surface meteorological parameters

The following sections present a comparison of the model output with observational data from the coastal stations. Polar WRF model parameters such as 2-m temperature, wind speed, and direction, mean sea level pressure (MSLP), and surface pressure were compared with observational values of corresponding stations in all domains, as well as time-series values from the nearest grid point to observation location in ERA5 and ERA-Interim. The initial 24 hours of data were considered a spin-up period and were not included in the subsequent analysis (Bromwich et al., 2013). The variables pressure, temperature, and wind speed were corrected with the hypsometric equation, lapse rate correction, and logarithmic wind profile, respectively.

a) Neumayer and Syowa station

The temporal variations in surface variables during the cyclone are illustrated through time series analysis conducted for the Neumayer station, as depicted in Figure 2.4a. The surface meteorological variables are well-represented in all model domains; however, there were some discrepancies around the time of cyclone landfall. The model had difficulty in accurately reproducing the sudden fluctuations in 2-m temperature, wind speed, and wind direction. Specifically, the model significantly underestimates temperature readings just before the cyclone's landfall, resulting in an overall negative bias of 2°C.

This discrepancy arises from the model's inability to replicate sudden shifts in wind direction from southwest to northwest, leading to the advection of warm air masses from northern latitudes towards the station. While the model correctly captures changes in wind speed during the event, particularly the increase in wind speed, a notable overestimation is observed after the cyclone's landfall. Both the Polar WRF model and the reanalysis data correctly depicted changes in MSLP; however, there exists a slight tendency to overestimate (underestimate) values during (after) the storm's landfall. Reanalysis models, notably ERA5, exhibit good statistical performance in representing surface variables, particularly 2-m temperature, and wind direction and capturing subtle variations in these parameters at the Neumayer.

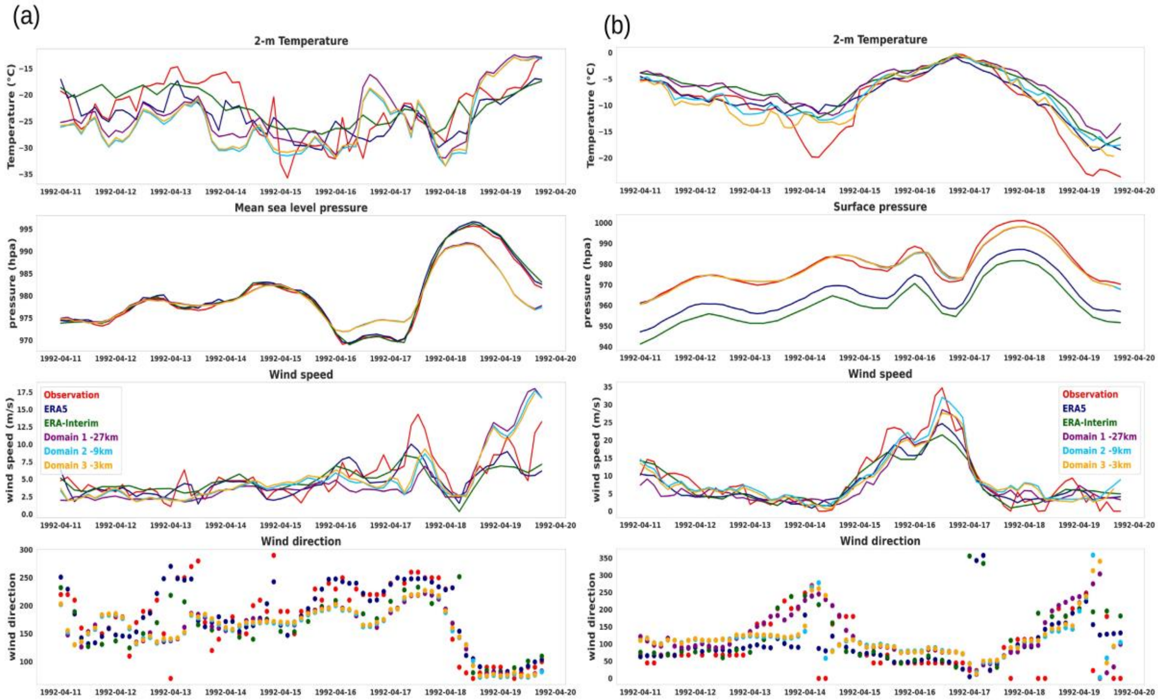

Figure 2.4: The Polar WRF model output validation for all the model domains. Time-series comparison of model output from the nearest grid point of observed values at Neumayer station and time-series values from ERA5 and ERA-Interim from the nearest grid point to observation location for the nine days from 11 April to 18 April 1992. (b) Same as (a) for Syowa station.

At Syowa (Figure 2.4b), the model effectively captures temperature variations; however, it fails to detect a notable temperature drop at the event's onset, possibly linked to a sudden shift in wind direction from S-SE to N-NE, resulting in cold air advection and subsequent cooling. The model's difficulty in capturing abrupt changes in wind direction also contributed to temperature overestimation towards the end of the cyclone's life cycle. The mean RMSE for all Polar WRF domains averages ~3°C, with a bias of +2°C, while ERA5 exhibits a slightly smaller positive bias of 1°C. Surface pressure temporal variability, particularly when the cyclone was over the coast, was accurately captured by the model with negligible negative bias. The reanalysis tended to underestimate surface pressure fluctuations, with notable bias and RMSE values (~10 hPa), possibly due to disparities in observation location and the nearest reanalysis model grid point. Furthermore, the model effectively represented temporal variations in 10-m wind speed and accurately represented the rapid wind speed increase that started on 14 April 1992, coinciding with the cyclone's arrival at the coast. Although the model generally had a good wind direction simulation, abrupt changes were occasionally missed, especially towards the cyclolysis.

b) Molodezhnaya and Novolazarevskaya stations

Analyzing the 6-hourly time series of observations from Molodezhnaya (Figure 2.5a) against corresponding Polar WRF output reveals the model's skill in capturing changes in 2-m temperature, surface pressure, wind speed, and wind direction during the cyclonic event.

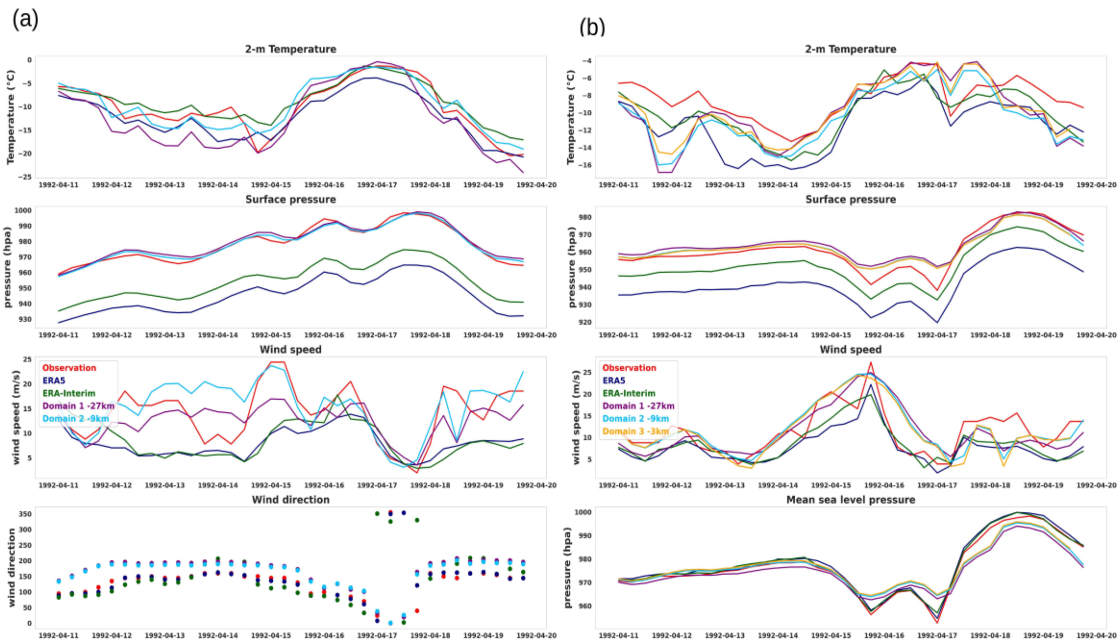

Figure 2.5: The validation of the Polar WRF output from all the domains. Time-series comparison of model output from the nearest grid point of observed values at Molodezhnaya, as well as time-

series values from such as ERA5 from the nearest grid point to observation location for the nine days from April 11 to April 18, 1992. (b) Same as (a) for Novolazarevskaya station.

Figure 2.5a shows the model's accurate depiction of surface pressure, wind speed and direction, and temperature, albeit with a slight underestimation of temperature before cyclone landfall over the location.

At Novolazarevskaya (Figure 2.5b), the increase in 2-m temperature during the cyclonic event was effectively captured. However, the model exhibited an overall temperature underestimation of ~2.0°C, notably having significant drops at the cyclone's onset and end, that were in the in-situ observations. Despite a high correlation coefficient of 0.9, ERA5 had a similar temperature underestimation when compared to the model output. Polar WRF effectively simulated changes in surface pressure, outperforming the reanalyses in statistics and capturing surface pressure drops during the lifetime of the storm, albeit with a small overestimation. Conversely, despite displaying a high correlation coefficient of 0.9, the reanalysis consistently underestimated the surface pressure, having large bias and RMSE values (~15 hPa for ERA5), possibly attributed to errors in orographic representation. Notably, Polar WRF accurately reproduced the increase in wind speed, particularly illustrating peak wind speed during the storm's landfall. In contrast, ERA5 had a negative bias of 3 m s^{-1}, underestimating the wind speed, notably during the storm's landfall.

Statistics of Sensitivity Studies

Along with the basic model simulation (with AMPS configuration), nine sensitivity runs were carried out by changing different model physics options and using different parameterization schemes, as explained in section 2.2.1.1. Correlation, RMSE, and bias values between observations and model output for 2-m temperature, surface pressure, and wind speed were calculated after each sensitivity run, during which each physics option was changed. Figure 2.6 shows the model statistics generated from the basic run and different sensitivity studies using PBL, cloud microphysics, and longwave radiation schemes, with these values being averaged for all stations. All these statistics are for the model output with a horizontal resolution of 9 km.

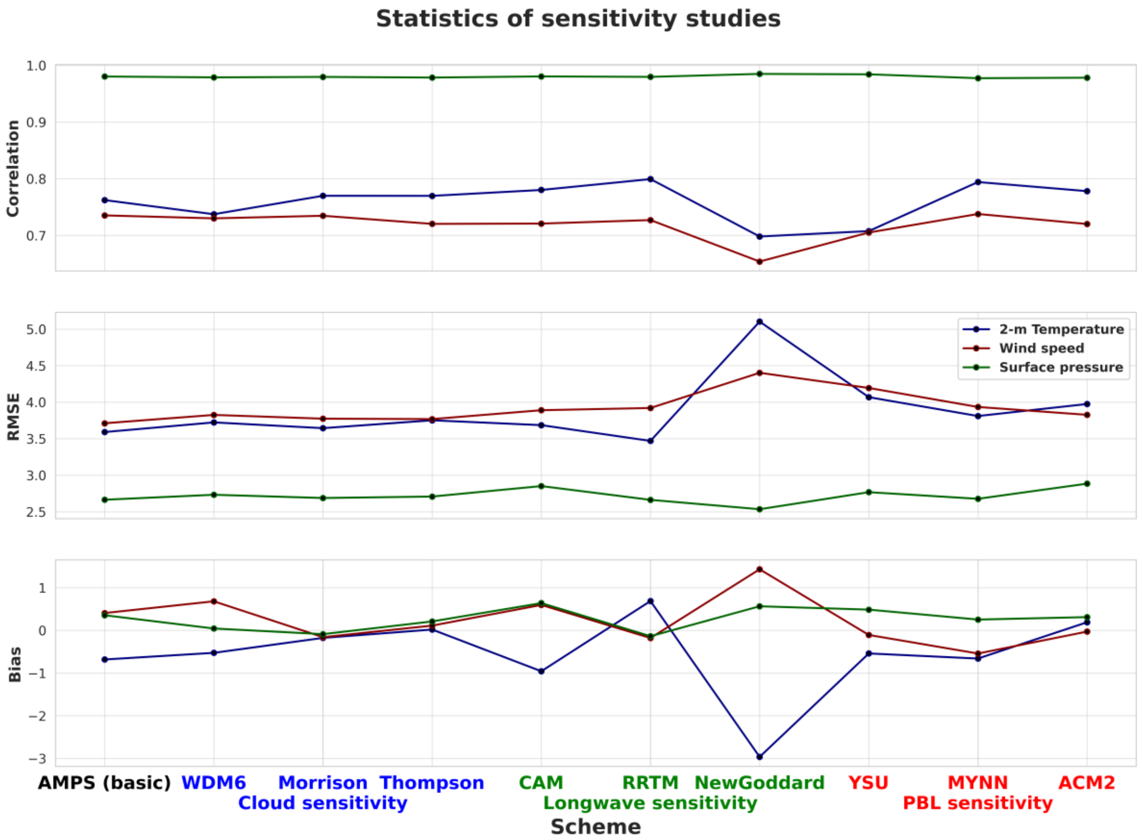

Figure 2.6: Statistical analysis values comparing observed variables and model output during different sensitivity simulations. All values are statistically significant at $p < 0.05$.

Surface pressure (MSLP for Neumayer) consistently correlated well with in-situ observations. It exhibited minimal fluctuations in response to changes in cloud microphysics, PBL, or longwave radiation schemes. However, the low correlation values observed with wind speed simulations gave significant concern, especially in regions with complex terrain, profoundly influenced by the orography. Moreover, the temperature bias resulting from the model's failure to capture warm or cold air advection during the event was improved by the choice of the appropriate parameterization schemes in the sensitivity studies. Notably, they revealed better statistics in longwave and PBL parameterization schemes, suggesting a higher susceptibility of these parameterizations to the synoptic event than cloud microphysics. This sensitivity analysis highlights the superior performance of the Morrison cloud microphysics scheme, the RRTM scheme for longwave radiation, and the MYNN scheme for PBL.

List of publications and conferences attended

Published articles

- **Simon, S**., Turner, J., Thamban, M., Wille, J. D., & Deb, P. (2024). Spatiotemporal variability of extreme precipitation events and associated atmospheric processes over Dronning Maud Land, East Antarctica. Journal of Geophysical Research: Atmospheres, 129, e2023JD038993. https://doi.org/10.1029/2023JD038993. (IF – 4.4)

- **Simon, S**., Turner, J., Meloth, T., Deb, P., Gorodetskaya, I. V., & Lazzara, M. (2024). An extreme precipitation event over Dronning Maud Land, East Antarctica—A case study of an atmospheric river event using the Polar WRF Model. Atmospheric Research, 311, 107724. https://doi.org/10.1016/j.atmosres.2024.107724 (IF - 5.5)

Papers Presented at Seminar/Conference

- **Simon, S**., Turner, J., Thamban, M., & Deb, P. (2022): "Extreme Precipitation Events and associated atmospheric patterns over Dronning Maud Land, East Antarctica", 10th Scientific Committee on Antarctic Research (SCAR) Open Science Conference, August 2022 (online) – (Oral Presentation)
- **Simon, S**., Deb, P., Turner, J., & Meloth, T. (2023): "Extreme precipitation event over Dronning Maud Land, East Antarctica – An Atmospheric River case study using the Polar WRF Model," 3rd International Workshop on Biodiversity and Climate Change (BDCC) (Kharagpur, February 2023) – (Oral Presentation)
- **Simon, S.**, Turner, J., Deb, P., Lazzara, M., Meloth, T. (2023): "An extreme precipitation event over Dronning Maud Land, East Antarctica - Atmospheric River case study using the Polar WRF Model," National Conference on Polar Sciences (NCPS), NCPOR, (Goa, May 2023) – (Poster Presentation)
- **Simon, S**., Turner, J., Deb, P., Lazzara, M., Meloth, T. (2023): "An extreme precipitation event over Dronning Maud Land, East Antarctica - Atmospheric River case study using the Polar WRF Model," XXVIII General Assembly of the International Union of Geodesy and Geophysics (IUGG) (Berlin, August 2023) – (Oral Presentation)
- **Simon, S**., Turner, J., Thamban, M., & Deb, P. (2023): "Spatial and Temporal Variability of Extreme Precipitation Events in Dronning Maud Land, East Antarctica:

Insights from High-Resolution Data and a Case Study," 8th National Conference of Ocean Society of India (OSICON-2023), (Hyderabad – September 2023) – (Oral Presentation)